NORTHWESTERN UNIVERSITY

Colloidal Superionics

A DISSERTATION

SUBMITTED TO THE GRADUATE SCHOOL
IN PARTIAL FULFILLMENT OF THE REQUIREMENTS

for the degree

DOCTOR OF PHILOSOPHY

Field of Chemistry

By

Yange Lin （林雁戈）

EVANSTON, ILLINOIS

July 2023

ABSTRACT

Colloidal Superionics

Yange Lin （林雁戈）

This dissertation focuses on the study of the superionic state in multicomponent systems, where the smaller component exhibits delocalization and mobility while still maintaining system compactness through component attractions. Superionic behavior is widely observed in various systems and plays a crucial role in ceramic superionic conductors, which offer high ion conductivities comparable to liquid electrolytes while ensuring enhanced safety. Consequently, comprehending the superionic state and effectively controlling the superionic transition hold both scientific and practical significance, particularly in the development of solid-state batteries. Recent advancements have revealed superionic behaviors in nanoparticle assemblies with asymmetric size, thereby expanding the scope of nanoparticle engineering and proposing colloidal assemblies as potential models for investigating the superionic state. This dissertation employs computer simulations to explore the superionic state in a binary colloidal crystal formed by highly asymmetric components in terms of size and charge. The research investigates the structural and dynamic properties of the crystal concerning temperature variations, changes in solution

concentration, and the application of an external electric field. These preliminary efforts deepen our understanding of superionics and establish a theoretical framework for the improved design of superionic conductors.

Acknowledgments

I would like to express my deepest gratitude to the individuals who have made significant contributions to the completion of this PhD dissertation. Their support, guidance, and encouragement have been invaluable throughout this journey.

First and foremost, I extend my heartfelt appreciation to my advisor, Prof. Monica Olvera de la Cruz, for accepting me as her student and providing me with the freedom to explore topics that piqued my interest. Her patience and unwavering support during the challenging times, especially amidst the Covid period, have been instrumental in my research progress. Collaborating with Monica has always been a pleasure, and I will fondly remember the countless discussions we had on physics. I will truly miss those days and nights of intellectual exchange. I would also like to express my sincere gratitude to my committee members, Prof. George Schatz, Prof. Franz Geiger, and Prof. Todd Gingrich, for their guidance and their commitment to reviewing my work. Their expertise and insightful feedback have been crucial in shaping the trajectory of my Ph.D. career.

I am grateful to be part of a vibrant and intellectually stimulating research group comprised of brilliant, creative, and supportive individuals. I extend my special thanks to Dr. Trung Nguyen, who taught me numerous simulation techniques during our subgroup meetings and provided invaluable coding assistance through our private discussions. Although he is no longer part of the group, the LAMMPS binaries he developed for me continue to be instrumental in my ongoing research. I am indebted to Prof. Felipe

Lastly, I would like to express my deepest appreciation to my friends and family, whose support and contributions to my life extend far beyond the scope of this PhD and the contents of this document.

List of abbreviations

BCC: body-centered cubic

CG: coarse-grained

ci: counterion

DH: Debye-Hückel

DLVO: Derjaguin-Landau-Verwey-Overbeek

DNA: deoxyribonucleic acid

DOF: degrees of freedom

EP: entropy production

FCC: face-centered cubic

FDT: fluctuation-dissipation theorem

FEP: free energy pertubation

IMT: insulator-metal transition

ISS: interstitial solid solution

LAMMPS: Large-scale Atomic/Molecular Massively Parallel Simulator

MD: molecular dynamics

MSD: mean square displacement

NESS: nonequilibrium steady state

NN: nearest-neighbor

NP: nanoparticles

NPT: constant (particle) number, constant pressure, and constant temperature

NPH: constant (particle) number, constant pressure, and constant enthalpy

NVT: constant (particle) number, constant volume, and constant temperature

PMMA: polymethylmethacrylate

PPPM: particle-particle particle-mesh

SEI: solid electrolyte interfaces

ss: steady state

sp: small particle neutral cluster

TUR: thermodynamic uncertainty relation

UCG: ultra-coarse-grained

VMD: Visual Molecular Dynamics

WCA: Weeks-Chandler-Andersen

WS: Wigner-Seitz

Glossary

σ: length unit

τ: time unit

ε: energy unit

t: time

T: temperature

V: volume

P or p: pressure

m: mass

q: charge

$\boldsymbol{a}$, $\boldsymbol{b}$, and $\boldsymbol{c}$: primitive vectors of the crystal

a, b, and c: lattice constants of the crystal

N_A: number of particles of type A

N_B: number of particles of type B

N_l: number of large particles

N_s: number of small particles

R: radius of the particle

D: diffusion coefficient

h: Planck constant

Λ: thermal de Broglie wavelength

k_B: Boltzmann constant

V_c: unit cell volume

T_c: critical temperature

n: stoichiometry (number ratio) of small particles and large particles

κ: screening constant in the Debey-Hückel potential

ϵ_0: vacuum permittivity, $8.854 \times 10^{-12}\,\mathrm{CV}^{-1}\mathrm{m}^{-1}$

ϵ_r: relative permittivity of the medium

F: free energy

F_{ext}: external force

f: free energy per unit cell

ρ: density, usually the density of small particles

ρ_0: mean density of small particles

$g(r)$: radial distribution function

G: Gibbs free energy

g: Gibbs free energy per unit cell

μ (Chap. 3): chemical potential

μ (Chap. 4): mobility

ϕ: volume fraction

$\Omega_{\alpha,\alpha'}$: the infinite set of coordinates of all α' positions when setting the α position as the origin

M_α ($\alpha = l$, $8c$ or $32f$): Madelung constant for type i sites

U: internal energy, or interaction energy

u_{ij}: the interaction energy between particle i and j

$\boldsymbol{E}$: electric field

E: magnitude of the electric field

β: the inverse of the thermal energy, $1/k_B T$

$\boldsymbol{q}$ (Chap. 3): wavevector

$\boldsymbol{q}$ (Appendix A): quaternion

γ (Chap. 3): Grüneisen constant

γ (Chap. 4): friction coefficient in Langevin dynamics

$A(n)$: prefactor of the internal pressure as a function of the stoichiometry n

$\boldsymbol{v}$: velocity of the particle

η_0: viscosity of the medium

η: energy conversion efficiency

$\boldsymbol{\xi}$: Gaussian white noise

$\boldsymbol{I}_d$: identity matrix in a d-dimensional space

δ_{ij}: Kronecker delta function

$P(x)$: probability distribution function

$\mathcal{Q}$: dissipation

$\mathcal{U}$: input energy

$\mathcal{W}$: work

$\mathcal{T}$: a time interval

Σ: entropy production

$\boldsymbol{j}$: particle current

S_{tran}: translational entropy, or two-body excess entropy

Υ: dynamical activity

χ: transport efficiency

$\boldsymbol{\Gamma}_{\mathcal{T}}$: evolution trajectory of the system in a time interval $\mathcal{T}$

$\mathcal{A}[\boldsymbol{\Gamma}_{\mathcal{T}}]$: Onsager-Machlup action functional along a trajectory $\boldsymbol{\Gamma}_{\mathcal{T}}$

$\hat{\boldsymbol{R}}_i$: orientation of a rigid body

$\boldsymbol{r} = (r, \psi_r, \theta_r)$: spatial vector in the real space

$\boldsymbol{\omega} = (\omega, \psi_\omega, \theta_\omega)$: frequency vector in the reciprocal space

$F(\boldsymbol{\omega})$: Fourier transform of $f(\boldsymbol{r})$

Y_l^k: spherical harmonics of degree l and order k

j_l: spherical Bessel function of the l-order

P_l^m: associated Legendre function of degree l and order m

(x): Gamma function

$J_\alpha(x)$: Bessel function of the first kind

$\hat{F}_n(\omega)$: spherical Hankel transform of order n of a function $f(\boldsymbol{r})$

$S_n\{...\}$: spherical Hankel transform of order n

f_l^k: spherical harmonic expansion coefficient of $f(\boldsymbol{r})$

F_l^k: spherical harmonic expansion coefficient of $F(\boldsymbol{\omega})$

$c^{l''}(l, k, l', k')$: Slater coefficients

$\hat{\mathcal{R}}(\alpha, \beta, \gamma)$: 3D rotation operator with Euler angles (α, β, γ)

$D_{mm'}^l(\alpha, \beta, \gamma)$: Wigner D-matrix

$d_{mm'}^l(\beta)$: Wigner's small d-matrix

Dedication

To the best memory and the best people.

To Wenbo Ji （籍文波）.

Table of Contents

List of Tables

List of Figures

CHAPTER 1

Introduction to superionic states

1.1. Liquid-state batteries

Batteries have become an integral part of our daily lives, powering our smartphones, computers, advanced energy storage technologies, and electric vehicles. Currently, Lithium-ion batteries are the most commonly used commercial batteries due to their high energy density [1]. The conducting media that facilitate the movement of ions between electrodes are typically organic liquid electrolytes or gel polymer electrolytes. Both of these media share similar conductive properties, with gel polymer electrolytes functioning by containing liquid electrolytes within polymer networks [2]. Liquid electrolytes offer several advantages, including high ion conductivity at room temperature and the ability to form solid electrolyte interfaces (SEI) on electrode surfaces. These interfaces enable the transport of Li^+ ions while blocking electrons to prevent further electrolyte decomposition, thereby maintaining electrochemical reactions and resulting in low interface resistivities [3, 4].

Liquid electrolytes, despite their benefits, have multiple drawbacks. One major concern is the potential for leakage, as these electrolytes are often composed of toxic and volatile organic solvents. Additionally, the use of high voltage is limited in liquid electrolytes due to the risk of oxidation-reduction reactions. Most liquid-state batteries have an electrochemical window that cannot exceed 4.5 V [5], which hinders improvements to

energy density. The operating temperature range of liquid-state batteries is also narrow, as low temperatures cause the electrolytes to become more viscous or even transition to solids, leading to a significant decrease in ion conductivities [1]. For gel electrolytes, the glass transition temperature of the polymers sets a lower temperature limit. At high temperatures, the vapor of organic solvents can harm battery seals. The thermal stability of lithium salts in the solvents is also a concern. For example, $LiPF_6$ [6], a commonly used salt, tends to decompose into LiF and PF_5 at high temperatures, which in turn can induce the decomposition of the solvent. These chemical reactions generate heat, which can accelerate further reactions and even cause flammable organic solvents to ignite, resulting in major incidents. Thus, there is a critical need to develop highly efficient and safer batteries.

1.2. Atomic Superionics and superionic state

Solid-state batteries are the most promising candidates for next-generation batteries. By replacing liquid electrolytes with solid ones, solid-state batteries can address the aforementioned issues and significantly enhance device safety. First and foremost, solid electrolytes, especially inorganic ones, are non-volatile and generally non-flammable. Therefore, the risk of ignition is substantially minimized. Secondly, solid-state batteries can operate in a wider range of temperatures, particularly high temperatures, due to the exceptional thermal stability of solids [7]. The stability of solids also permits the electrolytes to tolerate a broader range of operating voltage, which improves the energy density of the battery [8]. Thirdly, solid electrolytes are more chemically inert compared to their liquid counterparts, allowing them to be utilized in various environments. It also

implies that an inert protective atmosphere is not required during the synthesis of solid electrolytes [9], which can potentially lower the production cost of solid-state batteries.

However, the development of solid-state batteries is faced with significant challenges. One of the challenges is the lack of an SEI, as well as the material mismatch at the interface between the electrodes and solid electrolytes, which could hinder ion transport and lead to additional resistances [8]. On the other hand, the ion conductivities of traditional solid-state electrolytes are much lower than those of liquid electrolytes, mainly because ions are rigidly held in fixed positions by neighboring atoms or ions, which restricts their mobility.

A potential solution to this problem is the use of a specific class of solid-state materials with high ionic conductivities comparable to molten salts [10], known as *superionic conductors* or *superionics*. Superionic conductors typically consist of highly asymmetric components in size. Their high conductivities are associated with sublattice melting of the weakly bonded smaller component in ionic solids. Canonical examples of superionic materials include AgI and PbF_2 [11]. Below 420K, AgI exists in a stable wurtzite structure where larger ions, I^-, form a host lattice, and smaller ions, Ag^+, occupy fixed interstitial sites. Above 420K, the sublattice of Ag^+ melts, allowing them to diffuse rapidly within the lattice [12]. Additionally, superionic conductors for lithium and sodium ions are of great interest and significance. Due to their small sizes, Li^+ and Na^+ are readily detached from lattice sites and can diffuse through lattice gaps. Thus, lithium-ion and sodium-ion superionic conductors can exhibit liquid-like ionic conductivities at room temperature (such as $Li_{10}GeP_2S_{12}$ [13] discovered in 2011), and they have low activation energies for

use over a wide range of operating temperatures [14, 15, 16, 17, 18], making them the core component of solid-state batteries.

Solids composed of delocalized small components are referred to as having a superionic state. This state has been observed in ice by researchers, as evidenced by various studies [19, 20, 21, 22, 23]. At extremely high pressure ($\sim$300GPa) and temperatures ($\sim$1000K), covalent bonds between hydrogen and oxygen atoms break, causing hydrogen atoms to become dispersed throughout the entire structure instead of being centered between oxygen atoms. Similar transitions to superionic states have also been observed in ammonia [23]. Interestingly, superionic ice and ammonia have been detected in the rock layers of Uranus and Neptune, and are believed to be the source of these planets' magnetic fields [23]. Researchers are exploring the potential for superionic polymers, which are safer alternatives for use as electrolytes in solid-state batteries [24, 25]. By stiffening polymers, ion motion becomes decoupled from polymer relaxation and rearrangement, resulting in faster ion transport. It is worth noting that superionic states are not restricted to inorganic solid electrolytes, but can also exist more broadly. It is essential to comprehend this universal phenomenon.

1.3. Phase transitions to superionic states

When salts melt, their ionic conductivities generally experience a sharp increase, rising several orders of magnitude to values similar to those of liquids [10]. In contrast, the ionic conductivities of superionic solid electrolytes or materials show gradual increases or one or more sharp increases as they heat up while remaining solid. This indicates a series

of phase transitions, either continuous or discontinuous, from the ionic to the superionic state.

The gradual or sequential "sublattice melting" of particles on a specific set of lattice positions is believed to cause this series of phase transitions, where some particles become mobile and almost liquid-like, while the rest remain in their normal positions. Sublattice melting is thought to be responsible for the high ion conductivities observed in the superionic phase [10]. Researchers have investigated the prerequisites for sublattice melting and the superionic phase, with sufficient lattice defects and interstitial sites being identified as key factors [26, 27, 28]. Interstitial sites create space for the molten component and reduce the activation energy of the ion transport path from one lattice site to a neighboring vacant site [29, 14]. Therefore, improving the density of lattice defects while retaining enough charge carriers is crucial but challenging. Other factors, such as distortable frameworks of immobile ions and linear transport channels, may also contribute to reducing activation energy in transport although are not necessary [14].

To understand the conditions under which superionic materials melt gradually, in stages, or at a certain point, it is important to identify the different types of transitions to superionic phases. Researchers have classified three types of transitions [30]. Type I is a first-order transition where the ordered sublattice of mobile ions melts at a specific transition temperature, T_c, resulting in a sharp and discontinuous increase in ion conductivity. This transition is also known as an insulator-metal transition (IMT) [10]. In most Type I superionic conductors, the transition is accompanied by a rearrangement of the immobile ion lattice, typically from a low-symmetry structure to a high-symmetry structure [30]. This rearrangement is necessary to accommodate the disordering of mobile

ions and the resulting increase in symmetry in the sublattice. For example, in Ag_2S, the S^{2-} lattice changes from monoclinic to body-centered cubic (BCC) or face-centered cubic (FCC) at T_c, and the SO_4^{2-} lattice in Li_2SO_4 changes from monoclinic to FCC. There are a few exceptions to this, such as CuI, whose immobile ion lattice (I^-) remains FCC before and after the superionic transition. However, in general, lattice variations are common upon first-order sublattice melting and are worth considering.

Type II transitions are characterized by a continuous increase in ion conductivity as the material is heated, but exhibit peaks or anomalies in the specific heat [31]. The immobile ion lattice remains unchanged and is typically composed of FCC structures [30]. In an FCC lattice, the mobile ions tend to occupy the tetrahedral voids, which are energetically favorable due to the maximization of the electrostatic attraction. However, the tetrahedral voids in the FCC structure are separated by the octahedral voids, making it energetically unfavorable for mobile ions to diffuse through the lattice. As the temperature increases, the mobile ions gradually move to the octahedral voids, following the Boltzmann distribution, leading to a gradual increase in ion conductivity that does not rely on lattice variation. Type III transitions are similar to Type II, but lack any peak or anomaly in the specific heat [30]. They only occur in non-stoichiometric materials with complex crystal structures, where mixed phases could be the cause of the continuous nature of the transition.

The preceding discourse highlights the diverse factors that influence the transitions to superionic states. The nature of the ion-ion interactions, the lattice structure, and the stoichiometry all impact these transitions in unique ways. It is erroneous to view superionic materials as solely solids with numerous vacancies or liquids moving within a

rigid framework. The interactions between the mobile and stationary ions are crucial, disrupting the customary phonon spectrum of the solid and attenuating the robust ion-ion repulsion. There is still much to learn about these materials, and a comprehensive understanding remains elusive.

In summary, to further the development of batteries and energy storage technologies, it is essential to comprehend charge transport in superionic materials for the design and synthesis of new superionic conductors. Additionally, controlling transitions to superionic states is important due to the wide range of superionic behaviors and states. Achieving a comprehensive understanding of superionic materials and their physical nature necessitates good models for both experimental and theoretical studies, where colloidal assemblies could be a perfect fit.

This dissertation will focus on studies of superionic behaviors in charged colloidal crystals and is divided into three chapters (Chap. 2, 3, and 4). In Chap. 2, we explore the discovery of superionic states in an isolated binary colloidal crystal with highly asymmetric components in size and charge. In Chap. 3, we examine the ionic to superionic transition in a binary charged colloidal crystal in equilibrium with a solution of colloidal particles. In Chap. 4, we investigate the structural transitions and charge transport in a binary charged colloidal crystal under an external electric field. A brief summary of each chapter's content and organization is presented below.

- **Chapter 2:** We explore the discovery of superionic states in an isolated binary colloidal crystal composed of highly asymmetric components in size and charge. We observe sublattice melting in colloidal crystals of oppositely charged particles

immersed in salt solutions. As the temperature increases, the small particles, akin to mobile ions in superionic compounds, undergo melting and form a superionic phase. Unlike superionic phases in atomic systems, these delocalized small particles in a crystal of large oppositely charged particles result in crystals with non-electroneutral stoichiometric ratios. This leads to structures exhibiting multiple domains of ionic crystals in percolated superionic phases with adjustable stoichiometries.

- **Chapter 3:** We simulate a charged colloidal crystal in equilibrium with a solution containing small colloidal particles and counterions using Coulomb interaction between the finite-size components. We find ionic to metallic first order transitions by increasing either the temperature or the concentration of small particles in the solution. The transition is accompanied by a lattice expansion and increased absorption of small particles into the crystal. We compute the free energies of the ionic and metallic states using the Madelung constant and Wigner-Seitz cell approaches, respectively, combined with the quasi-harmonic lattice model. The calculation reproduces the simulated transition and reveals that the enthalpic gain is more pronounced than the entropic gain in the transition from ionic to metallic bonding when materials are exchanged with the solution.

- **Chapter 4:** We use coarse-grained molecular simulations with underdamped Langevin dynamics to explore how a binary charged colloidal crystal reacts to an external electric field. As the field strength increases, we find transitions from insulator (ionic state), to superionic (conductive state), to laning, to complete

melting (liquid state). In the superionic state, the resistivity decreases with increasing temperature, which is contrary to metals, yet the increment decreases as the electric field becomes stronger. Additionally, we verify that the dissipation of the system and the fluctuation of charge currents obey recently developed thermodynamic uncertainty relation. Our results describe charge transport mechanisms in colloidal superionic conductors.

CHAPTER 2

Sublattice Melting in Charged Colloidal Crystals[*]

2.1. Introduction

Colloidal particles, which range in size from several nanometers to a few microns, are small solid particles that can be suspended in fluids via thermal motion and buoyancy. Common materials for colloidal suspensions include low-solubility compounds like $Al(OH)_3$ and $Fe(OH)_3$, which can form small clusters within the nanometer scale when they precipitate from water at an uncontrolled rate. However, polymers are more favorable materials for producing colloidal particles. One of the most well-studied systems is that of polymethylmethacrylate (PMMA) nanoparticles, which can be synthesized with high precision. Colloidal particles made of PMMA can have a size polydispersity of less than 3% [33], making them ideal for a wide range of applications, from paints and inks to critical diagnostic tests [33]. Furthermore, colloidal particles and their assemblies can serve as perfect models to study various structures and behaviors, especially those in atomic and molecular systems that are difficult to characterize and track [34, 35, 36, 37, 38, 39]. By scaling up the particles from the atomic scale to the nanoscale while maintaining their size ratio, it is possible to reproduce the same or similar structures and behaviors in colloidal systems, and even synthesize novel structures without atomic counterparts.

---

[*]This chapter is primarily based on the published work [32] of Yange Lin and Monica Olvera de la Cruz, **Sublattice melting in binary superionic colloidal crystals**, *Phys. Rev. E* 101.3 (2020): 032603, with modified notations and extended details to comply with the structure of this work.

Techniques such as laser-scanning confocal fluorescence microscopy [33] enable visualization of each particle and tracking of its motion in both space and time, leading to a deeper understanding at the particle level.

In addition to the precise control of particle size, colloidal systems exhibit diverse interparticle interactions that are easier to tune than those in atomic or molecular systems. This makes colloids an interesting model system for fundamental condensed matter physics. In addition to hard-core and van der Waals interactions, electrostatics is one of the most common interactions in colloids. Due to their large specific surface area, colloidal particles tend to adsorb co-ions and become charged. For instance, metal oxides and metal hydroxides such as $Al(OH)_3$ and $Fe(OH)_3$ adsorb cations, while metal sulfides such as Ag_2S adsorb anions. By coating PMMA with poly-12-hydroxystearic acid, the amount and sign of charge on each nanoparticle can be precisely tuned by adding tetrabutylammonium bromide salt [40, 41]. Like-charge repulsions stabilize the colloidal suspension and prevent particle aggregation. Dissociation of surface groups of nanoparticles, such as amino acids, also charges the particles [42]. As the dissociation is often pH-dependent, it provides another means to control particle charge by adjusting the pH of the solution.

Under appropriate conditions, two types of nanoparticles with opposite charges can form complex superstructures through colloidal assembly [41, 42, 43, 44]. The formation of these structures can be driven by various interactions, including depletion forces resulting from pure hard-core repulsions of NPs and smaller particles in the solution such as ions [45, 46, 47, 48]. Interestingly, even in the absence of smaller particles, hard-core NPs can still crystallize via entropy-driven processes [49, 50, 51]. Magnetic colloidal particles can assemble through dipole-dipole interactions that can be manipulated by external magnetic

fields, leading to fascinating time-varying phenomena [52, 53, 54, 55]. Additionally, by grafting DNA sequences onto the surface of different NPs, particles with complementary sequences can co-assemble while repelling those with unmatched sequences, allowing for the synthesis of various NP superlattices and hierarchical structures [56, 57, 58, 59, 60].

Unlike chemical compounds in atomic systems, colloidal assemblies do not face constraints from the number, symmetry, or energy of orbitals. This property greatly expands the possible crystal structures that can contain multiple types of NPs, particularly binary colloidal crystals. Over the past few decades, several types of binary colloidal crystals with different component ratios have been studied, such as AB [61], AB_2 [53], and AB_8 [41]. Experimental and computational studies have shown that the size and charge ratios of the two components, as well as the ionic strength of the solution, are critical factors in the assembly process of binary superlattices [41, 45, 43].

The majority of research on binary charged colloidal crystals has focused on classical atomic ionic compounds with fixed particle positions. However, in 2019, Girard *et al.* discovered colloidal crystals that resemble atomic metallic crystals. These crystals were formed through the co-assembly of highly size-asymmetric DNA-functionalized nanoparticles (NPs) with complementary end nucleotide sequences [62]. By decreasing the number of grafted DNA chains on the smaller NPs and/or increasing the temperature, the strength of interactions between the two components is reduced. This causes the smaller NPs to undergo a transition from localized at the interstitial sites to delocalized and roaming the crystal while still preserving the integrity of the lattice formed by the larger NPs, similar to the behavior of electrons in metals. Molecular dynamics (MD) simulations have

demonstrated this bonding behavior in co-assemblies of asymmetric NPs, even in the absence of electrostatic interactions [62, 63, 64]. The transition from localized to delocalized small components, known as *metallization*, has been predicted to exist in cubic [63] and various non-cubic functionalized colloidal crystal lattices [64]. Some of these lattices have been successfully obtained experimentally [65]. Additionally, metallization behavior has been observed in two-dimensional lattices [66].

In the following sections of this chapter, we investigate whether metallization behavior exists in charged colloidal systems by incorporating electrostatic interactions. This is a critical step in exploring the potential to assemble real superionic conductors using oppositely charged colloids in salt solutions. In charged colloidal crystals, the charge neutrality restriction present in traditional ionic and superionic atomic crystals can be removed when small ions screen the charge [41, 42]. Additionally, the range of the interaction potential can be adjusted by controlling the salt concentration in regimes where the Debye-Hückel approximation is valid [42, 43]. As such, these colloidal systems have the potential to expand the scope of colloidal science and superionic materials.

We hypothesize that the significant size difference between the colloidal components is crucial for observing sublattice melting in colloidal systems. This is in line with the prerequisites for atomic superionics discussed in Chapter 1. Therefore, we focus on binary oppositely charged colloidal crystals with a substantial difference in size and charge. We study the thermal expansion of the superlattice with different stoichiometries and find a sharp transition from ionic to superionic phases under specific stoichiometries. This transition is characterized by a discontinuous jump in lattice spacing as temperature increases and by the double-well shape of the free energy landscape observed through

MD simulations. We also observe regions of coexistence between different phases, such as ionic-like phases of varying stoichiometries at low temperatures or ionic-like phases coexisting with superionic-like phases at intermediate temperatures. We analyze these regions of coexistence by calculating the time-averaged density of small particles [67] and explain why the attractions provided by the small particles in superionic-like phases are not depletion-type interactions. Finally, we discuss the potential realization of our observations in experiments and their potential applications.

2.2. Methods

2.2.1. Coarse-Grained Molecular Simulation Model

In our model of size-asymmetric binary colloidal crystals, we adopt a coarse-grained approach, where both large (A) and small (B) NPs are treated as isotropic, monodispersed, charged spheres. The interaction between particles of the same species is purely repulsive, preventing the spontaneous formation of crystal structures from pure As or Bs. The implicit presence of ions in the system is accounted for by applying the Debye-Huckel approximation, which describes pair potentials between charged nanoparticles at salt concentrations up to approximately $300\,\mathrm{mM}$ of NaCl [47]. In our model, particles interact through the Weeks-Chandler-Andersen (WCA) potential, which accounts for excluded volume effects, and the Debye-Hückel (DH) potential, which takes into account the screened Coulombic interactions:

$$U(r) = U_{WCA}(r) + U_{DH}(r),$$
(2.1)

where

$$(2.2) \qquad U_{WCA}(r_{ij}) = \begin{cases} 4\varepsilon \left[\left(\dfrac{\sigma_{ij}}{r_{ij}} \right)^{12} - \left(\dfrac{\sigma_{ij}}{r_{ij}} \right)^{6} \right] + \varepsilon, & r_{ij} < r_{cut}, \\[3mm] 0, & r_{ij} > r_{cut}, \end{cases}$$

$$(2.3) \qquad U_{DH}(r_{ij}) = \frac{q_i^* q_j^* e^{-\kappa r_{ij}}}{r_{ij}/\sigma} \varepsilon.$$

The energy term of the WCA potential, ε, is chosen to be the characteristic energy parameter in our simulations. The cutoff distance of the WCA potential $r_{cutWCA}^{ij} = 2^{1/6} \sigma_{ij}$, where σ_{ij} is pair-dependent and is calculated from the Lorentz-Berthelot mixing rules $\sigma_{ij} = R_i + R_j$. Here the radii of the two species were fixed at $R_A = 5\sigma$ and $R_B = 1\sigma$, where σ is the characteristic distance parameter. For the Debey-Hückel potential, κ is the screening strength, and q_i^* and q_j^* are effective reduced charges. For colloidal particles, an extended form of q_i^* commonly used in simulations includes the hard-core via the Derjaguin-Landau-Verwey-Overbeek (DLVO) potential which gives $q_i^* = q_i e^{\kappa R_i}/(1 + \kappa R_i)$ [41, 44], yet it is accurate only for dilute systems. In concentrated colloidal suspensions, such as in the crystals studied here, q^* has a more complicated form [68]. Thus, without losing generality we directly use q^* as simulation parameters that are independent of κ and the compactness of the system. We keep the exponentially-decaying part with the distance between particles because it is preserved in nonlinear models even when water effects and ions are explicitly included [47]. The cutoff distance of the Debey-Huckel potential $r_{cutDH}^{ij} = 3\kappa^{-1} + \sigma_{ij}$.

From the energy unit ε and distance unit σ, the reduced quantities can be defined, including the reduced temperature $T^* = k_B T/\varepsilon$, the reduced pressure $P^* = P\sigma^3/\varepsilon$, the reduced time $\tau^* = t\sqrt{\varepsilon/(m\sigma^2)}$, and the reduced charges $q^* = q/\sqrt{4\pi\epsilon_0\epsilon_r\sigma\varepsilon}$. Here, e is the elementary charge; ϵ_0 and ϵ_r are the vacuum permittivity and the relative permittivity of the medium, respectively. In the rest of the paper the prefix *reduced* will be omitted and these quantities are in terms of the reduced quantities.

2.2.2. zero pressure NPT simulations

All the MD simulations are done in the LAMMPS software package [69]. We initialize the system by setting large particles in perfect FCC crystal positions in a periodic cubic box, with small particles randomly placed throughout the lattice while avoiding strong overlap. The number of crystal unit cells in each direction is 6 (We have examined larger systems and found that the system size effect is negligible. See Table 2.1 and Figure 2.8 in the Appendix section of this chapter for more details). The system is first thermalized in the canonical (NVT) ensemble with a Langevin thermostat, then is slowly compressed to a close-packing state by reducing the simulation box size. After the system is equilibrated for $2 \times 10^3\tau^*$ (10^6 timesteps), it is switched to the isobaric–isothermal (NPT) ensemble with a large enough external pressure to keep the system compressed and run for another $2 \times 10^3\tau^*$. The pressure is subsequently relaxed to exactly 0 and the system is further equilibrated for $2\times10^4\tau^*$ (10^7 timesteps). To simplify the simulations, the cubic symmetry of the simulation box is maintained during the run.

Simulating a crystal under zero pressure is crucial to ensure that the assembly forms purely due to the attraction between the large and small particles, and not because of any

external compression. However, zero-pressure NPT simulations must be conducted with caution [70]. In principle, any solid will eventually vaporize under zero pressure, leading to the absence of stable crystals in equilibrium. This means that the crystal structures obtained in simulations are metastable and may collapse in the long run. Nevertheless, in terms of free energy, the equilibrium volume (or lattice spacing) of the crystal satisfies the equation:

$$(2.4) \qquad\qquad 0 = \left.\left(\frac{\partial F}{\partial V}\right)\right|_T = -p.$$

This indicates that the metastable structures, in fact, give the accurate equilibrium volume (or lattice spacing), as confirmed by the comparison of NPT simulation results and NVT simulation results in the latter section. Therefore, zero-pressure NPT simulations provide a fast method of acquiring the equilibrium structures, but should not be run for an extended period.

In this work, we focus on the FCC structure, which is one of the closest packed structures commonly observed in charged colloidal assemblies [41, 42, 43, 44]. These structures maximize the long-range electrostatic interactions. Removing the symmetry constraint in simulations may allow the crystal to transform from the FCC to other non-cubic or cubic structures, such as the BCC structure, more easily. A following study on metallization in size-asymmetric DNA-functionalized colloidal crystals observed deformation of the lattice of large particles (the immobile component) due to short-range interactions [64].

In terms of conductive behaviors, the BCC structure is better than the FCC structure. The BCC structure contains tetrahedra that share faces with one another, and the largest voids are tetrahedra. Thus, small particles can move among equivalent sites by passing

through the tetrahedral faces. In contrast, the FCC structure contains tetrahedra that share corners with one another and share faces with octahedra, not with other tetrahedra. Similarly, the octahedra share faces only with tetrahedra. If small particles pass through the faces of the polyhedra, the conduction path consists of alternating tetrahedral and octahedral sites. This difference in lattice often results in FCC structures having higher activation energies and smaller diffusion coefficients than BCC structures [30]. Nevertheless, this work focuses on the variation of the small particle positions and does not consider the lattice deformation of the large particles during transitions, which is an interesting topic but is outside the scope of this study.

2.3. Results and Discussions

2.3.1. First-Order Sublattice Melting

We first investigate the relationship between the strength of the attraction between the two components (A-B attraction) and the crystal structure of colloidal particles. Specifically, reducing the A-B attraction leads to an increase in potential energy wells and a decrease in the activation energy of transport, which can cause the delocalization of the smaller component. Previous research [62] supports this idea.

Our results show that under moderate salt conditions, reducing the A-B attraction can cause colloidal crystals to transition from ionic phases to superionic phases (Figure 2.1). To illustrate this, we examine the equilibrium size of the simulation box, which is equivalent to six lattice constants. We vary the reduced charge of the small particles, denoted as q_B^*, while keeping the temperature at $T^* = 0.3$, and the stoichiometric ratio of small (B) and large (A) particles, denoted as $N_B : N_A$, at 8. Additionally, we set the

charge of the large particles to $q_A^* = -247$, and the screening strength to $\kappa\sigma = 0.7$. [†] We find that when $q_B^* = +11$, the small particles aggregate into an ionic crystal, where they are fixed at interstitial positions and form a regular sublattice. As we decrease q_B^*, the A-B attraction weakens, and the equilibrium box size gradually increases. When $q_B^* = +5.5$ and $+4$, the attraction strength is no longer sufficient to localize the small particles at specific positions, but it can still keep the crystal stable. Therefore, the sublattice melts, and the system transitions to a superionic-like structure. Further decreasing q_B^* induces the melting of the whole FCC crystal.

[†]We note that when setting $\sigma = 1\,\mathrm{nm}$, the screening strength we use corresponds to a salt concentration of approximately $44\,\mathrm{mM}$ NaCl. This concentration falls within the concentration range where the Debye-Huckel approximation is applicable. Moreover, the sizes of the large and small nanoparticles are 10nm and 2nm, respectively, which are reasonable values in experiments.
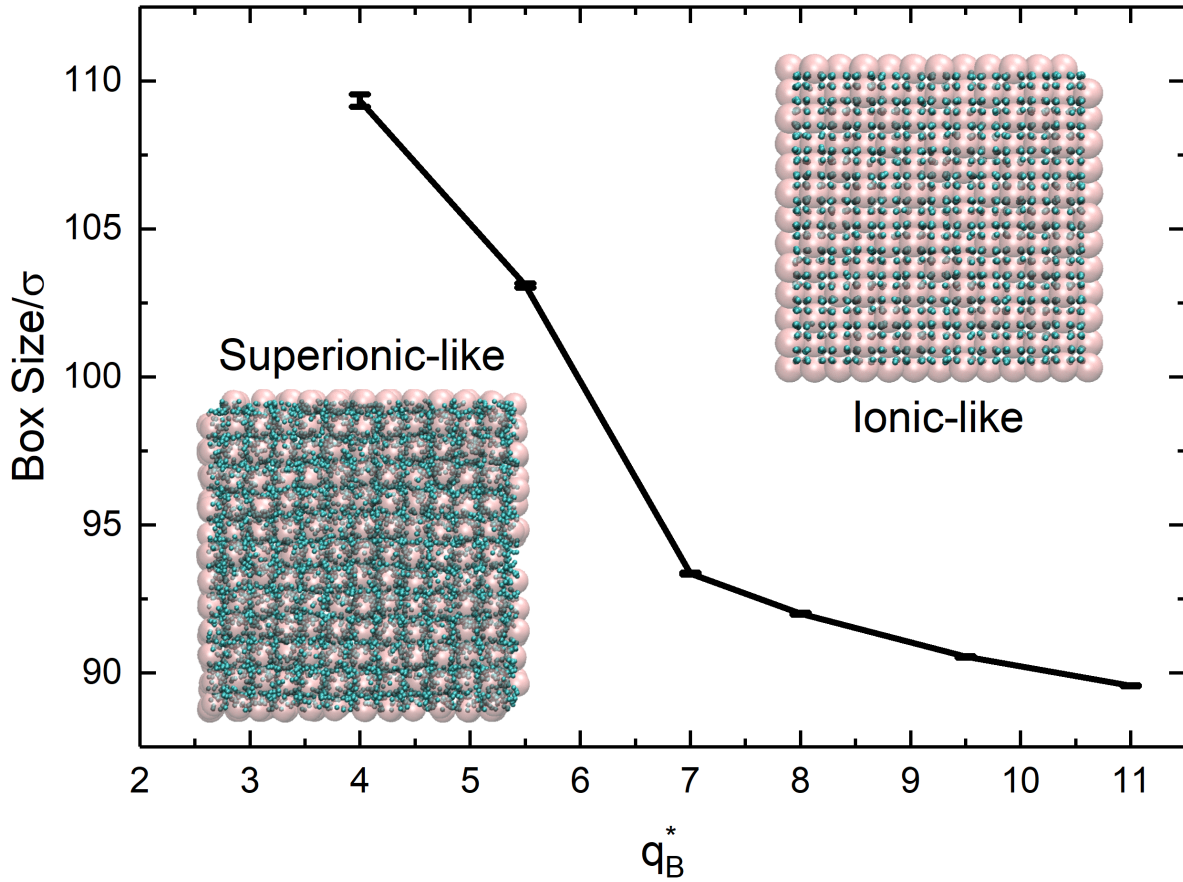
Figure 2.1. Simulation box size under different reduced charges of the small particles (q_B^*) at $T^* = 0.3$, for $N_B/N_A = 8$, $q_A^* = -247$ at $\kappa\sigma = 0.7$. Two distinct phases are observed, superionic-like and ionic-like; the snapshots are from the [001] direction of the FCC crystal.

Maintaining a medium salt concentration is critical for the stability of colloidal crystals, particularly when the colloidal particles themselves are not charge-neutral. A high salt concentration (large κ) weakens the A-B attraction by screening the charges, which causes the crystal to melt due to insufficient cohesive energy. Conversely, reducing the salt concentration increases the A-B attraction, which enhances the repulsion between large particles, resulting in a gas state where large particles stay far apart, surrounded

by small particles. As the salt concentration approaches 0, charge neutrality becomes increasingly important and eventually becomes a requirement for stability, as discussed in Chap. 3. The melting behavior of an unstable crystal at low pressure is shown in Figure 2.9 in the Appendix section of this chapter.

Increasing the temperature (T^*) above 0.3 in the system with $q_A^* = -247$, $q_B^* = +11$, and $\kappa\sigma = 0.7$ causes the sublattice to melt. We also observe a strong first-order ionic-to-superionic transition at $N_B/N_A = 8$. If we convert q_i^* to bare charges q_i using the DLVO approximation for these parameters, we get $q_A \approx -34$ and $q_B \approx +9$, indicating that the crystal is not charge-neutral. In contrast, the nearly charge-neutral crystal with $q_A^* = -247$, $q_B^* = +11$ ($q_A \approx -34$ and $q_B \approx +4$) also exhibits sublattice melting, as shown in Figure 2.1. This comparison demonstrates that sublattice melting can occur without charge neutrality if sufficient screening exists. We determine the sublattice melting temperature by analyzing changes in the equilibrated simulation box size. Heating curves of the box size for different number ratios N_B/N_A (Figure 2.2) show that the lattice expands as the temperature increases, but for $N_B/N_A = 8$, the expansion is discontinuous at a specific temperature ($T^* = 0.68$), indicating a first-order phase transition for sublattice melting. At $N_B/N_A = 10$, a similar but weaker discontinuous lattice expansion occurred. For $N_B/N_A = 9$, the lattice has two distinct discontinuous expansions (at $T^* = 0.3$ and $T^* = 0.46$), which we later find are caused by the melting of two separate sublattices with different favorable stoichiometric ratios ($N_B/N_A = 8$ and $N_B/N_A = 10$).
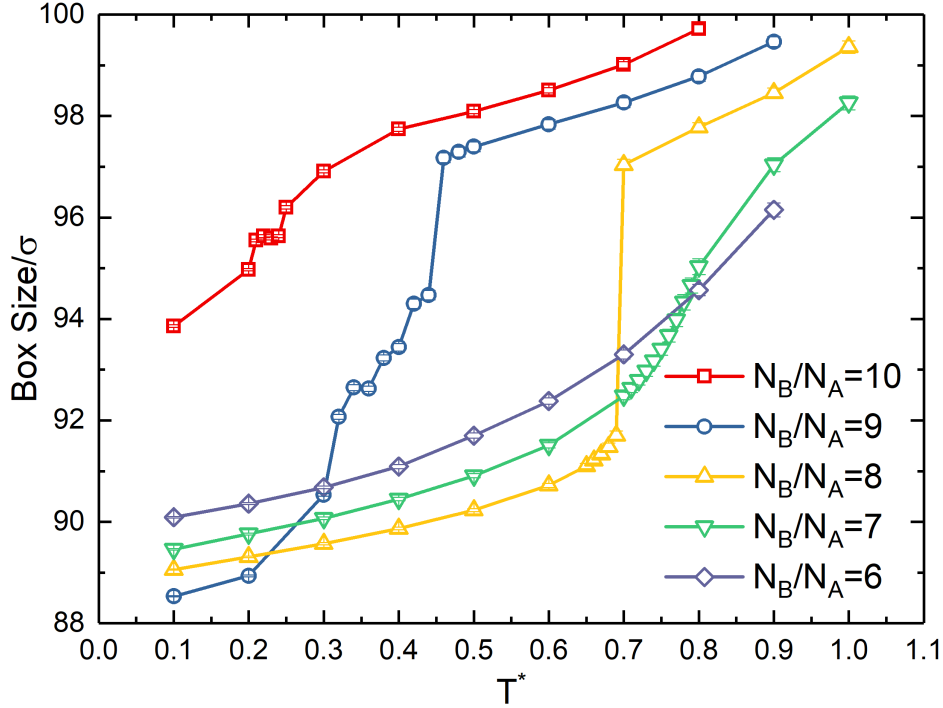
Figure 2.2. Heating curves of the equilibrium box size under different number ratios N_B/N_A with $q_A^* = -247$, $q_B^* = +11$, $\kappa\sigma = 0.7$. First-order sublattice melting is observed at $N_B/N_A = 8$, 9, and 10.

The phenomenon of the first-order phase transition occurring only at $N_B/N_A = 8$ and $N_B/N_A = 10$ in a size-asymmetric binary crystal can be explained by using Wyckoff positions, a fundamental concept in crystallography [71]. Wyckoff positions are used to describe the positions of special sites and their symmetries inside a unit cell. In this case, we use them to describe the location of small particles in the crystal. In an FCC unit cell, there are two important Wyckoff positions: the $32f$ and the $8c$ positions. The $32f$ positions are the four inner face centers of the tetrahedral voids in the unit cell, while the

$8c$ positions are the centers of these tetrahedrons. Since one FCC unit cell also contains four large particles, the number ratio between the $32f$ positions and the large particles is $8 : 1$, and between the $8c$ positions and the large particles is $2 : 1$. In a size-asymmetric oppositely-charged binary crystal, the small particles on the $32f$ positions have lower energy than on the $8c$ positions. This is because each particle on the $32f$ positions is closer to oppositely-charged large particles than the $8c$ positions, maximizing the screened electrostatic interactions that are not long-range. Therefore, in the ionic phases, the small particles tend to first occupy the $32f$ positions and then the $8c$ positions, resulting in two favorable number ratios $N_B/N_A = 8$ and $N_B/N_A = 10$. In fact, the $32f$ positions are commonly the home for the small particles in a AB_8 binary ionic crystal [41, 42, 43, 44]. At low temperatures, the crystal is in the ionic state that is enthalpically favorable but entropically unfavorable. In this state, the small particles are basically stuck at their equilibrium positions, resulting in a great entropy loss compared to the superionic state in which the small particles can access the whole free space inside the crystal. As a result, there exists a transition temperature above which the system favors entropy over enthalpy and expands the lattice spacing for small particles previously trapped in the interstitial positions to delocalize. Figure 2.10 in the Appendix section of this chapter shows how the diffusion coefficient of small particles varies with the temperature.
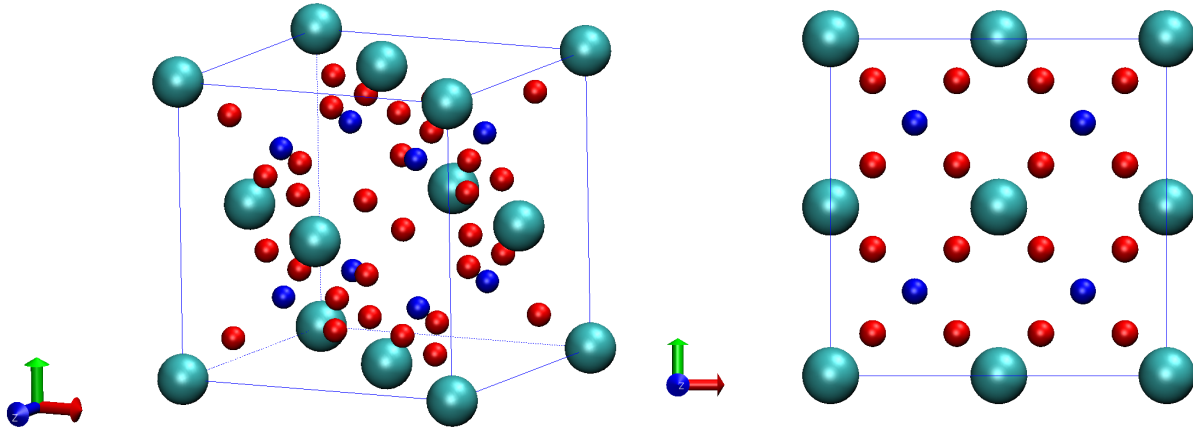
Figure 2.3. Schematic plots of the $32f$ and $8c$ Wyckoff positions in the FCC crystal. (Left) One FCC unit cell contains four atoms (cyan), eight $8c$ positions (blue), and thirty two $32f$ positions (red). (Right) The view from the [001] direction.

Based on volume expansion, the ionic-to-superionic transition appears to be continuous at number ratios $N_B/N_A < 8$. One possible explanation for this is that thermal expansion, rather than other factors, governs volume expansion in these systems due to the presence of vacancy defects (unoccupied $32f$ positions) and lower cohesive energy. When in their ionic state, these superstructures resemble the interstitial solid solution (ISS) phase observed in size asymmetric hard-sphere mixtures under high external pressure [72]. In the ISS phase, the crystal lattice is formed by large spheres, while the small spheres occupy interstitial sites and diffuse among them via vacancies like a fluid, with the number of small spheres less than the number of interstitial sites.

To evaluate the nature of the transition, it is necessary to analyze an order parameter, typically the density fluctuation around the mean density $\delta\rho$ and the correlation length. When transitioning from isotropic (or delocalized in space) to periodic (localized on lattice

sites) structures by decreasing the temperature, the symmetry of this order parameter changes, and the transition cannot be continuous [73]. In Figure 2.4, we show the radial distribution function of small particles $g_{BB}(r)$ in the crystal with $N_B/N_A = 7$ at different temperatures and observe a change in symmetry. This change is reflected in the differences in long-range ordering and peak positions between the superionic ($T^* = 0.8$) and ionic phases ($T^* = 0.4$). Therefore, it is possible that sublattice melting at ratios $N_B/N_A < 8$ is weakly first order.
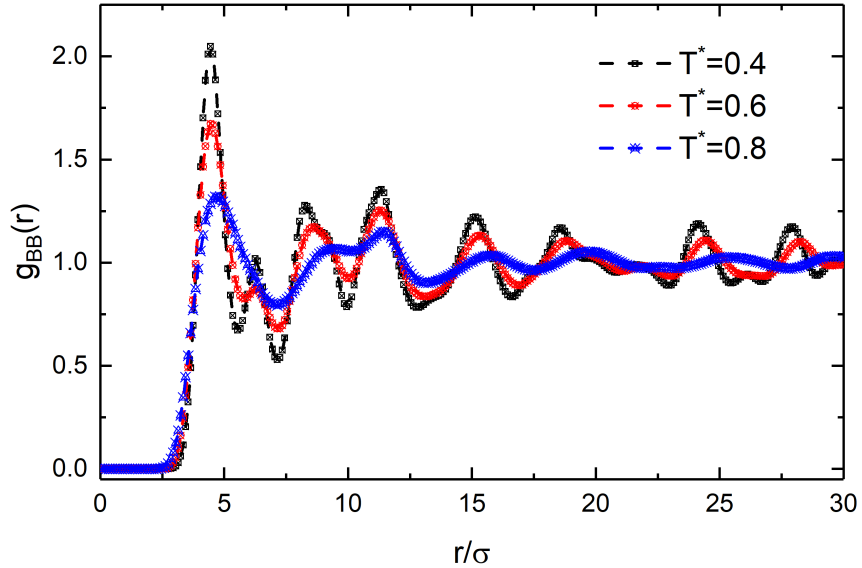
Figure 2.4. The radial distribution function of small particles $g_{BB}(r)$ at $N_B/N_A = 7$ for $T^* = 0.4$, 0.6, and 0.8.

2.3.2. Free Energy Calculations

Relative Helmholtz free energy landscapes are calculated by thermodynamic integration methods [70]. In thermodynamics, the Helmholtz free energy, F, is related to the pressure by $-P = (\partial F/\partial V)_{N,T}$. Therefore, under constant particle numbers and constant temperature, the relative free energy can be calculated from the integral:

$$
F_{rel}(V) = F(V) - F(V_0) = -\int_{V_0}^{V} P dV
$$

(2.5)

$$
\approx -\sum_i (P_{i+1} + P_i)(V_{i+1} - V_i)/2,
$$

where $F(V_0)$ is the reference state, and midpoint approximation was used to numerically evaluate the integral.
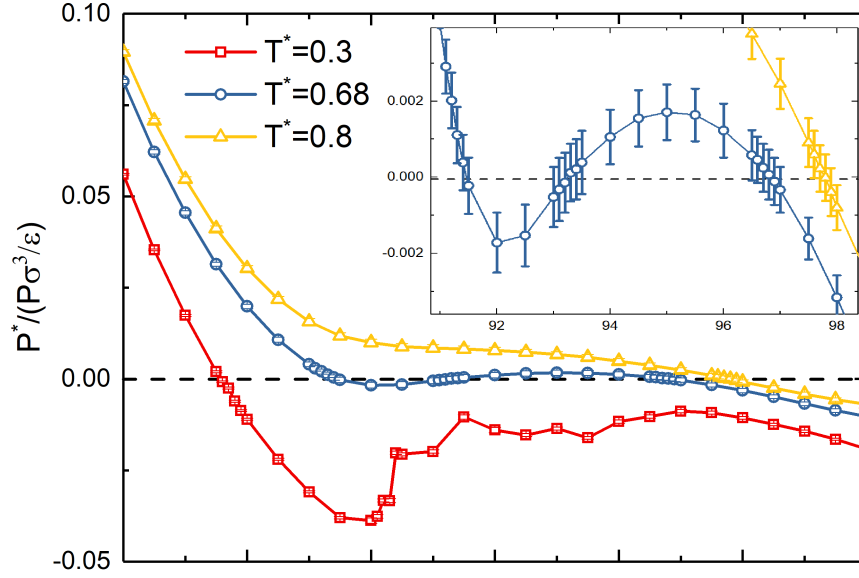
Figure 2.5. The Pressure–Volume plot obtained in NVT simulations. The enlarged view of the zero points of the pressure is shown in the Inset.

To evaluate Eqn. (2.5), a series of NVT simulations with a Langevin thermostat are performed for different volumes V_i at a fixed ratio of $N_B/N_A = 8$. The system is first initialized in the same way as in NPT simulations. After being thermalized in the NVT ensemble with a Langevin thermostat for $2 \times 10^3 \tau^*$, the initially large simulation box is deformed to the volume V_i, and then further equilibrated for $2 \times 10^4 \tau^*$ to obtain the corresponding ensemble averages of pressure P_i^* (see Figure 2.5). The curve at $T^* = 0.68$ in Figure 2.5 resembles a van der Waals loop. However, this curve is a finite-size effect, which means that the loop on this curve will reduce to a flat line in an infinite system at

equilibrium [74]. Negative pressures in the simulations indicate that the system tends to aggregate.

Using the pressure and volume data from Figure 2.5, we computed the relative free energy landscapes for the system with $N_B/N_A = 8$ at different temperatures, as shown in Figure 2.6. To facilitate comparisons between the depths of the free energy wells and thermal fluctuations, the curves are plotted as $F_{rel}/(T^*\varepsilon) = F_{rel}/k_B T$. In thermodynamic integration, the points where the pressure vanishes correspond to extrema in the free energy landscape. Typically, a single zero in pressure corresponds to a single well in the landscape, while three zeros correspond to two wells and a maximum. At both low temperatures ($T^* = 0.3$) and high temperatures ($T^* = 0.8$), the free energy has only one minimum in the compact state, indicating the ionic and superionic phases, respectively. The double-well shape around the transition temperature ($T^* = 0.68$) confirms that sublattice melting is a first-order phase transition when the system is at the optimal stoichiometry. The volumes at the free energy minima are in good agreement with the equilibrium volumes obtained in our previous NPT simulations. It is worth noting that when the free energy has double wells, our NPT simulations tend to sample states with smaller volumes, as we initialized the system in denser configurations.
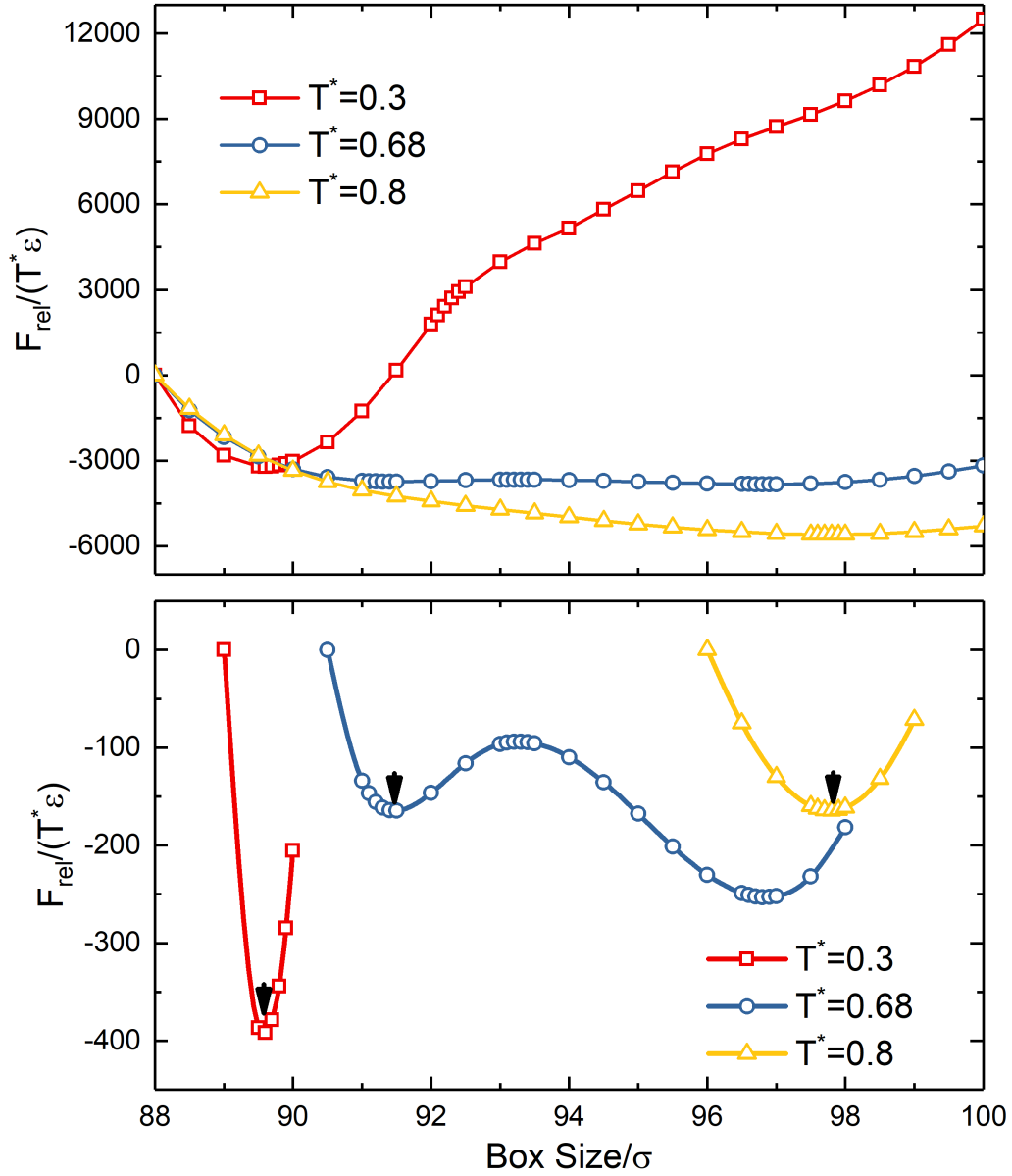
Figure 2.6. Calculations of the relative Helmholtz free energy in the $N_B/N_A = 8$ systems at different temperatures ($T^* = 0.3$, 0.68, and 0.8) via thermodynamic integration methods. (Top) The overall landscape of relative Helmholtz free energy. The reference volume V_0 is $(88\sigma)^3$ for all three temperatures. (Down) Locations of free energy minimums. The reference volumes are $(89\sigma)^3$ for $T^* = 0.3$, $(90.5\sigma)^3$ for $T^* = 0.68$, and $(96\sigma)^3$ for $T^* = 0.8$. Black arrows mark the state sampled by previous NPT simulations.

2.3.3. Phase Coexistence

For $N_B/N_A = 9$ systems, we observe two coexisting ionic phases with local number ratios

of $N_B/N_A = 8$ and $N_B/N_A = 10$, respectively, at low temperatures. As the temperature

increases, each of these phases transitions into superionic phases at different temperatures.

To obtain the local number ratios, we divided the simulation box into small cubic bins,

each of which has 1/8 the volume of the FCC unit cell and is the smallest chemically

identical unit for small particles. After equilibrium, we counted the average number of

small particles in each cube N_B^{local} from 1000 frames taken every 5000 timesteps ($10\tau^*$).

The local number ratio is then given by $N_B/N_A = 2N_B^{local}$ as one cube has 1/2 large

particle. The histogram of local N_B/N_A at different temperatures $T^* = 0.2$, 0.4, and 0.6

combined with corresponding simulation snapshots (Figure 2.7) reveals that at $T^* = 0.2$,

the system consists of two kinds of ionic crystals with stoichiometric ratios $N_B/N_A = 8$ and

$N_B/N_A = 10$, respectively. These two ionic phases are both in micro-size and randomly

mixed up (see Figure 2.11 in the Appendix section of this Chapter). However, because

the $8c$ positions have higher energy than the $32f$ positions, the $N_B/N_A = 10$ ionic phase

has a lower sublattice melting temperature than the $N_B/N_A = 8$ phase. Therefore, when

the temperature is raised to 0.4, the $N_B/N_A = 10$ phase melts into the superionic state,

and we observe the $N_B/N_A = 8$ ionic phases coexisting with superionic phases that have

various local number ratios distributed almost evenly in a wide range. By plotting the

locations of cubes with local $N_B/N_A = 8$, we find that instead of aggregating into a macro-

crystal, these ionic cubes form microphases scattered throughout a percolated structure

of superionic phases (the cluster sizes span from 2 to 6 unit cells in our simulations)

probably to decrease the surface strain generated from the lattice constant mismatch

between the ionic and the superionic phases, as shown in Figure 2.2. Further increasing the temperature melts the sublattice in the $N_B/N_A = 8$ phase, and the whole system forms a homogeneous superionic phase with $N_B/N_A = 9$.

The phase coexistence information indicates that $N_B/N_A = 8$ is the most stable stoichiometric ratio for the ionic phase in FCC crystals. However, it is uncertain whether there is an optimal stoichiometric ratio for the superionic phase without conducting equal chemical potential simulations to account for material exchanges. It is worth noting that with a variety of possible stoichiometric ratios, the system may become a glass state in which the large particles are fixed while the small ones are fluid, as predicted in charge- and size-asymmetric ionic systems with Coulombic interactions [75]. In our current work, we have imposed cubic symmetry and a fixed stoichiometry on the crystal. Therefore, the equilibrium structure may not represent the most stable state when the symmetry restriction and stoichiometric constraint are removed, such as in the case of deformable crystals that can exchange components with the surroundings.
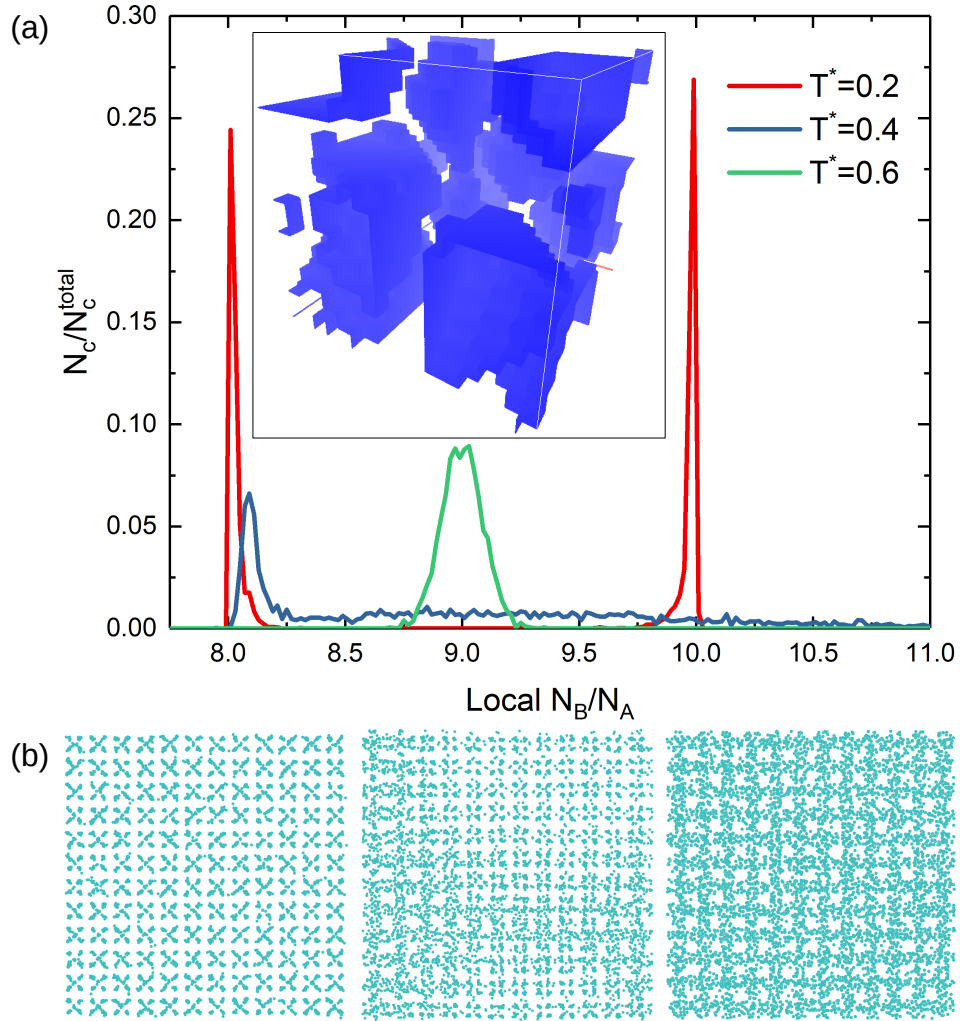
Figure 2.7. Phase coexistence in the system with $N_B/N_A = 9$. To obtain better statistics, we enlarged the simulation box to $8 \times 8 \times 8$ unit cells. (a) The histogram of the average number of small particles in sub-unit cubic bins at different temperatures $T^* = 0.2$, 0.4, and 0.6. N_C is the number of cubes that has a certain local N_B/N_A and N_c^{total} is the total number of cubes which is $16^3 = 4096$ here. (Inset) A three dimensional view of the simulation box showing locations of cubes with local $N_B/N_A = 8$ inside the crystal at $T^* = 0.4$. All the cubes satisfying $|N_B/N_A - 8| < 0.2$ are colored blue while the rest are left blank. (b) Snapshots of the equilibrium distribution of small particles at $T^* = 0.2$ (left), 0.4 (middle), and 0.6 (right).

2.3.4. Discussions on depletion effects

Depletion forces are known to play a role in driving the assembly of mixtures of colloidal particles with different sizes [45, 46]. However, we do not observe these forces playing a significant role in stabilizing the superionic structures found in our simulations. First, in our simulations, we do not include explicit salt that could cause depletion attraction between the nanoparticles [47]. Moreover, in experiments, there is no evidence of monovalent salt-mediated attractions, even in large colloids, provided the colloids have sufficient charge [76], as long as the experiments are performed at 300 mM of NaCl or less. Second, depletion is mainly entropy-driven and should be enhanced by increasing the temperature. However, in our simulations, all colloidal crystals melt into gas phases when the temperature is increased above 1.3, indicating that depletion is not a significant factor in stabilizing the superionic phases. Third, the system is equilibrated at a finite size in our zero-pressure NPT simulations, even though the box size is not constrained. This suggests that the system does not favor adding more free volume for the small particles. The average distance between two neighboring large particles d in our simulations satisfies $2R_A < d < 2\sigma_{AB}$, where $\sigma_{AB} = R_A + R_B$. Although depletion effects can exist when d is in the interval $(2R_A, 2\sigma_{AB})$, the free volume for small particles V_{free} as a function of d in the FCC structure monotonically increases in the interval $(2R_A, 2(R_A + R_B))$. Thus, the colloidal superionic structure is not stabilized at any local maximum of V_{free}.

2.4. Conclusions

To conclude, we have identified a superionic-like crystal structure in size-asymmetric charged colloidal systems where the smaller particles melt and hold the larger particles in

a crystalline lattice via screened Coulomb interactions. By cooling down the system, the small mobile particles condense to interstitial positions, resulting in an ionic-like structure. At the stoichiometric ratio where the number of small colloids equals the number of interstitial positions, this colloidal ionic-to-superionic transition is first order, demonstrated by the discontinuous change in lattice constant and the double-well shape in the free energy landscape. The addition of more small colloids inside the lattice leads to the coexistence of ionic-like domains and percolated superionic-like phases with multiple stoichiometries. This state of the system may provide insights into growing heterostructures. Overall, our findings provide guidelines to assemble metallic or superionic conductor colloidal crystals and set up the foundation for discovering exciting properties and functions of multicomponent colloidal crystals.

2.5. Appendix for Chapter 2

2.5.1. System Size Effects

T	$6 \times 6 \times 6$	$8 \times 8 \times 8$	$10 \times 10 \times 10$
0.1	14.84	14.84	14.84
0.2	14.89	14.89	14.89
0.3	14.93	14.93	14.93
0.4	14.98	14.93	14.93
0.5	15.04	15.04	15.04
0.6	15.12	15.12	15.12
0.65	15.18	15.18	15.18
0.66	15.20	15.20	15.20
0.67	15.22	15.22	15.22
0.68	15.25	15.25	15.25
0.69	15.28	15.28	15.28
0.7	16.17	16.17	16.17
0.8	16.30	16.30	16.30
0.9	16.41	16.41	16.41
1.0	16.56	16.56	16.56

Table 2.1. The equilibrium lattice constants (in σ) obtained in the zero pressure NPT simulations under different temperatures at $N_B/N_A = 8$ using simulation boxes with the sizes $6 \times 6 \times 6$, $8 \times 8 \times 8$, and $10 \times 10 \times 10$ FCC unit cells, respectively. The results are exactly the same regardless of the crystal size.
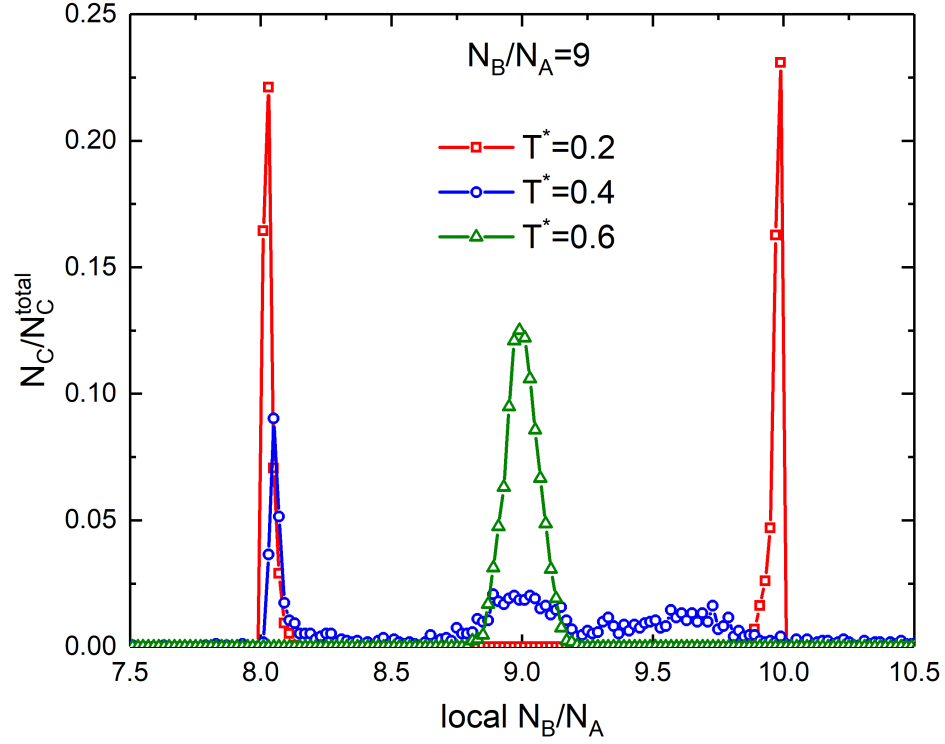
Figure 2.8. The histogram of the average number of small particles in sub-unit cubic bins at $T^* = 0.2$, 0.4, and 0.6 using a $6 \times 6 \times 6$ unit cell simulation box, which is similar to the results obtained from an $8 \times 8 \times 8$ unit cell simulation box in Figure 2.7. Therefore, there are no significant finite-size effects in our results.

2.5.2. The Crystal Melting
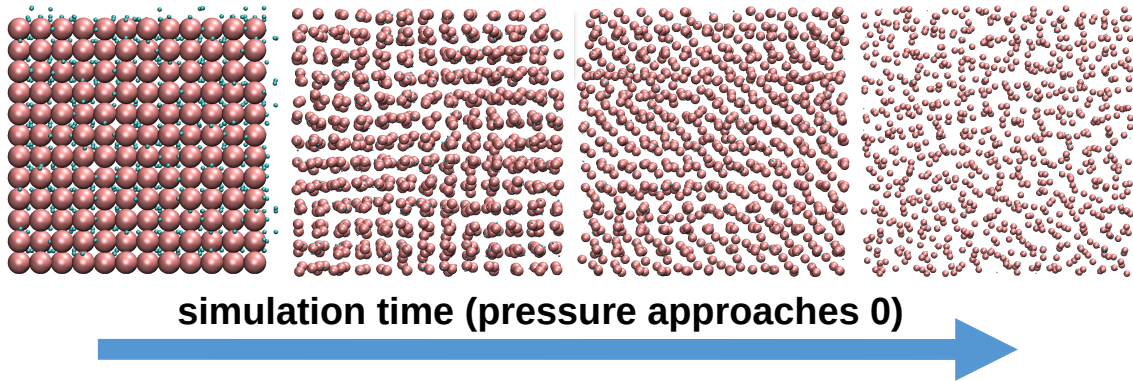
Figure 2.9. The melting process of unstable colloidal crystals as pressure approaches 0 in NPT simulations. The simulation box is expanding to infinity simultaneously; here $\kappa\sigma = 0.1$ and $q_B^* = +11$, $N_B/N_A = 8$, $T^* = 0.3$, and $q_A^* = -247$.

2.5.3. Diffusion Coefficient
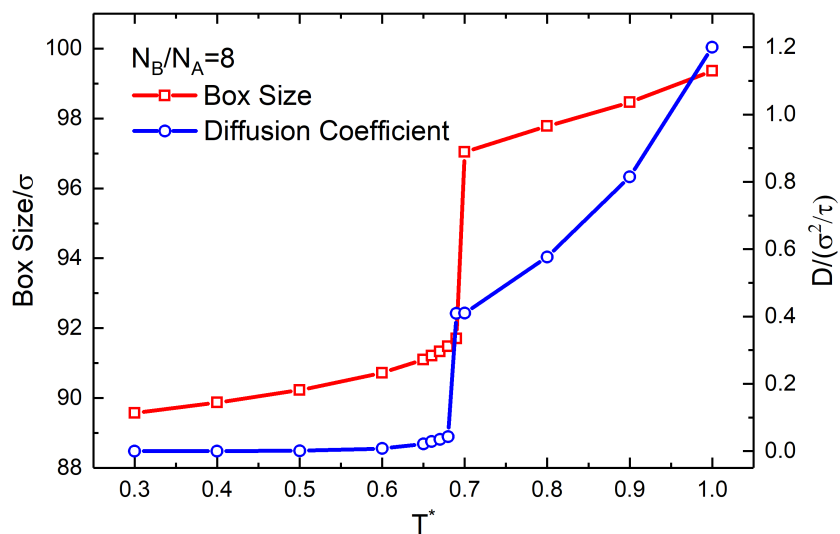
Figure 2.10. The equilibrium box size and the diffusion coefficient of small particles as a function of the temperature at $N_B/N_A = 8$. The diffusion coefficient also leaps at the "ionic-superionic" transition temperature. The diffusion coefficient is calculated from the mean-square-displacement (MSD) of small particles $\langle r(t)^2 \rangle$ over 5×10^6 timesteps using $D = \langle r(t)^2 \rangle / 6t$.

2.5.4. Two Coexisting Ionic Phases

(a)

(b)
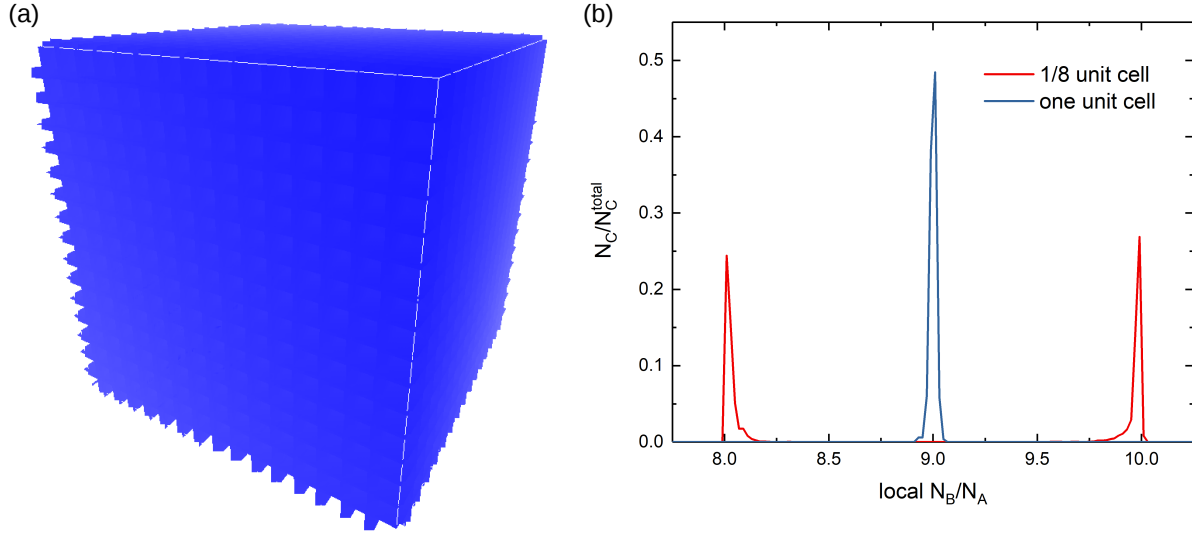
Figure 2.11. The $N_B/N_A = 8$ and $N_B/N_A = 10$ ionic phases both exist as microphases when they coexist (overall number ratio $N_B/N_A = 9$, $T^* = 0.2$). (a) Distribution of sub-unit cubes (1/8 unit cell) with local $N_B/N_A = 8$ in the crystal. All the cubes satisfying $|N_B/N_A - 8| < 0.2$ are colored blue while the rest are left blank. Results show that these $N_B/N_A = 8$ ionic cubes are nearly evenly dispersed within the crystal, hence the whole simulation box is colored blue. This is because at low temperatures the rearrangement of small particles can only happen between two neighboring cubes, i.e., two neighboring cubes with initial local number ratio 9/1 become one 8/1 cube and one 10/1. (b) The local number ratio calculation using two different cube sizes: 1/8 unit cell (red) and one unit cell (blue). The two separate peaks (red) merge into one single peak (blue) when using more coarse grained cubes, showing that these two ionic phases are both in micro–size.

2.5.5. Justification of the parameters

Here we justify that the parameters used in our simulations can be converted to reasonable experimental values, which is helpful for testing our results in experiments. There are many different ways to convert the quantities from the reduced units used in our simulations to the real units, and one possible way of conversions we provide is:

- the distance unit: $\sigma = 1$ nm;

- the reduced temperature: $T^* = T/(428.6\,\text{K})$ where T is the real temperature and K is Kelvin; the transition temperature in $N_B/N_A = 8$ systems is about $T^* \approx 0.7$, and we assume it corresponds to the room temperature, $300\,\text{K}$; hence $T^*/0.7 = T/(300\,\text{K})$ and then $T^* = T/(428.6\,\text{K})$;

- the energy unit: $\varepsilon = k_B \times 428.6\,\text{K} = 5.9 \times 10^{-21}$ J; here $k_B = 1.38 \times 10^{-23}$ J/K is the Boltzmann constant;

- the reduced charge: $q^* = q^r/(0.161\sqrt{\epsilon_r}e)$, where q^r is the real charge, e is the elementary charge, and ϵ_r is the dielectric constant of the media; this relationship is obtained by plugging the above quantities into $q^* = q/\sqrt{4\pi\epsilon_0\epsilon_r\sigma\varepsilon}$;

- the reduced pressure: $P^* = P\sigma^3/\varepsilon = P/(5.9 \times 10^6\,\text{Pa})$ where Pa is Pascal.

From these conversions, we have the particle sizes $R_A = 5\sigma = 5$ nm, $R_B = 1\sigma = 1$ nm, and the screening constant $\kappa = 0.7\,\text{nm}^{-1}$ which corresponds to a $44\,\text{mM}$ NaCl salt solution. For the charges, assuming the media is water and $\epsilon_r = 80$, plugging in $q_A^* = -247, q_B^* = +11$ we have:

$$q_A^r = q_A^*(1 + \kappa R_A)/e^{\kappa R_A} \times 0.161\sqrt{\epsilon_r}e = -48e$$

$$q_B^r = q_B^*(1 + \kappa R_B)/e^{\kappa R_B} \times 0.161\sqrt{\epsilon_r}e = +13e$$

Note that we are using the effective reduced charges, which need to be first converted to the bare charges via DLVO and then further converted to the real charges. In real units, the electrostatic interaction is governed by:

$$(2.6) \qquad U(r_{ij}) = \frac{q_i^r e^{\kappa R_i} q_j^r e^{\kappa R_j} e^{-\kappa r_{ij}}}{4\pi\epsilon_0\epsilon_r(1+\kappa R_i)(1+\kappa R_j)r_{ij}}$$

All the parameters, after being converted into real units, are achievable in experiments. Therefore, in order to verify the ionic-superionic transition found in our simulations, experimentalists can prepare two kinds of particles with these given size and charge values, mix them in a $44\,\mathrm{mM}$ NaCl salt solution, and the transition may be seen at around $300\,K$.

CHAPTER 3

Superionic Transitions in equilibrium with solutions[*]

3.1. Introduction

In Chap. 2, we have shown that the ionic to superionic transition has been observed in simulations of colloidal crystals of oppositely charged and highly size-asymmetric NPs with screened Coulomb interactions [32]. Interestingly, a recent experimental research work combining computer simulations on charged NPs co-assemble with oppositely charged ions via electrostatics [78] confirmed the dynamic diffusion of ions inside the charged NP superstructures. They observed the position exchange of ions from the surface of one NP, through the interface between two NPs, to the surface of another NP. Although the mobile components are ions instead of small NPs, this is still a giant leap toward realizing the superionic phase in colloidal crystals.

To explore the possibilities of assembling superionic conductors in colloidal systems in a more realistic way, we need to study the ionic to superionic transition using Coulomb interactions. This is necessary since the Debye-Hückel approximation and other continuum theories cannot describe dense charged colloidal systems [79, 80, 81, 82] and particularly fail to describe ionic compounds and ion-driven condensation [83]. In addition, experimentally, colloidal crystals are assembled in a colloidal solution. The crystal and the

colloid solution are in dynamic equilibrium. That is to say when the crystal undergoes structural changes or transitions, it needs to re-establish the equilibrium with the solution and its composition should adjust accordingly. In turn, changes in the solution should affect the crystal as well. Simulations and analysis of the ionic-metallic transition in colloidal crystals [32, 63, 64, 66], however, do not consider molecular and/or atomic exchange between the crystal and the solution. That is, the simulations consider an isolated crystalline phase whose composition does not react to changes in the temperature or the solution conditions, whereas the composition of the assembled crystals should be an outcome of the experimental conditions, instead of a controlling parameter.

Plenty of studies have proven that the solution conditions have profound impacts on the materials. In polymer systems with charged monomers, the like-charge repulsions between monomers keep the polymers extended. The addition of salt and the condensation of counterions will screen the repulsions and induce the polymer collapse [83, 84, 85]. More complicated are the hydrogels. Apart from the ion correlations, the salt addition has competing effects on the hydrogel [86]. On the one hand, the hydrogel is compressed due to the increase of the osmotic pressure; on the other hand, the hydrogel swells because of the absorption of more ions as their chemical potentials in the solution increase. It is fascinating that the competition between these two effects is sensitive to the valency of salt ions. A similar competition is expected to exist in our colloidal systems.

In this paper, we study the composition and crystal spacing of a charged colloidal crystal in a solution by imposing equilibrium between the colloidal crystal and the rest of the solution (hereafter referred to as *reservoir*), including the ions explicitly (i.e., using Coulomb interactions) in implicit solvent. Our aim is to reveal how the crystal assemblies

react to external conditions, specifically the temperature and the solution composition. In our MD simulations, we use the restricted primitive model [86, 87] where the charged components interact via Coulomb and hard-core interactions, which has successfully described both ionic and superionic gels [88].

Given the complexity of the multi-component system, it is impossible for our study to cover all adjustable parameters. Compared to the density of small particles, the density of large particles is less important, since studying the phase behavior of large particles is not the focus. Thus, in the simulations, we kept the volume fraction of large NPs in the solution constant at 0.3. This volume fraction is dense enough for NPs to assemble while is still dilute for a solution phase to exist. The small to large charge ratio is $1 : 4$ while the small to large number ratio is always no less than $4 : 1$ so that a necessary number of counterions of small NPs are included to neutralize extra small NPs. No extra salt is added. Therefore, the controlling parameters are the concentration of small NPs in the reservoir, ϕ_s^{res}, and the temperature, T.

We begin by simulating the assembly in the solution to determine the crystallization conditions and the crystal structure. However, the lattice constant and the composition of the crystal are difficult to identify from the assemblies in the solution. Therefore, we continue with osmotic ensemble simulations [86]. That is, we simulate the crystal and the reservoir separately in two boxes, with each box representing a region in the bulk of an infinitely large phase. Due to the presence of excess small NPs, we assume all large NPs crystallize so the amount remaining in the reservoir is negligible. Thus, the reservoir contains only small NPs and counterions, while the crystal contains the large NPs in a particular lattice with small NPs and counterions inside (Figure 3.1A), and the small

NPs and counterions are exchangeable between these two phases. To maintain the charge neutrality, the minimum exchanging unit is one small NP accompanied by its neutralizing counterions, which, for the sake of simplicity, is termed *small NP neutral cluster* and denoted by *sp* hereafter. Phase equilibrium is achieved when the reservoir and the crystal have both equal osmotic pressure and μ_{sp}. We quantify the equilibrium colloidal crystal properties from the crystalline box simulations and observe a discontinuous increase in lattice constant when ϕ_s^{res} or T increases, which represents an ionic to metallic transition.

We also provide a theoretical understanding for the ionic-metallic transition based on free energy calculations. The ionic state in our theoretical model has small NPs located at interstitial sites and randomly hopping among these sites (Figure 3.1B). The metallic state has an even density distribution of small NPs within the lattice (Figure 3.1C). The cohesive energy consists of the lattice vibrational energy obtained from the quasi-harmonic phonon model, and the electrostatic energy, which is computed via Madelung sum calculations for the ionic state and via the Wigner-Seitz cell approach [89, 90, 91] for the metallic state. The entropic term counts for the contribution of delocalized components. We determine the more stable state through the comparison between these two free energies and reproduce the ionic-metallic transition in simulations. The free energy comparison also reveals the driving force of the ionic-metallic transition to be enthalpic instead of entropic.
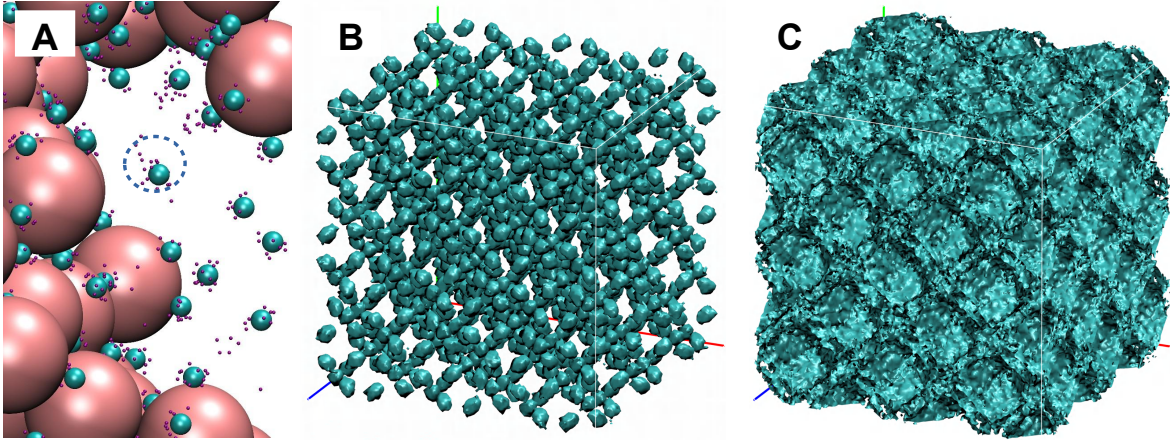
Figure 3.1. Outline for the simulation setup and the theory. (A) the colloidal crystal of large (pink) and small NPs (cyan) is in equilibrium with the reservoir containing excess small NPs and their counterions (purple). These two phases are simulated separately, with the equilibrium characterized by the mechanical equilibrium (equal pressure) and the chemical equilibrium of exchanging small NPs accompanied by neutralizing counterions (as shown in the dashed circle). (B) The density distribution of small NPs shown as cyan isosurface in a $2 \times 2 \times 2$ unit cell ionic FCC crystal, obtained from MD simulations, which will be used as the density distribution function for the ionic state in our model. It covers all the $32f$ and $8c$ Wyckoff positions [32, 71] of the FCC lattice. (C) The density distribution of small NPs in the metallic FCC crystal, which will be used as the density distribution function for the metallic state in our model. The small NPs can access all the free space within the lattice.

In order to be in accordance with the original work [77], we use the term *metallic* instead of *superionic*. In fact, these two terms are not exactly the same and partly capture the phenomena in colloidal systems, respectively. The charged large lattice is held together purely by small NPs carrying opposite charges. This way of aggregation is closer to metals than superionic conductors in which the frame is connected via covalent bonds. In contrast, there are no quantum effects existing in colloidal systems, especially since small NPs cannot actually behave as electrons. Here, in this chapter, *metallic* is used

not only to emphasize the metal-like way of aggregation but also because the Wigner-Seitz cell approach we used in the free energy calculation is a common method to evaluate the electron-nuclei interactions in metal solids [92, 93, 91].

3.2. Methods

3.2.1. Simulation setup

All of our MD simulations are done in the LAMMPS software package [69]. The Coulomb potential is evaluated by the particle-particle particle-mesh (PPPM) method with GPU acceleration [94, 95, 96, 97, 98]. Images of simulation results are created using VMD [99].

In the simulations, we used reduced quantities defined relative to the energy unit ϵ, the distance unit σ, and the mass unit m. The reduced quantities include the reduced temperature $T^* = k_B T/\varepsilon$, reduced pressure $p^* = p\sigma^3/\varepsilon$, reduced time $\tau^* = t\sqrt{\varepsilon/(m\sigma^2)}$, and reduced charge $q^* = q/\sqrt{4\pi\epsilon_0\epsilon_r\sigma\varepsilon}$ with ϵ_0 being the permitivity of the space and ϵ_r being the relative dielectric constant. The solvent is treated as an implicit medium. All the simulations follow Langevin dynamics.

The interaction between a pair of charged particles i and j separated by the vector $\mathbf{r}_{ij}$ (whose magnitude is $|\mathbf{r}_{ij}| = r_{ij}$) is included by a repulsive Weeks-Chandler-Andersen potential (U_{WCA}) and the Coulombic potential (U_{el}) as

$$(3.1) \qquad U_{WCA}(r_{ij}) = \begin{cases} 4\varepsilon\left[\left(\dfrac{\sigma_{ij}}{r_{ij}}\right)^{12} - \left(\dfrac{\sigma_{ij}}{r_{ij}}\right)^{6}\right] + \varepsilon, & r_{ij} < 2^{1/6}\sigma_{ij}. \\ 0, & r_{ij} > 2^{1/6}\sigma_{ij}. \end{cases}$$

$$(3.2) \qquad U_{el}(r_{ij}) = \frac{q_i q_j}{r_{ij}},$$

where σ_{ij} is calculated using the Lorentz-Berthelot mixing rules $\sigma_{ij} = R_i + R_j$. Here, $R_l = 5$, $R_s = 1$, and $R_{ci} = 0.2$ are the radii of the large NPs, small NPs, and counterions, respectively. And the charges are $q_l = -100$, $q_s = +25$, and $q_{ci} = -1$ for the three species. All quantities are expressed in dimensionless reduced units.

3.2.2. Osmotic ensemble simulations

The simulations are conducted in two steps: first, we simulate the whole mixture in the NVT ensemble to obtain a rough phase diagram; second, we simulate the solid phase and the solution phase separately and acquire their equilibrium via the osmotic ensemble simulations.

For the simulations of the whole mixture, we set up the system by randomly initializing a fixed number (80) of large NPs, a certain amount of small NPs (varying by individual simulation), and the necessary amount of neutralizing counterions in a $(50\sigma)^3$ periodic cubic box. The system was then thermalized in the NVT ensemble for $6 \times 10^4 \tau$ to reach equilibrium.

The reservoir is simulated as a $(50\sigma)^3$ periodic cubic box. The small NPs and their counterions are randomly initialized in the box, and the system is run for $5 \times 10^3 \tau$ in the NVT ensemble to reach equilibrium. After equilibrium, we sample the potential energy of each particle every 1τ for 10000 times, which are then input in the calculation of μ_{sp}^{res} using the *real particle method*. The equilibrium osmotic pressure is simply the ensemble average of the virial pressure of the system.

The crystal is simulated as a periodic cubic box consisting of $4 \times 4 \times 4$ FCC unit cells with various stoichiometries n. At each n, we first set up the system by initializing the

large NPs on lattice sites with relatively wide lattice spacing and adding the small NPs as well as the counterions inside the voids. After energetically equilibrating the system using NVE integration for 4τ, we gradually shrink the lattice to a close-packing size and pressurized it at a pressure three times larger than the final pressure for 100τ in the NPT ensemble. The lattice is depressurized 200τ to the final pressure and equilibrated for 6000τ followed by an additional 1500τ for sampling. The potential energy of each small NP and counterion are sampled for calculation of μ_{sp}^{cry} via the *real particle method.*

3.2.3. Real particle method

The chemical potential is calculated via the *real particle method* [100, 101]. It is based on the *Widom test particle deletion method* [102, 70], which gives the chemical potential of a N-particle system as

$$
(3.3) \qquad \mu = k_B T \ln\left(N\Lambda^3/V\right) + k_B T \ln\left\langle \exp\left(\frac{u_N}{k_B T}\right)\right\rangle_N.
$$

Here, $\Lambda = h/\sqrt{2\pi m k_B T}$ is the thermal de Broglie wavelength, where h is the Planck constant and m is the mass of the particle. u_N is the total interaction energy between the selected particle (to be deleted) and the rest $N-1$ particles

$$
(3.4) \qquad u_N = \sum_{i=1}^{N-1} u_{iN}
$$

and $\langle...\rangle_N$ stands for the ensemble average over the N-particle system.

The problem with the deletion method is that [102]: it is not possible to estimate the chemical potential correctly by deleting a particle, due to inefficient sampling of the highly

positive energies felt by the removed molecule which contribute greatly to the chemical potential. Thus, note that each of the N particles in one equilibrium configuration has an equal probability of being deleted, the *real particle method* has

$$(3.5) \qquad \left\langle \exp\left(\frac{u_N}{kT}\right)\right\rangle_N = \sum_{j=1}^{M}\sum_{i=1}^{N} \exp\left(\frac{u_i^j}{kT}\right)/(NM),$$

where M is the number of sampled configurations, and u_i^j is the potential energy of the ith particle in the jth configuration. Eqn. (3.5) uses the properties of all the atoms while requiring no actual trial deletions, and thus it has a much higher sampling efficiency than sampling individual particle deletions.

Insertion methods such as the *Widom test particle insertion method* [70] fail in dense systems due to strong overlaps. The free energy perturbation method [70], or the so-called stage insertion method, experiences large fluctuations in our numerical implementation because results are sensitive to the initial insertion position. Therefore, we chose the *real particle method* for this work.

3.3. Theory

3.3.1. Free energy

We calculate the free energy of the ionic and metallic states as a function of the lattice constant and n to predict which is the equilibrium phase under different environmental conditions. The Gibbs free energy per unit cell is

$$(3.6) \qquad g(N_s, V_c) \equiv G/N_c = \min_{V_c}(f_{id} + f_{el} + f_{vib} + pV_c).$$

Here, N_s is the average number of small NPs per FCC unit cell, V_c is the unit cell size, and N_c is the number of unit cells in the whole crystal. The first term, f_{id}, accounts for the ideal entropic contribution of diffusive particles. The second term, f_{el}, is the electrostatic contribution. The third term, f_{vib}, is the contribution attributed to the thermal vibrations of the lattice.

The state of the crystal, ionic or metallic, can be told from the density distribution of small NPs, $\{\rho(\boldsymbol{r})\}$. To pursue an accurate determination of the density distribution, one may treat the free energy of a functional of $\{\rho(\boldsymbol{r})\}$. By minimizing $G(\{\rho(\boldsymbol{r})\})$ (locally or globally) with respect to $\{\rho(\boldsymbol{r})\}$, the equilibrium $\{\rho(\boldsymbol{r})\}$ can be identified. The resulting $\rho(\boldsymbol{r})$ is likely to be a mixed state of ionic and metallic where small NPs are diffusive while staying at the interstitial sites for a longer time. Such mixed states are what have been observed in experiments [62, 65] and simulations [63, 64, 32]. However, these calculations require solving the Poisson equation in a dense system, which still lacks an analytical way so far. To avoid the lengthy iterative numerical computation, we assume only two possible equilibrium density distributions, $\{\rho_I\}$ and $\{\rho_M\}$, for the ionic and metallic states, respectively, as shown in Figure 3.1(b) and 3.1(c). The counterions are assumed to be delocalized (fully mobile) in both states. The small NPs in the metallic state are assumed to have a homogeneous distribution in the unoccupied space inside the crystal, while in the ionic phase, they are assumed to have an equal probability to appear at any interstitial site. These approximations allow us to evaluate the free energy analytically in a simple manner.

In the following three subsections, we sequentially present the calculations of f_{id}, f_{el}, and f_{vib}, based on $\{\rho_I\}$ and $\{\rho_M\}$.

3.3.2. The ideal term.

In the ionic state, counterions are moving in a free space $V_f^I = V_c - N_l v_l - N_s v_s$ where v_l and v_s are the volumes of individual large and small NP, respectively. In the metallic state, both small NPs and counterions are moving in a free space $V_f^M = V_c - N_l v_l$. Therefore, we have

$$(3.7) \qquad \beta f_{id}^I = N_{ci}(\ln\rho_{ci}^I - 1),$$

$$(3.8) \qquad \beta p_{id}^I = \rho_{ci}^I,$$

$$(3.9) \qquad \beta \mu_{id}^I = |q_s|\ln\rho_{ci}^I,$$

and

$$(3.10) \qquad \beta f_{id}^M = N_{ci}(\ln\rho_{ci}^M - 1) + N_{sp}(\ln\rho_s^M - 1),$$

$$(3.11) \qquad \beta p_{id}^M = \rho_{ci}^M + \rho_s^M,$$

$$(3.12) \qquad \beta \mu_{id}^M = |q_s|\ln\rho_{ci}^M + \ln\rho_s^M,$$

where $\rho_{ci}^I = N_{ci}/V_f^I$, $\rho_{ci}^M = N_{ci}/V_f^M$, and $\rho_s^M = N_s/V_f^M$, with ci standing for *counterions*.

3.3.3. The electrostatic term.

The ionic state in our theoretical model is that with large NPs being fixed at lattice sites, small NPs hop among the $8c$ and $32f$ Wyckoff interstitial sites with an equal visiting probability, while counterions freely roam in the crystal voids. For a crystal with a given n, each interstitial site has on average $4n/N_{int}$ small NPs and $4(n-c)|q_s|/N_{int}$ counterions in its vicinity, where $c = |q_l/q_s| = 4$ is the large to small NP charge ratio and $N_{int} = 40$ is the number of interstitial sites per unit cell. We average these $4n/N_{int}$ small NPs and $4(n-c)|q_s|/N_{int}$ counterions into a *pseudo particle*, which has a charge $q_{ps} = -4q_l/N_{int}$, and assume the system to be a crystal compound of large NPs and these pseudo particles located at interstitial sites. As a result, the electrostatic energy is separated into the interaction between large NPs and pseudo particles and the internal energy of pseudo particles. The first term can be obtained via Madelung sum calculations, where the Madelung constants for large NP lattice sites, the $8c$ sites, and the $32f$ sites are, respectively, given as

$$(3.13) \qquad M_l = \sum_{r_{ijk}\in\Omega_{l,l}} \frac{q_l}{r_{ijk}/a} + \sum_{r_{ijk}\in\Omega_{l,32f}} \frac{q_{ps}}{r_{ijk}/a} + \sum_{r_{ijk}\in\Omega_{l,8c}} \frac{q_{ps}}{r_{ijk}/a},$$

$$(3.14) \qquad M_{32f} = \sum_{r_{ijk}\in\Omega_{32f,l}} \frac{q_l}{r_{ijk}/a} + \sum_{r_{ijk}\in\Omega_{32f,32f}} \frac{q_{ps}}{r_{ijk}/a} + \sum_{r_{ijk}\in\Omega_{32f,8c}} \frac{q_{ps}}{r_{ijk}/a},$$

$$(3.15) \qquad M_{8c} = \sum_{r_{ijk}\in\Omega_{8c,l}} \frac{q_l}{r_{ijk}/a} + \sum_{r_{ijk}\in\Omega_{8c,32f}} \frac{q_{ps}}{r_{ijk}/a} + \sum_{r_{ijk}\in\Omega_{8c,8c}} \frac{q_{ps}}{r_{ijk}/a}.$$

Here, $\Omega_{\alpha,\alpha'}$ is the infinite set of coordinates of all α' positions when setting the α position as the origin. The Madelung constants are numerically evaluated via Eqns. (3.13), (3.14), and (3.15) and given by $M_l = 501.4$, $M_{32f} = -26.26$, and $M_{8c} = -55.42$ (details are provided in Table 3.1 in the Appendix section of this Chapter).

The internal energy of a pseudo particle, u_{ps}, includes the attraction between $4n/N_{int}$ small NP and $4(n-c)|q_s|/N_{int}$ surrounding counterions, as well as the repulsion among these counterions. We use a characteristic length, L_{ps}, for the interaction inside pseudo particles. We approximate $N_{int}(L_{ps})^3 = V_c$ since the total interaction volume of all pseudo particles is the unit cell. Then, the internal energy of pseudo particles per unit cell is estimated as

$$
\begin{aligned}
U_{ps} \equiv N_{int}u_{ps} &= \frac{N_{int}}{L_{ps}}\left[\left(\frac{4n}{N_{int}}q_s\right)\frac{4(n-c)q_sq_i}{N_{int}} + \frac{16(n-c)^2q_s^2q_i^2}{2\times N_{int}^2}\right] \\
&= -\frac{8q_s^2(n^2-c^2)}{N_{int}^{2/3}}V_c^{-1/3}.
\end{aligned}
$$

(3.16)

Therefore, the electrostatic energy per unit cell is given as

(3.17)
$$
f_{el}^I = \left[C_I - \frac{8q_s^2(n^2-c^2)}{N_{int}^{2/3}}\right]V_c^{-1/3}
$$

with

(3.18)
$$
C_I = -\frac{1}{2}(4q_lM_l + 32q_{ps}M_{32f} + 8q_{ps}M_{8c}) = -106698.7,
$$

and, correspondingly

(3.19)
$$
p_{el}^I = \frac{\partial f_{el}^I}{\partial V_c} = \frac{1}{3}\left[C_I + \frac{8q_s^2(n^2-c^2)}{N_{int}^{2/3}}\right]V_c^{-4/3},
$$

$$(3.20) \qquad \mu_{el}^I = \frac{\partial f_{el}^I}{N_l \partial n} = -\frac{4q_s^2 n}{N_{int}^{2/3}} V_c^{-1/3}$$

In the metallic phase, we use the Wigner-Seitz (WS) cell approach [91, 90] to evaluate the electrostatic energy. A WS cell is the space surrounded by the planes perpendicularly bisecting the lines connecting the nearest large NPs. For an FCC crystal, each WS cell is a charge-neutral dodecahedron, containing one large NP at the center and a homogeneous oppositely charged background together formed by n small NPs as well as $(n - c)q_{sp}$ counterions. The electrostatic energy can be then divided into two terms: the self energy in each dodecahedron and the interactions between dodecahedra. The self energy of one dodecahedron is given as

$$
\begin{aligned}
U_{self} =& q_l \sum_j q_j \int_{cell} \frac{\mathrm{d}\boldsymbol{r}_j}{r} + \sum_j q_j \sum_{k \neq j} q_k/2 \iint_{cell} \frac{\mathrm{d}\boldsymbol{r}_j \mathrm{d}\boldsymbol{r}_k}{|\boldsymbol{r}_j - \boldsymbol{r}_k|} \\
=& -q_l^2 D_1 + \sum_j q_j(-q_l - q_j) D_2/2 \\
=& -q_l^2 (D_1 - D_2/2) - \sum_j q_j^2 D_2/2,
\end{aligned}
$$

(3.21)

where the sum goes through all delocalized particles (small NPs and counterions) inside one Wigner-Seitz cell, and

$$(3.22) \qquad D_1 = \int_{cell} \frac{\mathrm{d}\boldsymbol{r}}{r} = 3.80249 V_c^{-1/3},$$

$$(3.23) \qquad D_2 = \iint_{cell} \frac{\mathrm{d}\boldsymbol{r} \mathrm{d}\boldsymbol{r}'}{|\boldsymbol{r} - \boldsymbol{r}'|} = 3.02998 V_c^{-1/3}.$$

Substituting D_1 and D_2, Eqn. (3.21) becomes

$$(3.24) \qquad U_{self} = \left\{ -2.29 q_l^2 - 1.51 n q_s^2 - 1.51(n-4)|q_s| \right\} V_c^{-1/3}.$$

The interactions between nearest-neighbor (NN) WS cells are explicitly written as

$$(3.25) \qquad U_{NN} = \sqrt{2} q_l^2 V_c^{-1/3} - 2 q_l^2 D_3 + q_l^2 D_4,$$

and

$$(3.26) \qquad D_3 = \int_{cell} \frac{d\boldsymbol{r}}{|\boldsymbol{r} - \boldsymbol{x}/\sqrt{2}|} = 1.42197 V_c^{-1/3},$$

$$(3.27) \qquad D_4 = \iint_{cell} \frac{d\boldsymbol{r} d\boldsymbol{r}'}{|\boldsymbol{r} - \boldsymbol{r}' - \boldsymbol{x}/\sqrt{2}|} = 1.42191 V_c^{-1/3},$$

where $\boldsymbol{x}/\sqrt{2}$ is the displacement between the centers of mass of two neighboring large NPs, with $|\boldsymbol{x}|$ equal to the lattice constant. Therefore, we have

$$(3.28) \qquad U_{NN} = -7.19 \times 10^{-3} q_l^2 V_c^{-1/3}.$$

Since each WS cell is in contact with 12 other WS cells, there are $12 \times 4/2 = 24$ pairs of NN interactions in one FCC unit cell. In sum, the electrostatic energy is

$$(3.29) \qquad f_{el}^M = 4 U_{self} + 24 U_{NN},$$

and correspondingly,

(3.30)
$$p_{el}^{M} = -\frac{\partial f_{el}^{M}}{\partial V_c},$$

(3.31)
$$\mu_{el}^{M} = \frac{\partial f_{el}^{M}}{N_l \partial n}.$$

3.3.4. The lattice vibrational term.

Lastly, we consider the excluded-volume effect of the lattice which generates the inner pressure that balances the attractive electrostatic interactions. We use the classical phonon model to describe the thermal vibrations of the lattice and calculate the inner pressure. Following the Grüneisen equation of states [90], the free energy of the lattice attributed to vibrations is given as

(3.32)
$$\beta F_{vib} = \sum_{\boldsymbol{q},s} \left\{ \frac{1}{2}\beta\hbar\omega_s(\boldsymbol{q}) + \ln\left(1 - e^{-\beta\hbar\omega_s(\boldsymbol{q})}\right) \right\}$$
$$= \int_0^\infty \left\{ \frac{1}{2}\beta\hbar\omega + \ln\left(1 - e^{-\beta\hbar\omega}\right) \right\} \rho(\omega)\mathrm{d}\omega.$$

Here, $\hbar = h/2\pi$ with h being the Planck constant, $\boldsymbol{q}$ is the wavevector, $\omega_s(\boldsymbol{q})$ is the phonon frequency of the s-th vibrational mode as a function of $\boldsymbol{q}$, and $\rho(\omega)$ is the density of states for phonons in continuous form. The Grüneisen parameter, γ, describes how ω changes with the lattice volume

(3.33)
$$\gamma = -\frac{\mathrm{dln}\omega_s(\boldsymbol{q})}{\mathrm{dln}V},$$

which Grüneisen assumed is a common constant for all vibrational modes. That is to say

$$(3.34) \qquad\qquad \omega(V_c) = \xi V_c^{-\gamma},$$

where ξ is a constant coefficient. Experimental measurements of γ in various crystals usually give $1 \leq \gamma \leq 3$ [90]. In our system, the vibrational pressure is governed by the volume excluding force, $F_{WCA} = -\partial U_{WCA}/\partial r \propto r^{-13}$. Thus, according to the virial theorem, we have

$$(3.35) \qquad\qquad p_{vib} \propto \langle \boldsymbol{r} \cdot \boldsymbol{F}_{WCA} \rangle \propto r^{-12} \propto V_c^{-4},$$

which gives $\gamma = 3$.

In order to evaluate Eqns. (3.32), we assume that $\rho(\omega)$ possesses the form identical to the classical Debye model:

$$(3.36) \qquad\qquad \rho(\omega) = \begin{cases} \dfrac{N_c N_{dof} \omega^{1/\gamma - 1}}{\gamma \omega_m^{1/\gamma}}, & \omega \leq \omega_m. \\[2em] 0, & \omega > \omega_m. \end{cases}$$

where ω_m is the cutoff frequency and N_{dof} is the total degrees of freedom (DOF) in one unit cell. Substituting Eqn. (3.36) into Eqn. (3.32) and using the low-temperature limit that $\beta\hbar\omega \gg 1$ (the equation under the high-temperature limit is discussed in Subsection 3.6.6 in the Appendix section of this Chapter, which is not coordinated with our results), we obtain the lattice vibrational free energy per unit cell as

$$(3.37) \qquad\qquad \beta f_{vib} \approx \frac{\beta\hbar N_{dof}}{2(\gamma + 1)}\omega_m = \frac{A(n)}{\gamma} V_c^{-\gamma},$$

where we use $\omega_m = \xi_m V_c^{-\gamma}$ from Eqn. (3.34), and

$$(3.38) \qquad A(n) = \frac{\gamma N_{dof} \beta \hbar \xi_m}{2(\gamma + 1)},$$

where the n-dependency comes from N_{dof}. Correspondingly,

$$(3.39) \qquad \beta p_{vib} = A(n) V_c^{-\gamma - 1},$$

$$(3.40) \qquad \beta \mu_{vib} = \frac{\mathrm{d}A(n)}{\mathrm{d}n} \frac{V_c^{-\gamma}}{N_l \gamma}.$$

Ideally, N_{dof} equals the product of the dimensionality and the total number of particles in the lattice, but our crystal is more complicated because of particle hopping and the coupling between mobile particles (small NPs and counterions) and phonons. Thus we evaluate $A(n)$ by fitting it to simulation data of pressure and the results match well with Eqn. (3.39) (see Figure 3.13 and Table 3.2 in the Appendix section of this chapter).

3.4. Results and Discussions

3.4.1. Crystallization

In the simulations of the whole colloidal system, we observe that at low temperatures and low small to large number ratios N_s / N_l, the large NPs aggregate with the small NPs via electrostatic attractions. We analyze the radial distribution function between large NPs, $g_{ll}(r)$, and confirm that the first four peaks in $g_{ll}(r)$ match the typical peak positions of FCC crystals (Figure 3.2(a) and 3.2(b)). When we increase the temperature (comparing Figure 3.2(a) and 3.2(c)) or add more small NPs into the system (comparing Figure

3.2(b) and 3.2(c)), the peaks in $g_{ll}(r)$ gradually become smooth (liquid-like). Simulation snapshots show, in this process, the melting of the crystal (Figure 3.3(a)) to a gel/liquid-like state (Figure 3.3(b)). This is either due to enhanced thermal motion, or enhanced screening effects that weaken the electrostatic attractions [103]. The latter often causes the re-dissolution of ionic-driven assemblies in the absence of short-ranged attractions between components [104, 105].
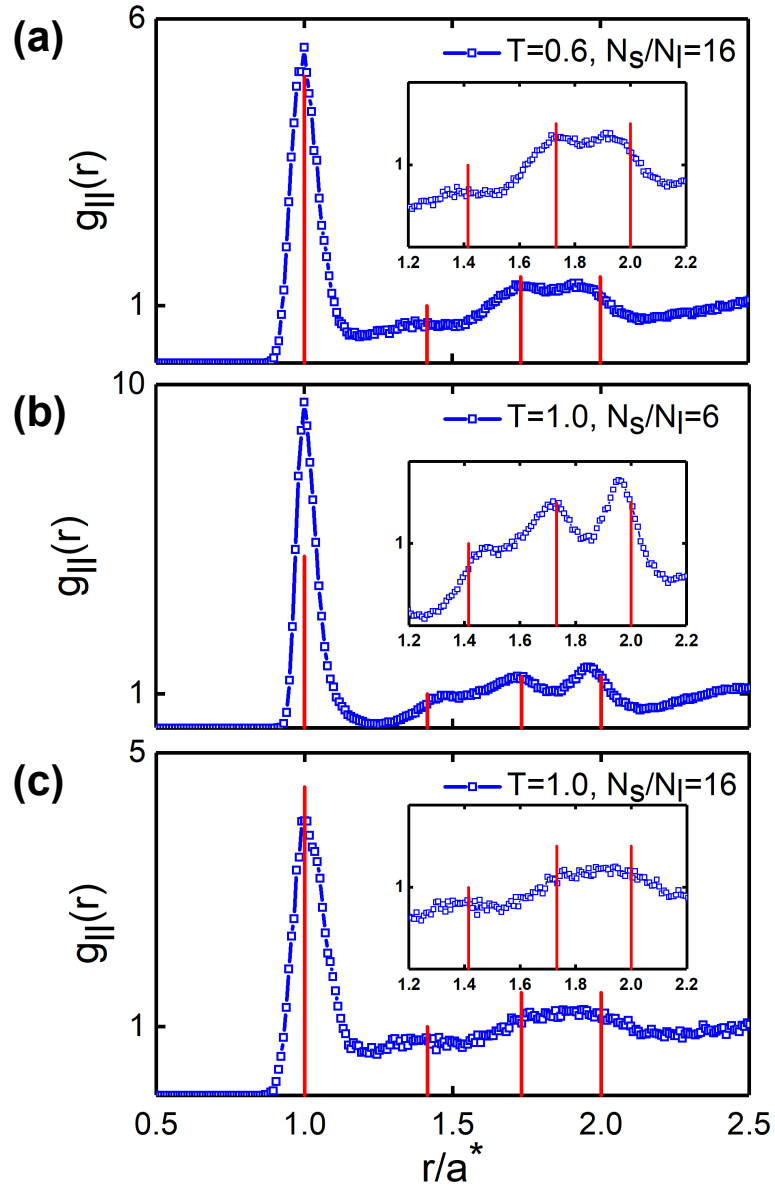
Figure 3.2. The $g_{ll}(r)$ in three equilibrium systems of binary charged colloidal systems with varying temperature and small to large number ratio N_s/N_l: (a) $N_s/N_l = 16$ and $T = 0.6$, (b) $N_s/N_l = 6$ and $T = 1.0$, and (c) $N_s/N_l = 16$ and $T = 1.0$. The distances are scaled by a^*, which is the position of the first peak in each $g_{ll}(r)$. The red lines mark the first four peak positions in a typical FCC crystal, at $r/a^* = 1, \sqrt{2}, \sqrt{3}$, and 2.

Based on $g_{ll}(r)$, a schematic phase diagram as a function of T and ϕ_s^{res} is shown in Figure 3.4. In the NVT simulations, we are able to control the overall N_s/N_l but not the concentration of small NPs in the solution. In addition, it is difficult to unambiguously decide if a small NP at the interface belongs to the reservoir or the crystal. Therefore, we obtain ϕ_s^{res} in Figure 3.4 by estimating it as a linear function of N_s/N_l (for details, see the discussion in Subsection 3.6.1 in the Appendix section of this Chapter). This is only to provide an approximate density regime of crystallization for later simulations. The roughness of the estimation has little impact on our results.

(a) **(b)**
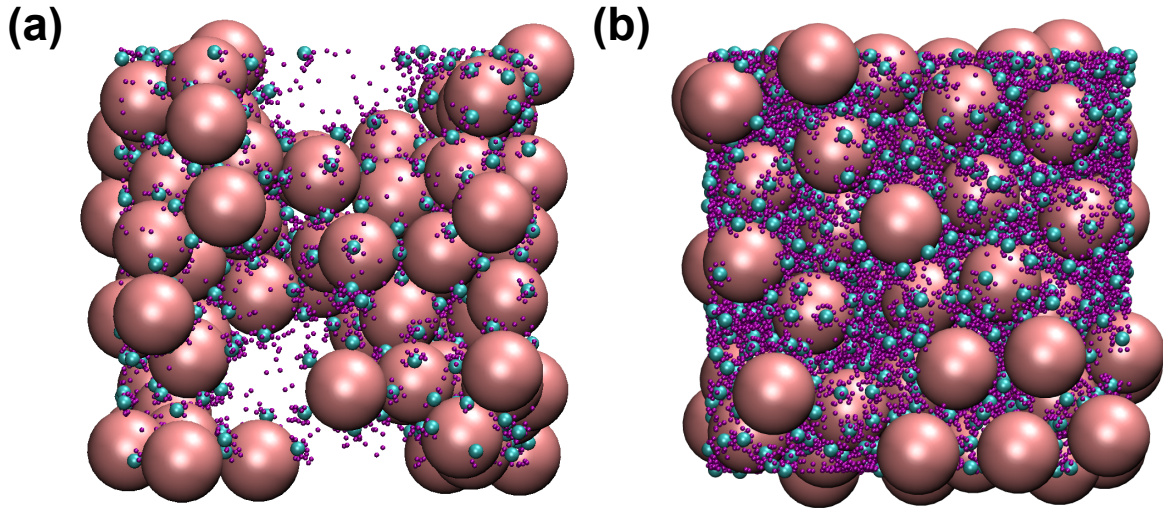
Figure 3.3. The transition from ionic bondings to metallic bondings in the colloidal crystal as the solution concentration of small NPs increases. (a) A snapshot of the FCC crystal, taken in the system with $N_s/N_l = 6$ and $T = 1.0$, using the same color scheme as in Figure 3.1. And (b) a snapshot of the *gel/liquid* phase, taken in the system with $N_s/N_l = 16$ and $T = 1.0$.

We also observe that in low-number ratio systems ($N_s/N_l = 4$), the small NPs barely move inside the crystal, but in high-number ratio systems ($N_s/N_l = 10$), the small NPs are able to roam inside the crystal. Similar transitions are observed when the temperature

increases. This supports the existence of an ionic-metallic transition in the forming of crystals. To explore the transition more quantitatively, we perform osmotic ensemble simulations, which simulate the bulk of the reservoir and the crystal separately.
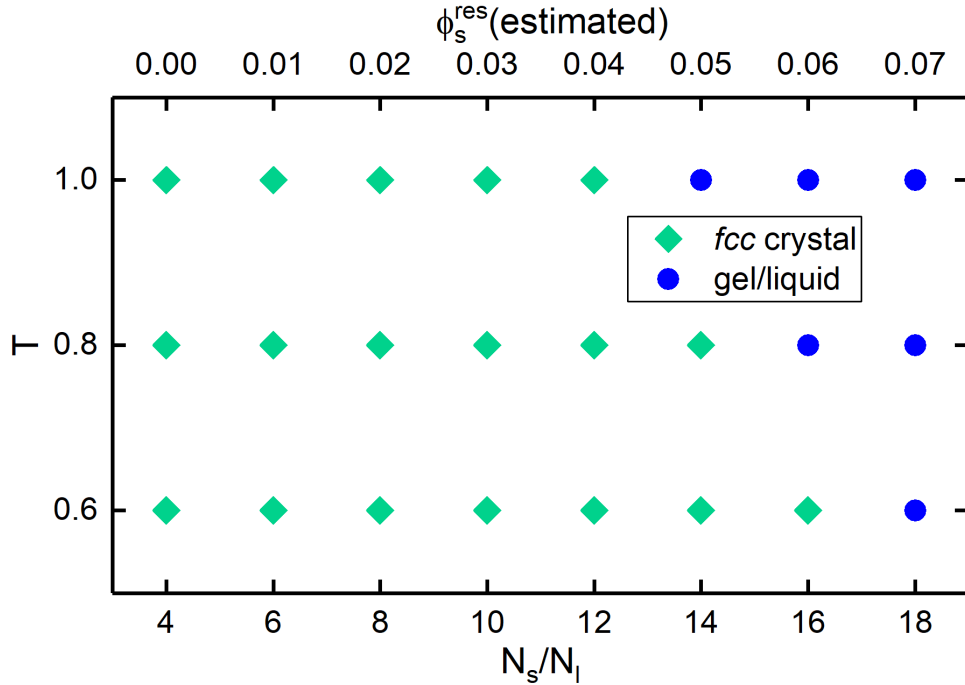
Figure 3.4. A schematic phase diagram of the oppositely charged size-asymmetric colloidal systems with $q_l : q_s = -100 : +25$ as a function of temperature and small NP density in the reservoir. The large NP density is fixed at 0.3. The terms *fcc crystal* and *gel/liquid* refer to the state of the large NPs.

3.4.2. Reservoir phase

Figure 3.5 shows the canonical ensemble (NVT) simulation results on the reservoir containing only small NPs and counterions. The osmotic pressure p grows nearly linearly with the concentration of small NPs under all three temperatures simulated, as expected.

The small NP neutral cluster, one small NP and its neutralizing counterions, is the smallest unit for the material exchange. The chemical potential of a cluster is the sum of that of every particle, $\mu_{sp} = \mu_s + |q_s|\mu_{ci}$, where μ_s and μ_{ci} are the chemical potential for the small NPs and counterions, respectively. As ϕ_s^{res} increases, μ_{sp}^{res} initially increases and slowly flattens, and at low T seems to even decrease. The non-monotonic behavior of μ_{sp}^{res} at large ϕ_s^{res} at $T = 0.6$ in Figure 3.5 is due to the electrostatic repulsion among counterions. The electrostatic repulsion is the main factor that raises μ_{sp}^{res}, saturating at a certain concentration. Above this concentration, μ_{sp}^{res} drops as the attractions between the small NPs and counterions dominate (see Figure S2 for more details).
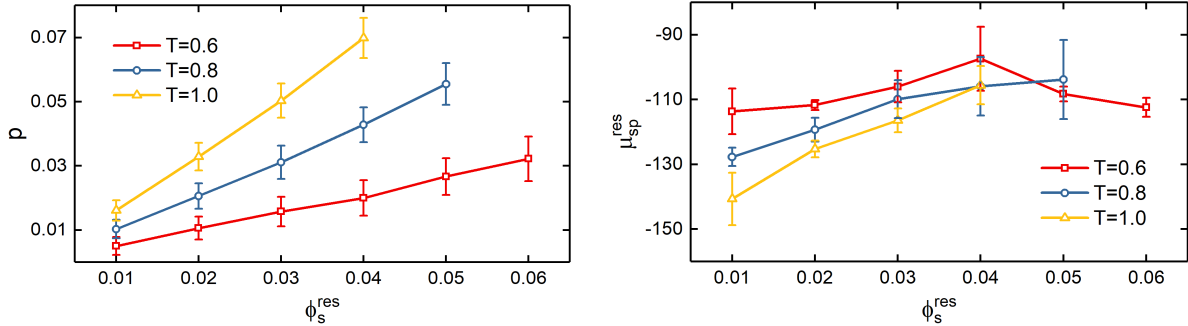
Figure 3.5. The NVT ensemble simulation results for the reservoir. (Left) the equilibrium osmotic pressure, and (right) the chemical potential of small NP neutral clusters under different ϕ_s^{res} and T. Each data point comes from the average of three parallel runs.

3.4.3. Crystalline phase.

Unlike the reservoir phase whose composition can be tuned freely, the crystalline phase is subjected to external constraints. Hereafter, we use n to stand for a reduced stoichiometry notation of a binary compound AB_n, where A and B are the large and small components, respectively. We tune n of the crystal and calculate the chemical potential of small

NP neutral clusters inside the crystal, μ_{sp}^{cry}. Note that the pressure has been already equalized since we use p in the reservoir in the NPT simulations of the crystal. Thus, when μ_{sp}^{cry} equals μ_{sp}^{res} shown in Figure 3.5 (see Figure S3 for details of how we determine the equalizing point), we acquire the equilibrium crystals under given conditions (T and ϕ_s^{res}). As a result, the equilibrium stoichiometries n^{eq} and the equilibrium lattice constants a^{eq} are also obtained.
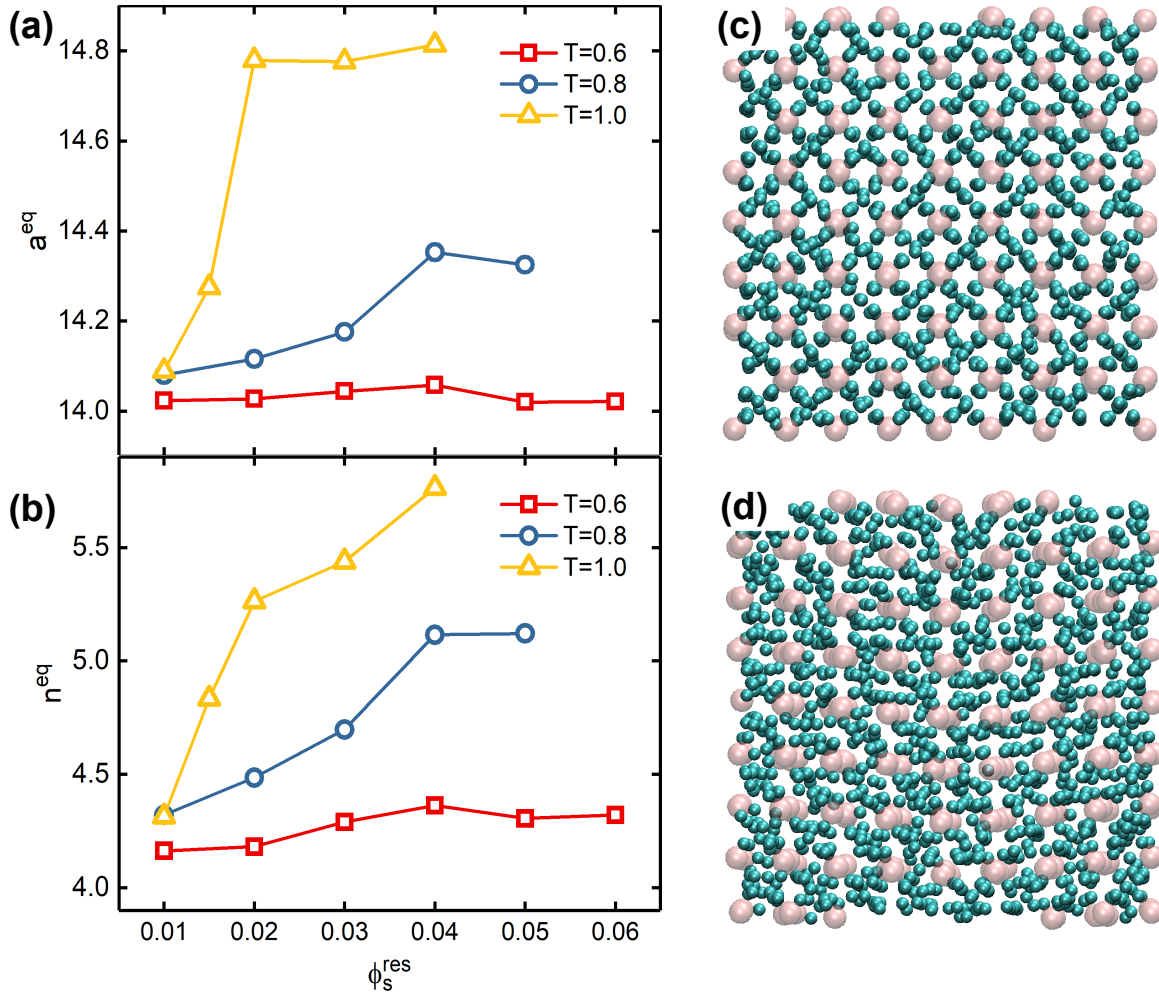
Figure 3.6. The osmotic ensemble simulation results for the crystal. (a) the equilibrium lattice constants of the crystal, and (b) the equilibrium small to large NP ratio inside the crystal; (c) a snapshot of the crystal in equilibrium with the reservoir with $T = 1.0$ and $\phi_s^{res} = 0.01$, where the large particles are presented in reduced size and counterions are not shown for better visualization, and (d) a snapshot of the crystal in equilibrium with the reservoir with $T = 1.0$ and $\phi_s^{res} = 0.02$.

Both n^{eq} and a^{eq} as functions of ϕ_s^{res} under different T are shown in Figure 3.6(a) and

3.6(b). When ϕ_s^{res} increases, additional small NPs get into the crystal at equilibrium as

the chemical environment becomes less favorable for them in the reservoir. The lattice

constant also increases with ϕ_s^{res}, and we show in the theory section that this is a conse-
quence of enhanced lattice vibration caused by increasing T or ϕ_s^{res}. However, the lattice
expansion is not always smooth. In Figure 3.6(a), we observe that the lattice constant has
a rapid increase and then flattens. Such a discontinuous pattern is often an indicator of a
first-order phase transition, which in our system is the ionic-metallic transition. Snapshots
of the lattice verify the fact that the small NPs are located at the interstitial sites before
the rapid lattice expansion (Figure 3.6(c)), as is characteristic of ionic compounds, and
after the expansion, the small NPs become delocalized (Figure 3.6(d)). Meanwhile, the
lattice in the metallic state experiences larger vibration and distortion while maintaining
the FCC structure, which is also found in NPs with grafted linkers interacting with large
NPs [63, 64]. Based on the equilibrium configurations of the crystal, we further divide
the FCC phase in Figure 3.4 into the ionic and metallic states (Figure 3.7).
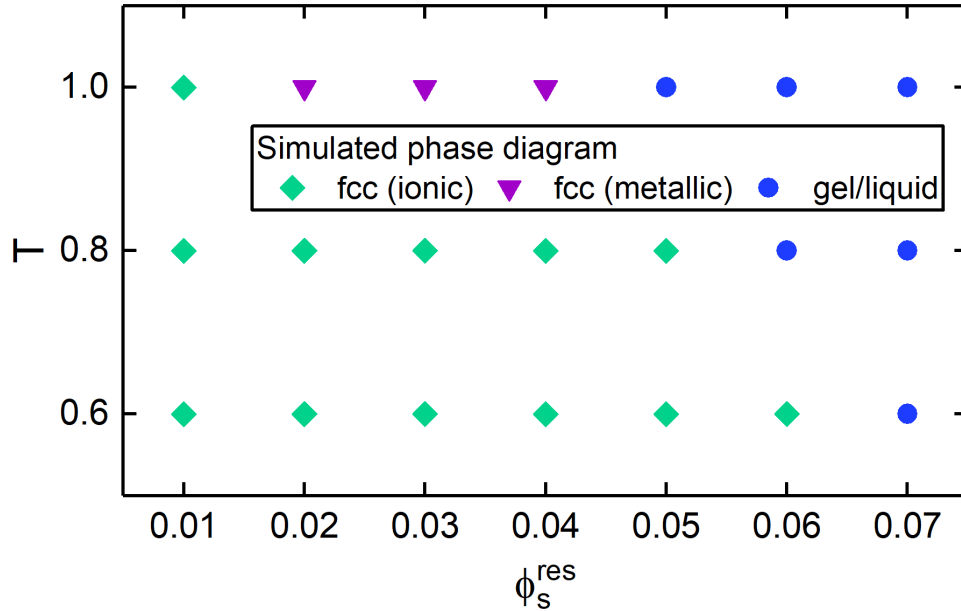
Figure 3.7. A schematic phase diagram of the oppositely charged size-asymmetric colloidal systems as a function of temperature and small NP density in the reservoir obtained by the osmotic simulations. The terms FCC crystal and *gel/liquid* refer to the state of the large NPs.

Lattice expansion is commonly observed during the delocalization of small particles. In charged colloidal systems, computer simulations always predict the lattice expansion during delocalization to be discontinuous, no matter if the electrostatic interactions are modeled as screened [32] or not (in the present work). On the contrary, in the DNA-functionalized NP systems where the attractions between large and small NPs come from the hybridization of their grafted complementary DNA strands, the lattice expansion tends to be smooth unless a change in lattice structure takes place [62, 63, 64, 65]. One possible reason is that, compared to charged colloidal crystals, the coherent energy of functionalized colloidal crystals is less sensitive to changes in the lattice constant. This

is not only because the repulsions between large NPs are short-ranged (mostly hard-cored), but also because the end-to-end interactions between large and small NPs are less influenced by the particle distance due to the flexibility of DNA strands.

Computer simulations show that high temperature and high small NP density in the reservoir both can induce the metallic state. Although the reasons behind this are complicated, our analytical results described below explain them. Temperature-induced transitions may occur due to the entropy gain from delocalized particles, or enhanced lattice vibrations. The density-induced transition may occur because the metallic state becomes more stable as more small NPs are squeezed into the crystal, yet how this effect competes with increasing osmotic pressure which suppresses the lattice expansion and hence favors the ionic state is still unclear.

3.4.4. Analytical results

We calculate the free energies, the pressure, and the chemical potential of the small NP neutral cluster for the ionic and the metallic states for given n and V_c using the theoretical model in the *Methods* section. We obtain the equilibrium number ratio n^{eq} and the equilibrium lattice constant a^{eq} by analytically solving the equations

$$(3.41) \qquad \frac{\partial g}{\partial N_s} = \mu_{sp}^{res},$$

$$(3.42) \qquad \frac{\partial g}{\partial V_c} = 0,$$

or

$$(3.43) \qquad p = -\frac{\partial f_{id}}{\partial V_c} - \frac{\partial f_{el}}{\partial V_c} - \frac{\partial f_{vib}}{\partial V_c} = p_{vib} + p_{id} + p_{el},$$

where the reservoir constraints $\{\mu_{sp}^{res}, p\}$ are acquired from the NVT simulations of the reservoir in Figure 3.5.

The change of n^{eq} is similar to the change of μ_{sp}^{res} with respect to ϕ_s (Figure 3.8(a)) because more small NPs are squeezed into the crystal when the reservoir becomes less favorable to the small NPs. In contrast, a^{eq} (Figure 3.8(b)) varies little with ϕ_s^{res} because a tiny change in volume can cause a large pressure change. However, it increases profoundly with the temperature, as p_{id} and p_{vib} both scale with temperature. The crystal expansion with increasing temperature induces a larger n^{eq} shown in Figure 3.8(a). Note that under the same external conditions, the metallic crystals always have a larger cell size than the ionic crystals due to their stronger lattice vibrations (i.e. inner pressure). As a result, the metallic crystals are able to accommodate more small NPs at equilibrium. Meanwhile, $n_M^{eq} > n_I^{eq}$ is also a reason for the transition, as additional small NPs and their counterions screen and weaken the interactions between the large and small NPs, which in part causes the sublattice melting. The effect that weak bondings or shallow potential energy wells within the lattice of large particles aid the small particles to delocalize via thermal motions has been reported in other works [62, 63, 64, 106, 65] introduced in Chap. 2.
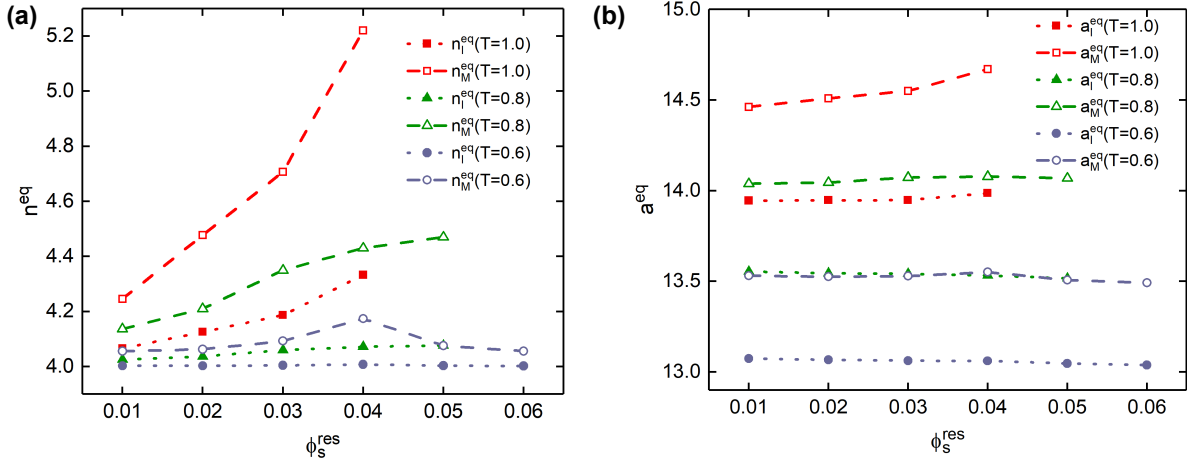
Figure 3.8. Analytical solutions of the Gibbs free energy equalities Eqns. (3.41) and (3.42). (a) the equilibrium number ratio n^{eq} for the ionic and metallic crystals in response to various reservoir small NP densities ϕ_s^{res} at different temperatures, and (b) the corresponding equilibrium lattice constant a^{eq} for the ionic and metallic crystals.

From the equilibrium external variables n^{eq} and a^{eq} (which gives V_c^{eq}), we calculate the free energies of an ionic crystal g_I^{eq} and a metallic crystal g_M^{eq} with those properties. The state with lower free energy is the actual equilibrium state of the crystal. The difference between the ionic and metallic states' free energies is given by

$$
\begin{aligned}
\Delta g^{eq} &= g_I^{eq}(n_I^{eq}, a_I^{eq}) - g_M^{eq}(n_M^{eq}, a_M^{eq}) + N_l(n_M^{eq} - n_I^{eq})\mu_{sp}^{res} \\
&= \Delta f_{id}^{eq} + \Delta f_{vib}^{eq} + \Delta f_{el}^{eq} + p\Delta V_c^{eq} + \mu_{sp}^{res}\Delta N_s^{eq},
\end{aligned}
$$
(3.44)

where the third term on the right-hand side of the first equation accounts for the fact that the transition between the two states is accompanied by absorbing/expelling small NP neutral clusters in/out of the crystal, and thus it allows us to compare the free energies on the basis of an equal number of particles. The second equation divides Δg^{eq} into individual terms as the free energy difference in the ideal term, the vibrational term, the

electrostatic term, the mechanical work term, and the material exchanging term with $\Delta N_s^{eq} = N_l(n_M^{eq} - n_I^{eq})$, enabling us to identify the key factor responsible for the ionic-metallic transition. With $\Delta g^{eq} < 0$ indicating the ionic state is more stable and vice versa, Figure 3.9 shows that the increase in temperature and the increase in ϕ_s^{res} both favor the metallic state, hence can induce the ionic-metallic transition.
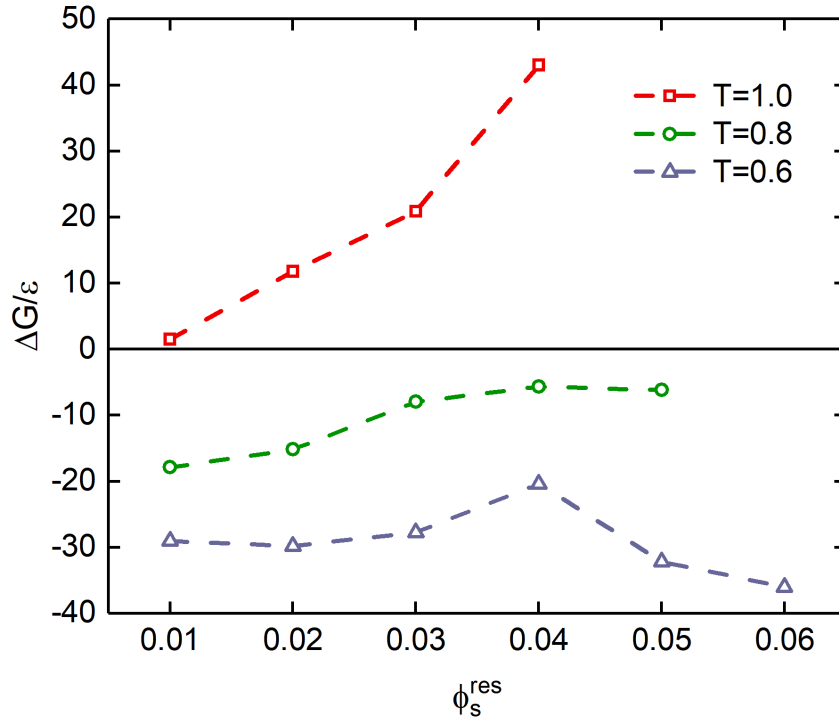
Figure 3.9. The free energy difference between the ionic and metallic states $\Delta g^{eq} = g_I^{eq} - g_M^{eq}$ calculated from Eqn. (3.44).

An analysis of each term in free energy difference in Eqn. (3.44) at different temperatures $T = 0.6$, 0.8, and 1.0 and at a fixed $\phi_s^{res} = 0.03$ is shown in Figure 3.10(a). It reveals that the ionic state has lower electrostatic free energy (Δf_{el}^{eq}), as the small NPs locating at the interstitial sites tends to maximize their Coulombic interaction with the large NPs. Also, the mechanical work term $p\Delta V_c^{eq}$ favors the ionic state, as well as the

material exchanging term $\mu_{sp}^{res}\Delta N_s^{eq}$, because the equilibrium ionic crystal always has a smaller size and a smaller number ratio than the equilibrium metallic crystal under same conditions. Meanwhile, the metallic state has lower ideal free energies (Δf_{id}^{eq}) as it has more delocalized particles and hence larger entropy. The lattice vibrational energy term Δf_{vib}^{eq} also favors the metallic state mainly due to a larger crystal spacing size.

The terms Δf_{id}^{eq} and $\mu_{sp}^{res}\Delta N_s^{eq}$ dominate and have opposite signs, showing a competition between small NPs staying in the reservoir and delocalizing inside the crystal. However, the sum of these two terms is close to zero and barely changes with the temperature, meaning that the free energy loss of additional small NPs leaving the reservoir is well compensated by their delocalization inside the crystal. Thus, the entropic effect is not the driving force for the temperature-induced transition. Instead, we attribute the transition to the increase of Δf_{el}^{eq}, which is a result of n_M^{eq} growing faster with temperature than n_I^{eq} as shown in Figure 3.8(a).
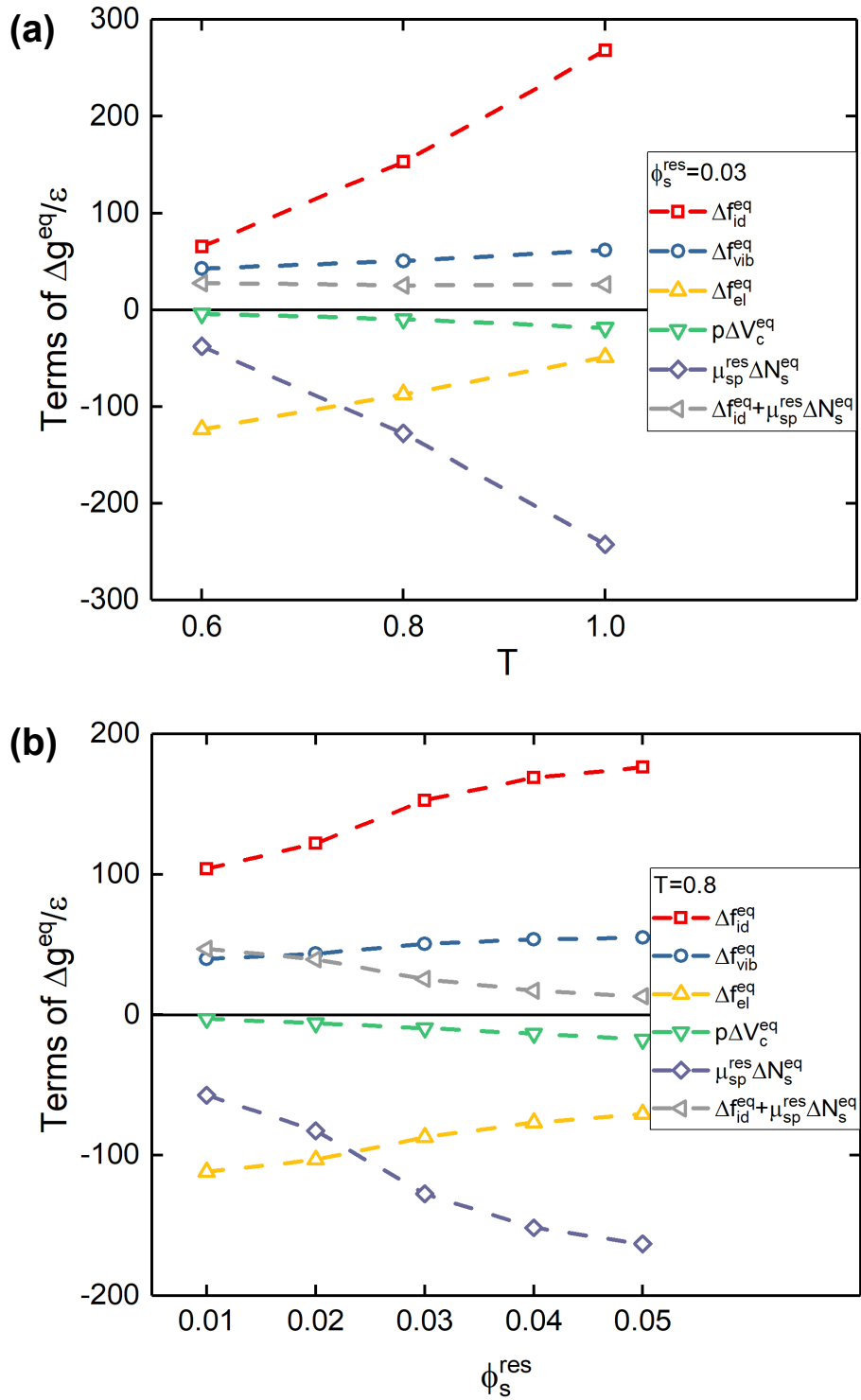
Figure 3.10. An analysis of each term in free energy difference between the ionic and metallic states. (a) Changes with the temperature at a fixed reservoir small NP density $\phi_s^{res} = 0.03$, and (b) changes with ϕ_s^{res} at a fixed temperature $T = 0.8$.

Akin to the temperature-induced transition, the increase of Δf_{el}^{eq} is also the main driving force for the density-induced transition, as shown in Figure 3.10(b). Therefore, we summarize the mechanism of the ionic-metallic transition as that, both temperature and the reservoir density increases can cause a more pronounced rise in stoichiometry in the metallic state than in the ionic state, and consequently, the metallic state has a lower cohesive energy disadvantage which finally makes it the more stable state.

We re-plot the results of the state with lower free energy in Figure 3.9 to provide a phase diagram obtained by theory, shown in Figure 3.11. Comparing Figure 3.11 with the phase diagram obtained from simulation in Figure 3.7 shows that the calculation of the electrostatic interactions using our theoretical model and approximations is reasonable. However, the linear relation between the vibrational pressure and the temperature in the phonon model tends to overestimate the coefficient of thermal expansion of the lattice. Consequently, the theoretically computed lattice sizes are generally smaller than the ones obtained in simulations, and hence the number ratio.
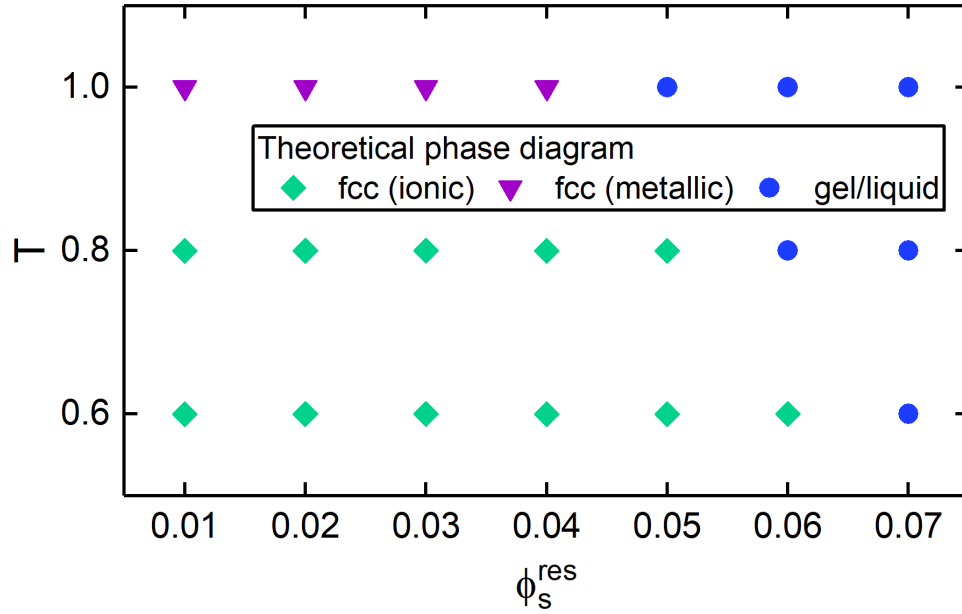
Figure 3.11.   The theoretical phase diagram based on the free energy calculations.

3.5. Conclusions and outlooks

Here, we show that an oppositely charged, size-asymmetric binary colloidal suspension undergoes an ionic-metallic bonding transition as the temperature or the concentration of small NPs increases. In the ionic phase, the large NPs form an FCC lattice with the small NPs occupying the interstitial sites. In the metallic state, the small NPs are delocalized within the crystal while maintaining the integrity of the lattice. This transition is first order, characterized by a discontinuous lattice expansion and a discontinuous change in the stoichiometry of the small to large NPs. The calculations of the free energy of the crystal predict the ionic-metallic transition. We uncover that, with material exchanges, the driving force for the transition is an enthalpic instead of an entropic effect, as the

entropy loss by absorbing additional small NPs from the reservoir into the crystal and the entropy gain from the sublattice melting cancel each other out.

Our work shows that when a colloidal crystal is in contact with a reservoir, the reservoir condition can affect the metallization of the crystal via the osmotic pressure and the material exchanges. In the work discussed in this chapter, we raise the chemical potential of the small NP in the reservoir by increasing their concentration. In experiments, this can be achieved in more complex ways such as using chemical reactions. Our work suggests that chemical reactions that control the chemical potential of the components, can be used to induce or suppress the ionic-metallic transition.

We have assumed a salt-free condition in order to reduce the complexity. Future studies on systems including additional salt should be needed since such systems are closer to experiments. Salt concentration can influence the phase behaviors in a charged colloidal suspension in a fascinating way. It has been reported [103] that gradually increasing the salt concentration induces transitions of colloidal particles from electrostatically aggregated gels, to energy-driven crystals mediated by the screening of salt ions, back to the disaggregated state because of overly strong screening, and finally to closely packed crystals driven by depletion forces. Therefore, we expect that salt would have more complicated competing impacts on the crystals and the ionic-metallic transition.

3.6. Appendix for Chapter 3

3.6.1. Estimation of the volume fraction of small particles in the reservoir

The goal of this subsection is to estimate the boundary of ϕ_s^{res} between the crystal phase and the gel phase of large NPs. We begin with the estimation of the volume of the crystal of large NPs in Figure 3.4. Note that we have 80 large particles with a radius of 5σ in a cubic simulation box with a volume $(50\sigma)^3$, where σ is the unit length. Assuming all large NPs aggregate into a close-packed FCC crystal whose packing fraction is known as 0.74, the crystal formed by 80 large NPs occupies a volume of $(80 \times 4/3\pi \times 5^3/0.74 = 56605)\sigma^3$. The rest of the space in the simulation box is considered as the reservoir, whose volume is $(50^3 - 56605 = 68395)\sigma^3$. Further, we assume the stoichiometry of small to large particles in the assembled crystal deviates little from $4:1$, which is the large to small charge ratio. As a result, the number of small NPs remaining in the reservoir is $80(N_s/N_l - 4)$. Hence, we can estimate the volume fraction of small particles in the reservoir as

$$(3.45) \qquad \phi_s^{res}(N_s/N_l) = 80(N_s/N_l - 4)v_s/(68395\sigma^3) \approx 0.005(N_s/N_l - 4),$$

where $v_s = 4\sigma^3/(3\pi)$ is the volume of an individual small NP with a radius of 1σ.

3.6.2. Nonlinearity of μ_{sp}^{res} in the reservoir at $T = 0.6$

Figure 3.12 provides insights in the non-monotonicity of μ_{sp}^{res} at $T = 0.6$ shown in Figure 3.5. Figures 3.12(a) and 3.12(b) show that the non-monotonicity is not due to the clustering of small NPs. Figure 3.12(c) reveals that as ϕ_s^{res} increases, both the repulsion among counterions and the attraction between small NPs and counterions increase, resulting in

the rise of μ_{ci}^{res} and the drop of μ_s^{res}. The repulsion among counterions first dominates at low ϕ_s^{res}. Hence, we see that μ_{sp}^{res} increases with ϕ_s^{res}. However, after the repulsion saturates above a certain concentration, μ_{sp}^{res} decreases as the attraction becomes more dominant.
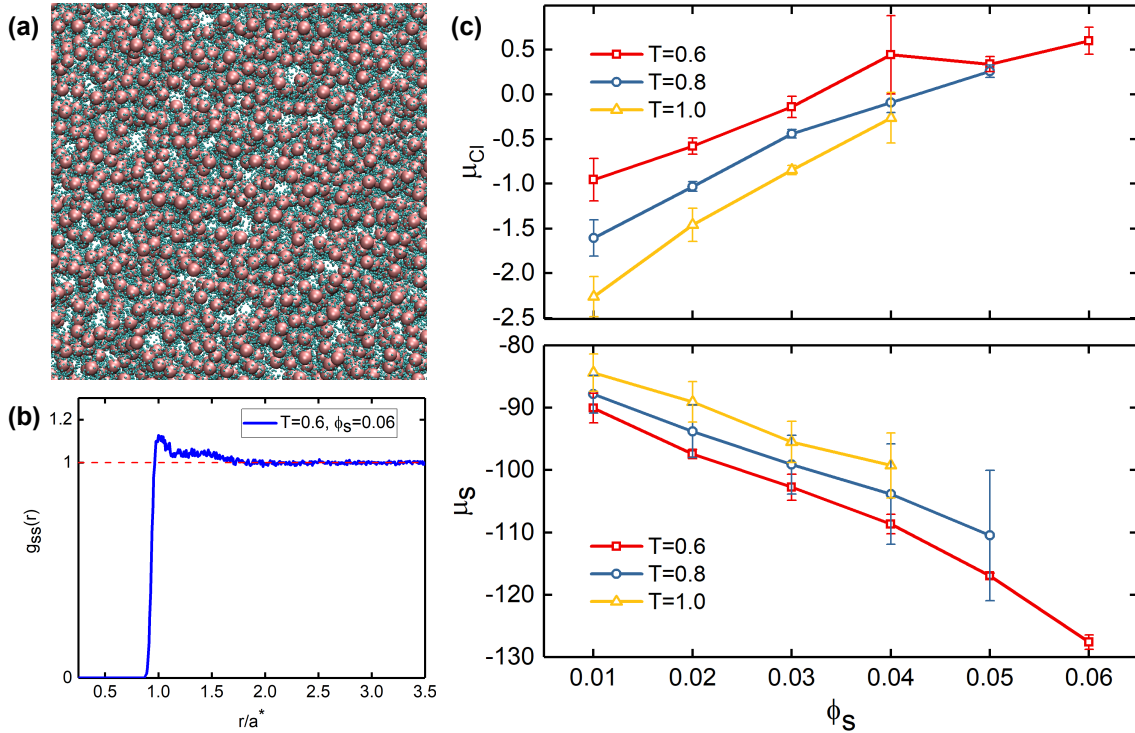
Figure 3.12. (a) The snapshot of the equilibrium system at $T = 0.6$ and $\phi_s^{res} = 0.06$, with the small NPs shown as pink spheres and the counterions shown as cyan spheres, where no clear aggregation of small NPs is found, and (b) the corresponding radial distribution function of small-small NPs, where a^* is the position of the first peak, indicating a gas-like distribution of the small NPs. (c) The changes of individual chemical potentials of counterions and small NPs, μ_{ci}^{res} and μ_s^{res}, with the small NP concentration at different temperatures.

3.6.3. Evaluation of the Madelung constants

We evaluate the Madelung constants using the numerical summation of Eqns. (3.13), (3.14), and (3.15). As the distance of a unit cell to the center increases, its structure details (charge arrangement) become negligible and contribute little to the summation. All three summations converge at a cutoff distance of 300 unit cell lengths. Their values are mainly contributed to by neighboring unit cells.

D_{cut}/a	1	3	10	30	100	300
M_l	501.688	501.326	501.398	501.401	501.401	501.401
M_{32f}	-26.2263	-26.2541	-26.2597	-26.2599	-26.2599	-26.2599
M_{8c}	-55.5864	-55.4064	-55.4222	-55.4229	-55.4229	-55.4229

Table 3.1. Direct summation for three Madelung constants with different cutoff lengths up to 300 lattice constants.

3.6.4. Numerical fitting of $A(n)$

The numerical fitting is based on the Eqn. (3.39) with $\gamma = 3$. We calculate p_{vib} from $p_{vib} = p - p_{id} - p_{el}$. Here, p is the overall pressure of the crystal which is obtained from a series of NVT simulations of the crystal with various n and a (Figure 3.13(a)). Note that the loop in the $p - V$ curves implies the existence of a phase transition, which is the ionic-metallic transition in our system. Thus, p^I is acquired from the $p - V$ curves before the loop, and p^M is acquired from the curves after the loop. The terms p_{id}^I, p_{id}^M, p_{el}^I, and p_{el}^M are calculated from Eqns. 5, 8, 16, and 27 in the main article, respectively.

The linear fitting of $\ln p_{vib}$ versus $\ln V_c$ with $\gamma = 3$ shown in Figures 3.13(b) and 3.13(c) support the accuracy of Eqn. (3.39). Figure 3.13(d) shows that both $A_I(n)$ and $A_M(n)$ are linear functions of n, as expected that the degrees of freedom of lattice vibration should linearly grow with the number of particles. Thus, we have

$$(3.46) \qquad \beta p_{vib}^I = A_I(n) V_c^{-4},$$

$$(3.47) \qquad \beta p_{vib}^M = A_M(n) V_c^{-4},$$

where the exact expressions for $A(n)$ are given in Table 3.2.

Via Eqns. (3.46) and (3.47), we calculate p_{vib} at other temperatures from the fitting results at one reference temperature ($T = 1.0$ in our work). From Eqn. (3.40) and Table 3.2, the vibration contributed chemical potentials are given as

$$(3.48) \qquad \beta \mu_{vib}^I = \frac{1.937 \times 10^{12} V_c^{-4}}{N_l},$$

$$(3.49) \qquad \beta \mu_{vib}^M = \frac{1.849 \times 10^{12} V_c^{-4}}{N_l}.$$
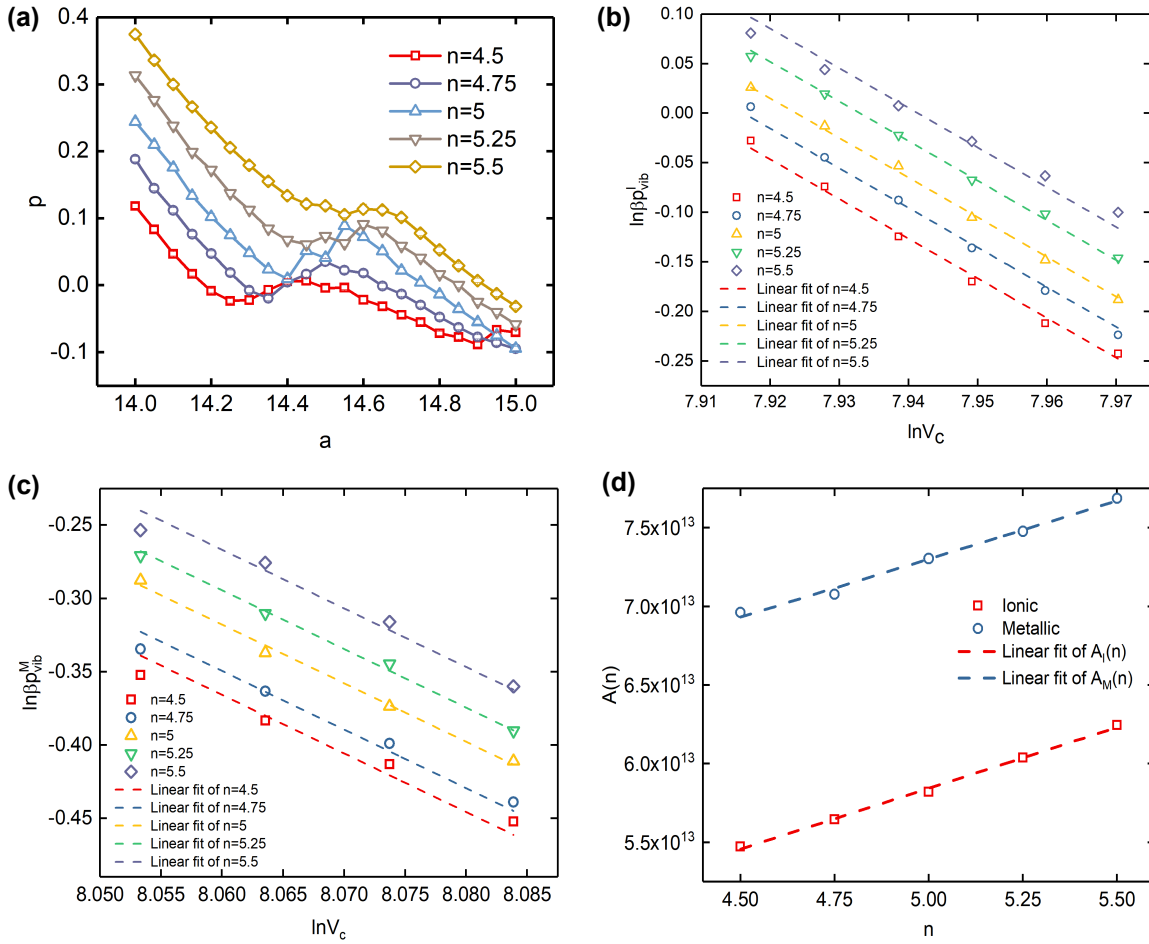
Figure 3.13. The fitting results for the lattice vibrational pressure. (a) the simulated equilibrium pressure of the crystal with different n and a at $T = 1.0$. (b)(c) The linear fitting of $\ln p_{vib}$ versus $(\gamma + 1)\ln V_c$ with $\gamma = 3$, where the intercepts give the prefactors $A(n)$. (d) Linear fitting results for $A(n)$ of the ionic and metallic states. The exact values of $A(n)$ from the fitting are shown in Table 3.2.

n	4.5	4.75	5	5.25	5.5
$\ln A_I$	31.63344	31.66445	31.69496	31.7319	31.76534
$A_I(n)$	$A_I(n) = 1.97 \times 10^{13} + 7.749 \times 10^{12} n$				
$\ln A_M$	31.87428	31.89058	31.92219	31.94556	31.97324
$A_M(n)$	$A_M(n) = 3.605 \times 10^{13} + 7.395 \times 10^{12} n$				

Table 3.2. $A(n)$ of the ionic and metallic states for different stoichiometries n, from the fitting results in Figure 3.13.

3.6.5. Osmotic simulations of the colloidal crystals

Figure 3.14 shows the details of how we obtain the equilibrium between the crystal and the reservoir simulations. First, we simulate the reservoir under given $\{T, \phi_s^{res}\}$ to obtain the osmotic pressure p^{res} and the chemical potential of neutralized small NP pairs μ_{sp}^{res}, as shown in Figure 3 in the main article. Then, we simulate the crystals with different small to large number ratio (stoichiometry) n in the NPT ensemble with $p = p^{res}$. After equilibration, the lattice constant is calculated via ensemble averaging, and the chemical potential of neutralized small NP pairs inside the crystal (μ_{sp}^{cry}) is calculated by the *real particle method*. Two curves, μ_{sp}^{cry} on the left y-axis and a on the right y-axis are plotted with respect to n in Figure 3.14. The intersection between the horizontal line $\mu = \mu_{sp}^{res}$ on the left y-axis and the μ_{sp}^{cry} curve gives us the equilibrium stoichiometry n^{eq} where the chemical equilibrium is reached between the crystal and the reservoir. The intersection between the vertical line $n = n^{eq}$ and the a curve gives us the equilibrium lattice constant a^{eq}.

(a)
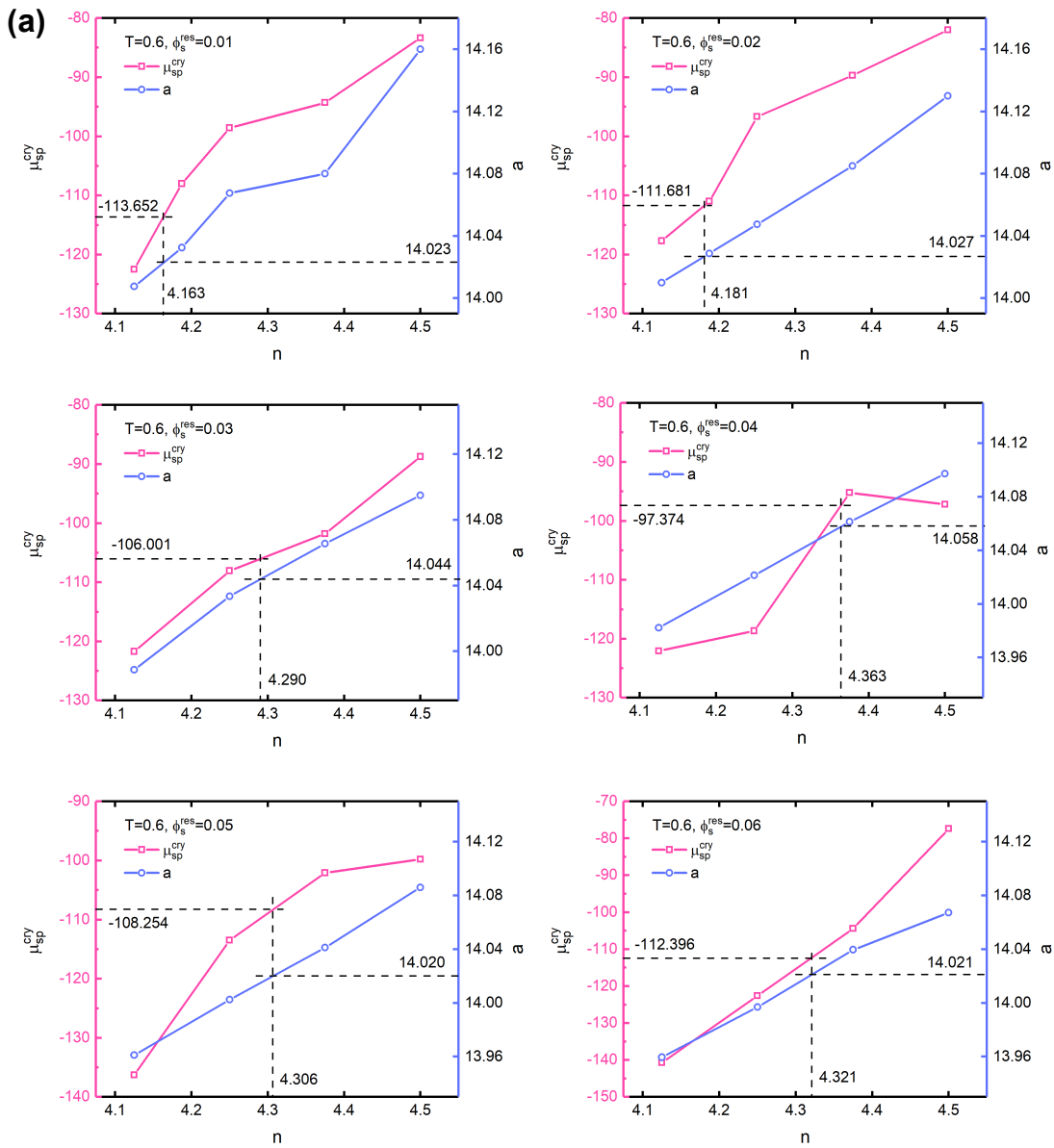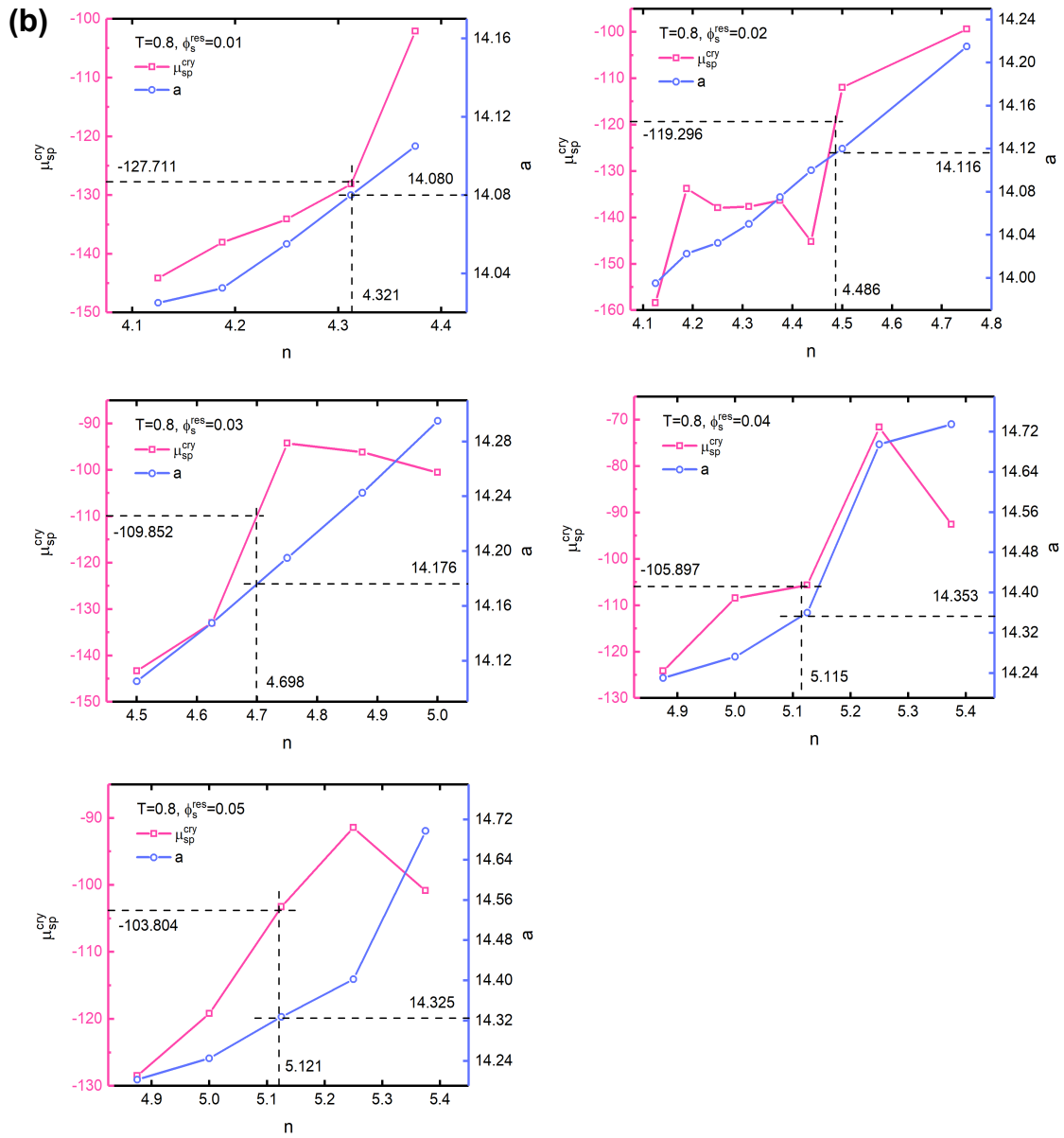
(Figure continues)

(Figure continues)
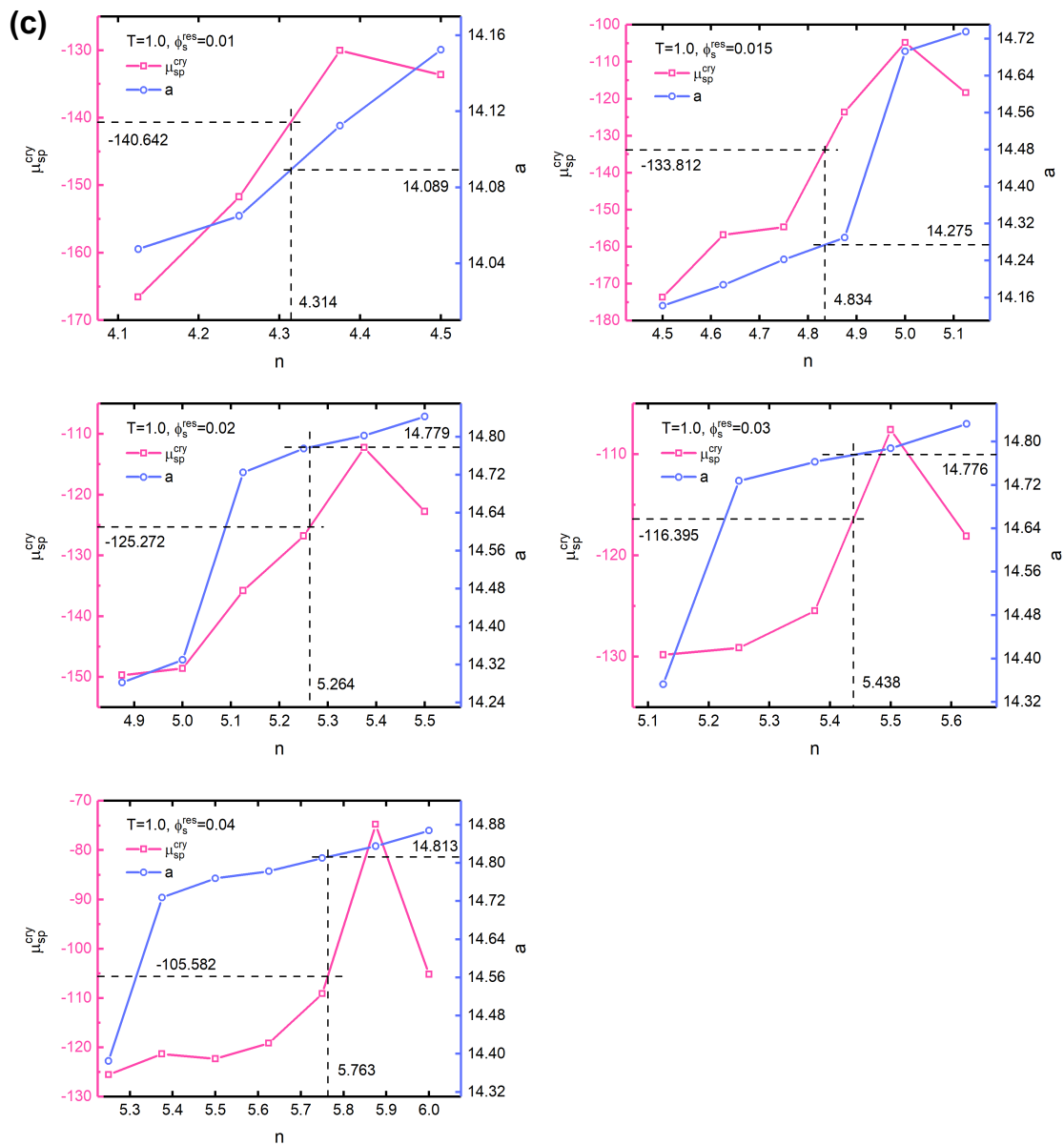
Figure 3.14. The NPT ensemble simulation results for how μ_s^{cry} and a of the colloidal crystals change with the stoichiometry n under different temperatures and reservoir concentrations. (a) T=0.6, (b) T=0.8, and (c) T=1.0.

3.6.6. High-temperature limit in the lattice vibrational term

If we use the high-temperature limit $\beta\hbar\omega \ll 1$ in the calculation of the lattice vibrational free energy, we get

$$
\begin{aligned}
\beta p_{vib} &= \frac{\gamma}{V} \int_0^{\omega_m} \left(\frac{1}{2}\beta\hbar\omega^{1/\gamma} + \frac{\beta\hbar\omega^{1/\gamma}}{e^{\beta\hbar\omega} - 1} \right) \frac{N_c N_{dof}}{\gamma\omega_m^{1/\gamma}} \mathrm{d}\omega \\
&\approx \frac{\gamma N_{dof}}{V_c} \left\{ \frac{\beta\hbar\omega_m}{2(\gamma+1)} + 1 \right\} \\
&\approx \frac{\gamma N_{dof}}{V_c}
\end{aligned}
$$

(3.50)

This gives the classic result that the thermal pressure is inversely proportional to the volume in the high-temperature limit [90], akin to the ideal gas law. However, this relation is not found in our results. Therefore, we believe the high-temperature limit is not reached in our system.

CHAPTER 4

Electric-Field-driven dynamics[*]

4.1. Introduction

In Chapters 2 and 3, we have demonstrated the existence of the superionic state in charged colloidal crystals, exploring the transitions to this state induced by temperature variations and particle concentration in the solution. These findings lay the groundwork for utilizing charged colloidal crystals as superionic materials. Now, our focus shifts to examining the dynamic behavior of colloidal crystals under the influence of an external electric field.

Electric-field-induced phenomena in charged colloidal systems have garnered significant attention due to their fascinating behavior and potential applications in various scientific and technological fields. When an external electric field is applied to a suspension of charged colloidal particles, a range of intriguing phenomena emerge. One such phenomenon is electrophoresis [108], where charged particles undergo directed motion in response to the electric field. Electrophoresis is driven by the electrostatic forces exerted on the particles, causing them to migrate toward the oppositely charged electrode. This phenomenon has been extensively studied and exploited for applications such as particle separation, microfluidics, and drug delivery systems [109].

---

[*]This chapter is primarily based on the published work [107] of Yange Lin and Monica Olvera de la Cruz, **Colloidal superionic conductors**, *PNAS* 120.15 (2023): e2300257120, with modified notations and extended details to comply with the structure of this work.

Another remarkable phenomenon observed in charged colloidal systems under electric fields is lane formation [110, 111, 112, 113]. When subjected to a sufficiently strong electric field, charged particles can self-organize into parallel lanes within the suspension. The formation of lanes is a consequence of the interplay between Coulomb interactions among the particles and the screening effects of the surrounding medium. The phenomenon has been observed in various systems, including colloidal suspensions, liquid crystals, and even biological systems. Lane formation has implications in areas such as pattern formation, particle sorting, and the design of functional materials.

In this study, we investigate the behaviors of a size-asymmetric charged colloidal crystal under an external electric field using molecular dynamics (MD) simulations. The phenomenon of electric-field-induced superionicity has been observed in various materials [114, 115, 116, 117]. Here, we aim to explore similar transitions and other field-driven phenomena within colloidal crystals, such as the formation of lanes through Coulomb interactions, in contrast to the Debye-H"uckel screened interactions typically used in lane formation studies [110, 111, 112, 113]. Furthermore, we conduct an in-depth analysis of charge transport, including ion mobility, resistivity, and the underlying transport mechanisms. Specifically, we quantify the dissipation, which reflects the heating of the system and relates to its thermal stability, as well as the fluctuation of ion currents, which indicates the stability of the output. As the applied electric field strengthens, we observe an increase in dissipation alongside a decrease in the relative fluctuation of currents. To characterize this trade-off relationship, we employ the *thermodynamic uncertainty relation* [118, 119, 120, 121, 122, 123, 124, 125, 126]. By examining these aspects, we gain

valuable insights into the charge transport mechanisms in colloidal superionic conductors and their implications for thermal stability and electrical performance.

4.2. Langevin dynamics

4.2.1. Langevin equations

In previous chapters, we employed Langevin dynamics to numerically implement an implicit solvent treatment, but we have yet to provide an introduction to this method. In this chapter, we continue to utilize Langevin dynamics and the implicit solvent treatment in our simulations. However, it is necessary to review the fundamentals of Langevin dynamics and the expressions for dissipation and work derived from the Langevin equations [127, 111], as these concepts are essential for our subsequent discussions.

When we treat the solvent as implicit, we disregard the degrees of freedom of solvent molecules. Instead, we consider the motions of solvent molecules as unpredictable random collisions with the larger particles explicitly included in the dynamics, often referred to as *Brownian particles*. These collisions are responsible for the *thermal fluctuations* and the stochastic nature of the system's dynamics. Moreover, when a Brownian particle moves in a certain direction, it encounters more collisions from that direction, leading to friction that hampers its movement. This friction, which causes the particle to lose kinetic energy that dissipates as heat into the medium, is known as the *dissipative force*. Mathematically, the dynamics of the system are described by a set of coupled underdamped Langevin equations:

$$(4.1) \qquad\qquad \dot{\boldsymbol{r}}_i = \boldsymbol{v}_i,$$

$$(4.2) \qquad\qquad m_i\dot{\boldsymbol{v}}_i = -\nabla_i U + \boldsymbol{F}_i^{ext} - \gamma_i\boldsymbol{v}_i + \sqrt{2D_i}\boldsymbol{\xi}_i.$$

Here, the dots indicate time derivatives. The first term on the right-hand side, $-\nabla_i U$, represents the interparticle force. The second term, $\boldsymbol{F}_i^{\text{ext}}$, accounts for the external force applied to the system, which in this case is given by $\boldsymbol{F}_i^{\text{ext}} = q_i\boldsymbol{E}$, where $\boldsymbol{E}$ is the applied electric field. The first and second terms correspond to Newton's second law. Following that, the third term on the right-hand side, $-\gamma_i\boldsymbol{v}_i$, denotes the dissipative force, which is directly proportional to the velocity of the particle. The damping coefficient $\gamma_i = 6\pi\eta_0 R_i$ is derived from Stokes' law, with η_0 representing the viscosity of the medium. Finally, the fourth term on the right-hand side, $\boldsymbol{\xi}_i$, represents Gaussian white noise that incorporates thermal fluctuations. It possesses a mean value $\langle\boldsymbol{\xi}_i\rangle = 0$ and a variance $\langle\boldsymbol{\xi}_i(t)\boldsymbol{\xi}_j(t')\rangle = 2D_i\boldsymbol{I}d\delta_{ij}\delta(t - t')$, where $\langle...\rangle$ denotes the ensemble average, D_i is the diffusion coefficient, $\boldsymbol{I}_d$ is the identity matrix in a d-dimensional space, and δ_{ij} is the Kronecker delta function.

4.2.2. Fluctuation-dissipation theorem

In order to sustain the continuous and erratic motion of Brownian particles, there is a relationship between the energy input (gain) from the medium to the particles through thermal fluctuations and the energy output (loss) from the particles to the medium. In the simplest system without external forces or interparticle interactions, such as a single-particle system, the fluctuation and dissipation must be in balance since they arise from

the same source—random collisions with surrounding molecules. This balance between fluctuation and dissipation is governed by the *fluctuation-dissipation theorem* (FDT) [128].

From Eqn. (4.2), the probability distribution function of particle velocity satisfies the Fokker-Planck equation:

$$(4.3) \qquad \frac{\partial P(v,t)}{\partial t} = -\frac{1}{m}\frac{\partial}{\partial v}\left[(-\nabla U + F_{\text{ext}} - \gamma v)P(v,t)\right] + \frac{D}{m^2}\frac{\partial^2}{\partial v^2}P(v,t).$$

In equilibrium or in the steady state, $\partial P/\partial t = 0$. By setting $-\nabla U = 0$ and $\boldsymbol{F}_i^{\text{ext}} = 0$, we solve (4.3) and obtain:

$$(4.4) \qquad P^{\text{ss}}(v) = \frac{1}{\sqrt{2\pi D/(m\gamma)}}\exp\left(-\frac{m\gamma v^2}{2D}\right),$$

where *ss* denotes *steady state*. The stationary velocity distribution must coincide with the Maxwellian distribution:

$$(4.5) \qquad P^{\text{ss}}(v) \propto \exp\left(-\frac{mv^2}{2k_BT}\right),$$

where k_B is the Boltzmann constant. By comparing Eqns. (4.4) and (4.5), we find:

$$(4.6) \qquad D = \gamma k_B T.$$

This relationship is known as the Einstein relation.

Using Eqn. (4.6), the Langevin equation becomes:

$$(4.7) \qquad m_i\dot{\boldsymbol{v}}_i = -\nabla_i U + \boldsymbol{F}_i^{\text{ext}} - \gamma_i\boldsymbol{v}_i + \sqrt{2k_BT\gamma_i}\boldsymbol{\xi}_i.$$

4.2.3. Dissipation, entropy production, and work

The system exchanges energy with the surrounding medium through the friction term $-\gamma \boldsymbol{v}$ and the thermal noise term $\sqrt{2k_B T \gamma}\boldsymbol{\xi}$. The dissipation over a time interval $\mathcal{T}$ is defined as the amount of energy flowing from the system to the reservoir during this time and can be expressed as [127]:

$$(4.8) \qquad \mathcal{Q} = \sum_i \int_{\mathcal{T}} (\gamma_i \boldsymbol{v}_i - \sqrt{2k_B T \gamma_i}\boldsymbol{\xi}_i) \cdot \mathrm{d}\boldsymbol{r}_i.$$

Here, the symbol "·" represents the Stratonovich product. By using equations (4.1) and (4.7), we can write:

$$(4.9) \qquad d\boldsymbol{r}(t) = \boldsymbol{v}(t)\mathrm{d}t + \frac{1}{2m}\left[\boldsymbol{F}(t)(\mathrm{d}t)^2 - \gamma\boldsymbol{v}(t)(\mathrm{d}t)^2 + \sqrt{2k_B T\gamma}\boldsymbol{\xi}(t)\mathrm{d}t\right],$$

where $\boldsymbol{F} = -\nabla U + \boldsymbol{F}^{\text{ext}}$ represents the force acting on a particle. Consequently, the average dissipation is given by:

(4.10)

$$\langle \mathcal{Q} \rangle = \sum_i \int_0^{\mathcal{T}} \langle \mathrm{d}\boldsymbol{r}_i(t) \cdot (\gamma_i \boldsymbol{v}_i(t) - \sqrt{2k_B T \gamma_i}\boldsymbol{\xi}_i(t)) \rangle$$

$$= \sum_i \int_0^{\mathcal{T}} \left\langle \left(\boldsymbol{v}_i(t)\mathrm{d}t + \frac{1}{2m_i}\sqrt{2k_B T\gamma_i}\boldsymbol{\xi}_i(t)\mathrm{d}t + \mathcal{O}((\mathrm{d}t)^2)\right) \cdot (\gamma_i \boldsymbol{v}_i(t) - \sqrt{2k_B T\gamma_i}\boldsymbol{\xi}_i(t)) \right\rangle$$

$$= \sum_i \int_0^{\mathcal{T}} \left(\gamma_i \langle v_i^2 \rangle - dk_B T\gamma_i/m_i\right)\mathrm{d}t,$$

where $\langle \boldsymbol{\xi}^2(t) \rangle = d$ represents the dimensionality of the space. In the third equality of equation (4.10), we have used the fact that the thermal force $\boldsymbol{\xi}$ is independent of other variables and has a mean of zero.

In a steady state, there is no average change in entropy in the system over a long period of time. Therefore, the total entropy production solely comes from the reservoir. Since the reservoir is assumed to be at a constant temperature, the entropy production (EP) is simply given by $\langle \mathcal{Q} \rangle / T$. Consequently, the mean (EP) rate is:

$$\langle \dot{\Sigma} \rangle \equiv \langle \dot{\mathcal{Q}} \rangle / T = \sum_i \left(\gamma_i \langle v_i^2 \rangle / T - d\gamma_i k_B / m_i \right). \tag{4.11}$$

It is worth noting that inside the integral is the difference between the kinetic energy of the particles and their thermal energy. In equilibrium, when there are no external fields, these two quantities should be equal, resulting in zero dissipation and zero entropy production.

When an external field is applied, the motion of the particles is driven and eventually reaches a non-equilibrium steady state (NESS). Since the particles generally gain more kinetic energy when driven, they experience larger frictions that the thermal noise cannot fully cancel out. As a result, the expression in equation (4.10) is no longer zero but positive. Therefore, to maintain the system in NESS, we need to continuously input energy into the system through the external force to compensate for the dissipation. The amount of input energy is given by:

$$\mathcal{U}(\mathcal{T}) = \sum_i \int_{\mathcal{T}} \boldsymbol{F}_i^{\text{ext}} \cdot d\boldsymbol{r}_i. \tag{4.12}$$

Apart from dissipation, the remaining input energy turns into the work used to drive the particles' motion. By using equations (4.8) and (4.12), the work can be written as:

$$(4.13) \qquad \mathcal{W} \equiv \mathcal{U} - \mathcal{Q} = \sum_i \int_{\mathcal{T}} (m_i \dot{\boldsymbol{v}}_i + \nabla_i U) \cdot \mathrm{d}\boldsymbol{r}_i.$$

Here, $m_i \dot{\boldsymbol{v}}_i$ represents the total force on a particle. Thus, the first term in equation (4.13) accounts for the work done by particle displacements, which are actually conducting charges. The second term, $\nabla_i U$, is the internal force with a negative sign, accounting for the energy stored in the structural distortion as a response to the applied field [111].

We have already discussed one limiting case when the external field goes to zero and the system returns to equilibrium, the energy input, the dissipation, and the work are all zero on average. In the other limiting case, as the field increases sufficiently, the interparticle force $-\nabla U$ becomes negligible. In this case, the steady-state velocity is solely determined by the external force, given by $v = F/\gamma$. Substituting this expression for velocity into Eqn. (4.11) and calculating the work rate $\dot{\mathcal{W}} = \dot{\mathcal{U}} - \dot{\mathcal{Q}}$, we find:

$$(4.14) \qquad \dot{\mathcal{W}} = dk_B T \sum_i \gamma_i / m_i.$$

Therefore, the work rate is bounded by the thermal energy. This can be understood as follows: the external field converts non-directional, stochastic thermal energy into useful energy that drives particles in the desired direction. The cost associated with this conversion is dissipation. As the field becomes stronger, the percentage of thermal energy being converted increases, but it can never exceed 100%.

4.3. Methods

All of our MD simulations are done using the LAMMPS software package [69, 94, 95, 96, 97, 98, 129]. Images of simulation results are created using VMD [99].

4.3.1. Simulation setup

We simulate a binary colloidal crystal composed of large charged NPs held on the lattice points together by oppositely-charged small NPs in salt-free conditions. The box contains $4 \times 4 \times 4$ unit cells with periodic boundary conditions, mimicking bulk crystal. Large and small NPs have the radii $R_L = 5\,\text{nm}$ and $R_S = 1\,\text{nm}$, respectively, and a mass ratio $m_L/m_S = 125$. The charges are set to be $q_L = -80\,\text{e}$ and $q_S = +10\,\text{e}$. The small-to-large number ratio is kept at $8:1$ to maintain charge neutrality. NPs interact with each other via hardcore interactions and Coulomb interactions. The initial lattice is arranged in a *fcc* structure but is deformable during the isothermal-isobaric (NPT) ensemble simulations. The external pressure is set to zero [70], hence the cohesion of the crystal comes from the attractions between large and small NPs only. A complete list of simulation parameters can be found in Table 4.1 in the Appendix section of this chapter. The Coulomb potential is calculated by the particle-particle particle-mesh (PPPM) method with a precision of 5×10^{-4}, and the cutoff distance for PPPM ranges from $20\sigma \sim 30\sigma$, depending on the crystal size.

As shown in Figure 4.1, we use $\boldsymbol{a}$, $\boldsymbol{b}$, and $\boldsymbol{c}$ to represent the three primitive vectors of the lattice in the x, y, z-directions, respectively. A uniform electric field $\boldsymbol{E}$ is applied along the x-direction which drives the large and small particles towards opposite directions, whose currents are marked as $\boldsymbol{j}_L$ and $\boldsymbol{j}_S$. The dynamics of the system are described by a set

of coupled underdamped Langevin equations given as Eqns. (4.1) and (4.2). We do not consider the temperature dependence of the medium viscosity as well as the hydrodynamic interactions and hence can treat γ_i as isotropic constants.
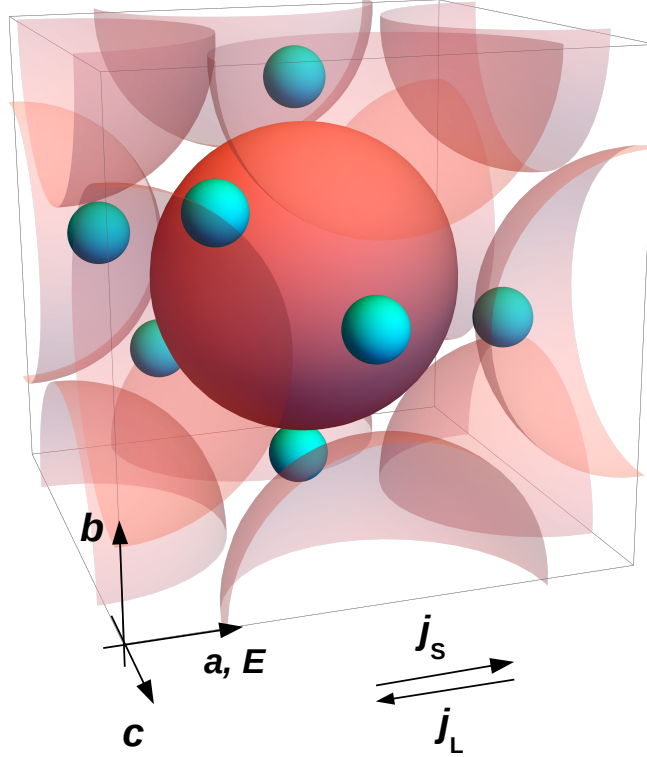
Figure 4.1. Coarse-grained model of a *fcc* unit cell in the binary colloidal superlattice: large NPs in pink and small NPs in cyan. Large NPs on the edge centers are set as partly transparent for better visualization. The primitive vectors $\boldsymbol{a}$, $\boldsymbol{b}$, and $\boldsymbol{c}$ are shown in the lower left. A uniform electric field $\boldsymbol{E}$ is applied along $\boldsymbol{a}$ during the MD simulations. $\boldsymbol{j}_L$ and $\boldsymbol{j}_S$ are the induced currents of large and small NPs.

4.3.2. Equilibration and sampling

The system is prepared by placing large NPs on a $4 \times 4 \times 4$ *fcc* lattice sites with small NPs filled in the lattice voids without strong overlaps. Periodic boundary conditions

are implemented. The crystal is thermalized and pressurized in the isobaric-isoenthalpic (NPH) ensemble using Langevin dynamics, which is equivalent to the isothermal-isobaric (NPT) ensemble but with stochastic thermal noise. The pressure is first set as $260\,\mathrm{kPa}$ to keep the crystal compact for 100τ. In this work, we set $\tau = 2.85 \times 10^{-10}\,\mathrm{s}$. Then, the pressure is gradually reduced to zero in another 200τ. After equilibrating the crystal at zero pressure for 5000τ, an external force $F_i^{ext} = q_i E$ is added to each particle along the x-direction, and the system is further run for 15000τ. The simulation box is set as triclinic and thus is able to deform all the time.

We start sampling 2500τ after the addition of external forces, at which time the system has already reached the NESS (see Figure 4.17 in the Appendix section of this chapter). The displacement of each particle along x-direction in the following 5000τ is measured. The x-velocity v_x, its square v_x^2, and the square of acting force F_i^2 are sampled every 5τ for 2000 times.

4.4. Results and Discussions

4.4.1. Field-induced transitions.

Before applying the electric field, we examine the thermal expansion of the crystal. As shown in Figure 4.2, the increasing temperature can cause an isotropic expansion of the crystal. The expansion is not always continuous, but has a discontinuous jump at $T_c \approx 320K$. It characterizes a first-order transition from the ionic state to the superionic state, as shown in previous chapters, regardless of the presence of electrostatic screening [32, 77].
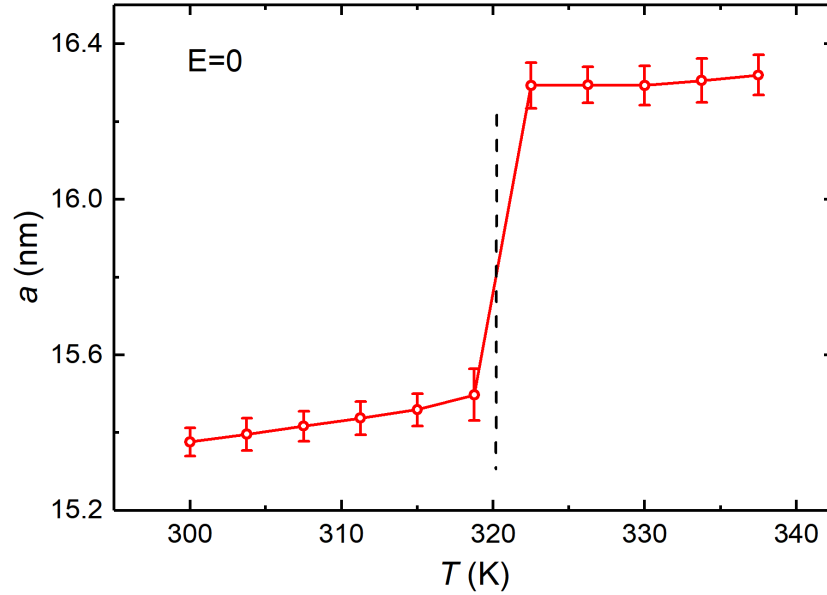
Figure 4.2. The equilibrium lattice constant under different temperatures in the NPT simulations without an electric field. The lattice expands isotropically in three dimensions with the increasing temperature, and an ionic to superionic transition is observed at $T_c \approx 320\,\mathrm{K}$.

Below the transition temperature, the application of an electric field can induce the ionic to superionic transition. Figure 4.3(a) shows that in the NESS and at $T = 300\,\mathrm{K}$, how the lattice constants in three dimensions change with the field intensity. At $E \approx 1\,\mathrm{mV/nm}$, a discontinuous expansion similar to that in Figure 4.3(a) is observed, indicating an ionic to superionic transition. Figure 4.3(b) shows the hysteresis curves of the field-induced ionic to superionic transition. Interestingly, when we prepare the crystal in the superionic state at $E = 2\,\mathrm{mV/nm}$ and gradually decrease the field intensity, the superionic state persists even when E reaches zero. This reflects a pronounced inertial effect of the system, akin to a well-known phenomenon that flowing suppresses the freezing point of water[114]. Nonetheless, the transition is still switchable when we reduce E

at a much slower speed or wait long enough after E reaches zero. Similar field-induced discontinuous crystal expansions and hysteretic behaviors have been observed in atomic insulators [114]. Notably, the crystal remains cubic and isotropic right after the ionic to superionic transition induced by an anisotropic field. It is because the maintenance of a symmetric structure helps to maximize the cohesive energy of the lattice.
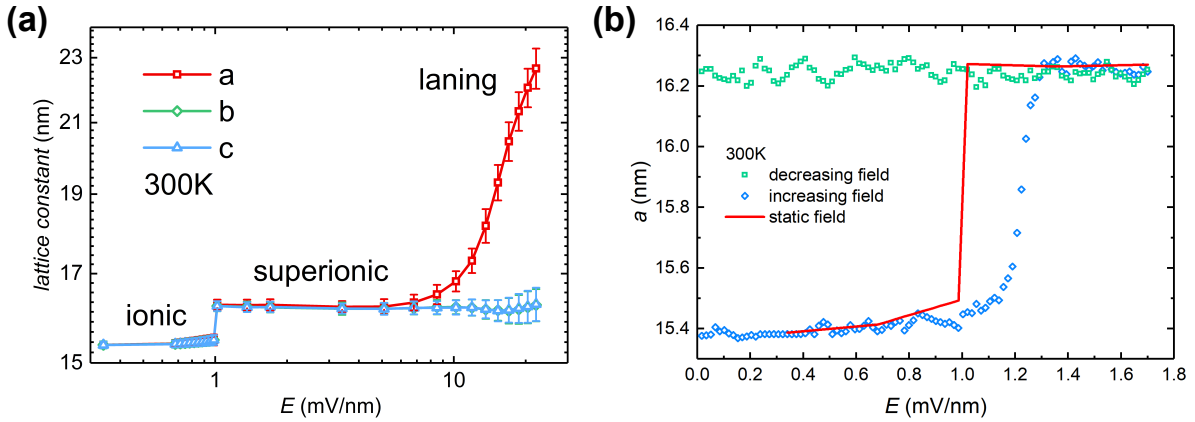
Figure 4.3. Lattice deformations and structural transitions induced by the electric field in the MD simulations. (a) Values of three lattice constants in the NESS under different electric field intensities E at $T = 300$ K. $a = |\boldsymbol{a}|$, $b = |\boldsymbol{b}|$, and $c = |\boldsymbol{c}|$. While the lattice maintains orthogonal in the whole range, it is gradually stretched along the x-direction where the field is applied. (b) The hysteresis curves for the field-induced sublattice melting in the weak field regime, where both increasing and decreasing fields vary in a rate of $\mathrm{d}E/\mathrm{d}t = 1.19 \times 10^6$ V/(nm · s).

This symmetry, however, is broken by further enhancing the field. The lattice deforms from cubic to tetragonal, where it expands along the field direction while remaining unchanged in the other two directions. Meanwhile, small NPs start to move in lanes for faster transport. Similar lane formations have been reported in various charged systems [41, 110, 111, 130, 112], except that our system has no constant volume and it is the attraction between the opposite fluxes that keeps the system finite. Although the lattice

of large NPs still drifts as a whole, the magnitude of the anisotropic stretch increases rapidly with the field strength until the crystal is destroyed. Due to the application of the field, we do not observe any dynamically arrested state throughout our simulations, such as low-density colloidal Wigner glass or electrostatic gels [88].
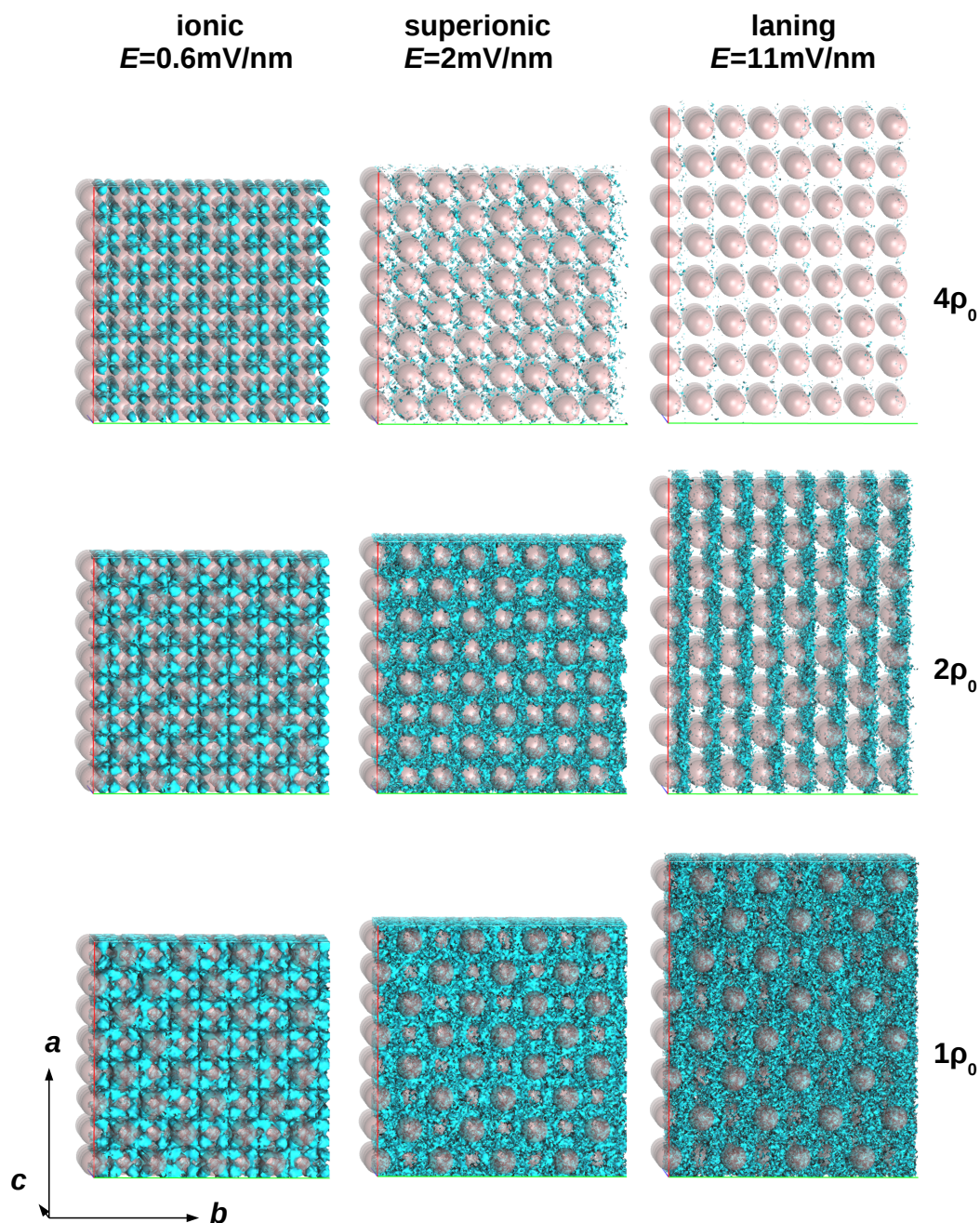
Figure 4.4. Isosurfaces of the probability densities of small NPs at different isovalues. The isosurfaces at $2\rho_0$ and $4\rho_0$ present the regimes where the density of small NPs is no less than $2\rho_0$ and $4\rho_0$, respectively, where ρ_0 is the mean density of small NPs. The plotting is three-dimensional. The lattice is placed almost parallel to the xz-plane because it is the best angle to visualize and compare the patterns of small NPs.

In the "ionic-superionic-laning" transitions, the distribution of small NPs inside the lattice (strictly speaking, the free space inside the lattice) goes from inhomogeneous, to homogeneous, and back to inhomogeneous. Figure 4.4 shows isosurfaces of the probability densities [14] of small NPs at increasing isovalues $1\rho_0$, $2\rho_0$, and $4\rho_0$, where $\rho_0 \equiv N_S/V_c$ is the mean density of small NPs in each structure. Here, $N_S = 8$ is the number of small NPs in one unit cell and V_c is the volume of a unit cell. We evaluate $V_c = abc$ since the lattice remains orthogonal, where a, b, and c are the lattice constants in x, y, and z-directions, respectively. In the ionic state, small NPs are highly populated at the interstitial sites of the lattice, which are the $32f$ Wyckoff positions [71]. In contrast, the superionic state has a uniform small NP distribution and very few high-density regimes. The laning state differs from the previous two in that, on one hand, the free space is ergodic for small NPs, as seen in the $1\rho_0$ isosurface, and on the other hand, small NPs are not uniformly distributed, as seen in the $2\rho_0$ isosurface.

To quantify the homogeneity of the distribution of small NPs, we measure their translational entropy, which is a physical quantity widely used in characterizing structural transitions [131, 132, 133, 134, 135], defined as [136, 137]

$$(4.15) \qquad S_{tran}/k_B = -2\pi\rho_0 \int_0^\infty [g(r)\ln g(r) - g(r) + 1]r^2 \mathrm{d}r.$$

Here, $g(r)$ is the radial distribution function between small and small NPs (see Figure 4.18 in the Appendix section of this chapter). $S_{tran} = 0$ means an utterly even distribution in the crystal including the hard-cores of large NPs. The change in S_{tran} (Figure 4.5) captures the transitions between states. The ionic to superionic transition is indicated by

a dramatic increase in S_{tran}, since in the superionic state there are more accessible translational degrees of freedom (DOF) for small NPs. Afterward, S_{tran} first slowly rises up and then drops with enhancing field intensity. This turning point signals lane formation, as small NPs start to lose their translational DOF in y and z directions.
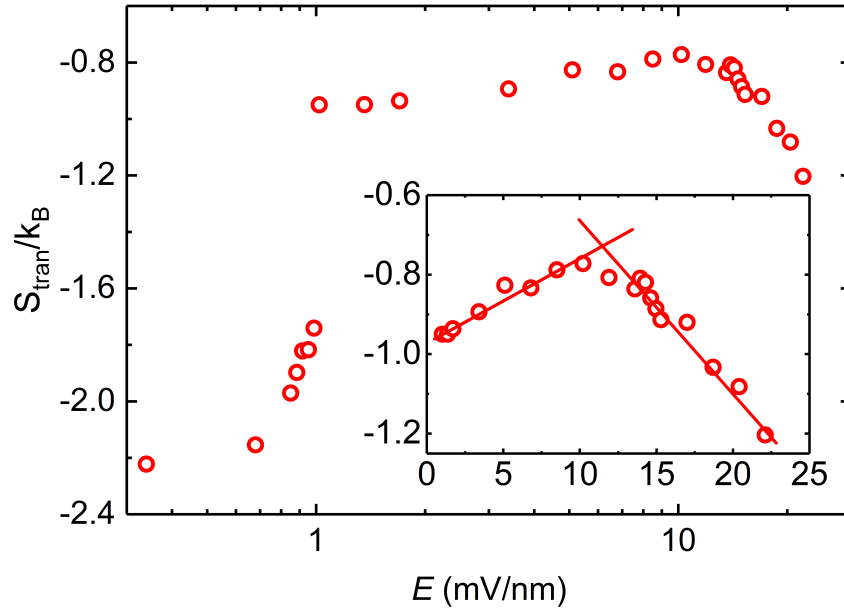
Figure 4.5. The change of translational entropy of small NPs in the NESS with the field intensity. (Inset) A zoom-in view of the turning point.

4.4.2. Conductive behavior.

The dynamic properties can be described by the mobilities of particles calculated as $\mu = \langle v \rangle / E$, where $\langle v \rangle$ is the mean drift velocity in the NESS. As seen in Figure 4.6, the mobilities of large and small NPs both grow monotonically with the field intensity and exhibit a sharp increase when the superionic transition occurs. Sodium ions Na^+, as a reference, have a mobility of $5 \times 10^{-8}\,\mathrm{m^2 s^{-1} V^{-1}}$ in water [138].The validity of the relation

$\mu_i \propto F^{ext}/(\gamma E) \propto q_i/R_i$ is examined in the inset graph and is proved by the fact that the

ratio $\alpha = (\mu_L R_L q_S)/(\mu_S R_S q_L)$ goes to 1 after the system enters the superionic state.
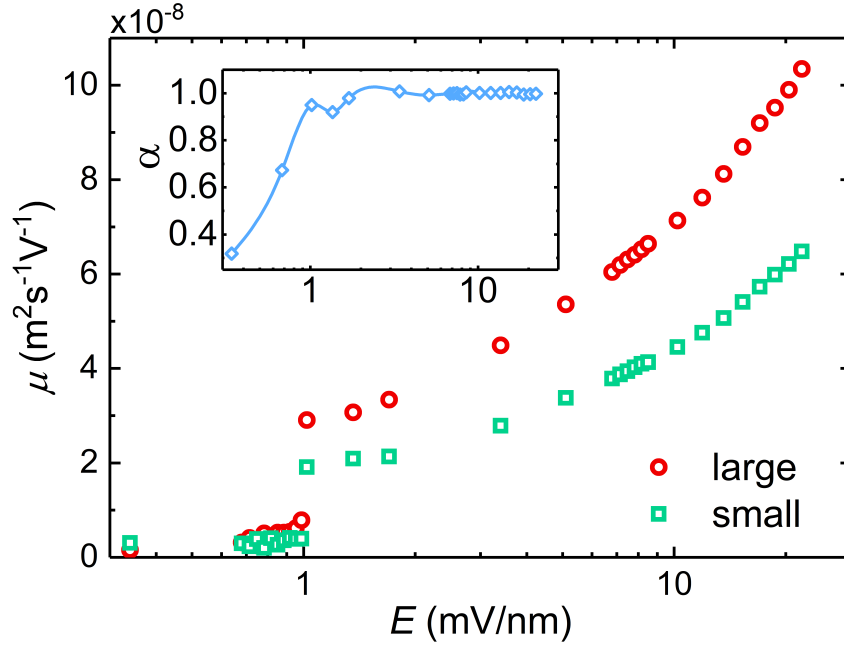
Figure 4.6. The mobilities of large and small NPs under different field intensities at $T = 300\,\mathrm{K}$. (Inset) The ratio $\alpha = (\mu_L R_L q_S)/(\mu_S R_S q_L)$ at different E.

To quantify the field intensity dependency of $\langle v \rangle$, we consider a one-dimensional trans-

port model. Similar models have been used to classically describe electron conduction in

periodic systems such as conjugate π bond systems [139]. As the crystal approaches

the laning state, linear transport channels parallel to the field direction (x-direction) are

formed. When a small NP moves in these transport channels, it encounters periodic

steric repulsions from large NPs (Figure 4.7(a)), which become the energy barriers in its

diffusion. The height of the energy barrier, ΔU, depends on the minimal distance, $r_{\min}$,

between the small NP and the large NP (Figure 4.7(b)). Since the lattice constants along

y and z-directions in the superionic and laning states are field independent (16.2 nm, see Figure 4.3(a)), we consider $r_{\min}$ to be a constant and obtain $\Delta U = 1.386 \times 10^{-20}$ J via the WCA potential used in our simulations. The original symmetric diffusion energy landscape is tilted by the applied electric field, as shown in Figure 4.7(c). The width of the energy barrier, d, can be physically understood as the distance in the x-direction over which the steric repulsion occurs. Consequently, the energy barriers for forward and backward fluxes become $\Delta U - qEd/2$ and $\Delta U + qEd/2$, respectively. Therefore, using Arrhenius's law we have

(4.16)
$$\langle v \rangle \propto e^{-(\Delta U - qEd/2)/k_B T} - e^{-(\Delta U + qEd/2)/k_B T}.$$
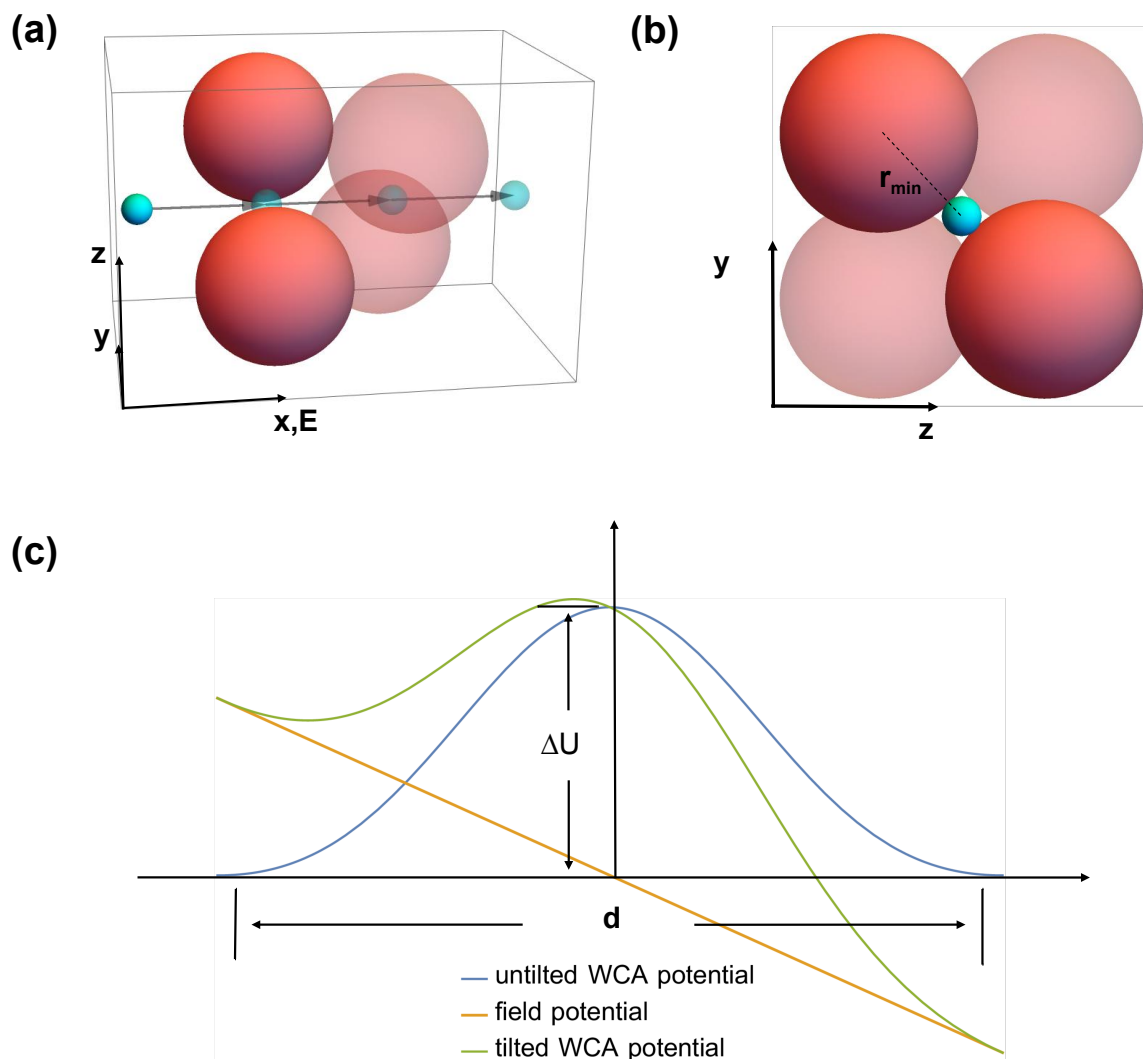
Figure 4.7. (a) A schematic model showing that a small NP (cyan) moves in a linear diffusion channel parallel to the x-direction. Transparent cyan spheres mark the positions where the steric repulsion between the small NP and large NPs (pink) maximizes. (b) The side view (yz-plane) of the model showing that the height of the energy barriers is determined by the minimal distance between the small NP and large NPs and thus can be evaluated by the lattice constant in the y or z-direction. (c) The potential energy landscape for the drift of small NPs under an external field.

We fit (4.16) to the relative drift velocity, $\langle v \rangle = \langle v_S \rangle - \langle v_L \rangle$, under different field strengths obtained in the simulations, with ΔU fixed at 1.386×10^{-20} J (Figure 4.8(a)). The agreement validates the model, despite its simplicity. From (4.16) we have $\mathrm{d}\langle v \rangle / \mathrm{d}T > 0$ when $(\Delta U - qEd/2)/T > 1$ and vice versa (see Section 4.6.1 in the Appendix section of this chapter). Thus, the field enhancement should gradually change $\mathrm{d}\langle v \rangle / \mathrm{d}T$ from positive to negative. This prediction is verified by the resistivity of the system. The resistivity is defined as $\rho = E/\langle j \rangle$, where the charge current is given as

$$(4.17) \qquad\qquad j = \sum_i q_i v_i.$$

Thus, on average $\langle j \rangle = N_S q_S \langle v \rangle$. In Figure 4.8(b) we plot the resistivity as a function of E at $T = 300$ K and $T = 338$ K, with analytical curves calculated via the fitted (4.16). Both simulation and analytical results show a trend that the crystal has a lower resistivity at a higher T, but the dependence on T weakens as the field gets stronger. It can be physically understood that [140] in the weak field regime, thermal agitation effectively helps small NPs overcome activation energy barriers, resulting in a resistivity reduction. However, in the strong field regime, the external force is sufficiently large to drive small NPs through energy barriers. Hence, the current enhancement brought by thermal agitation becomes negligible. Instead, thermal agitation impedes the current as stronger lattice vibration scatters the directional motion of small NPs, akin to electron-phonon interactions in metals.
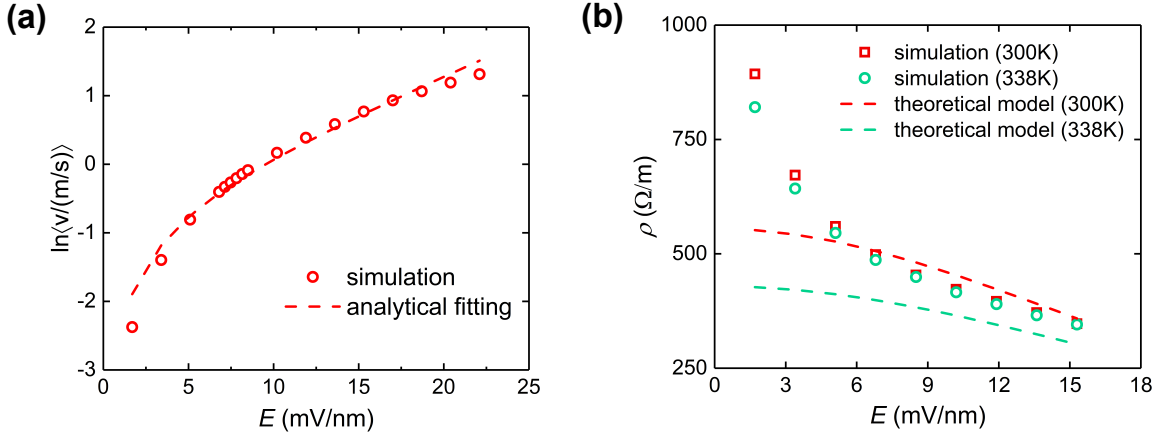
Figure 4.8. (a) The natural logarithm of the relative drift velocity, $\ln\langle v \rangle$, under different field strengths. The circles are the numerical data. The dashed line is the best analytical fitting of (4.16) with fixed $\Delta U = 1.386 \times 10^{-20}$ J, which gives $d = 1.2\,\text{nm}$ and a prefactor 3.32. (b) The resistivity of the system at different E at $T = 300\,\text{K}$ and $T = 338\,\text{K}$. The circles are the numerical data while the dashed lines are the analytical results calculated by the fitted (4.16).

4.4.3. Dissipation and energy conversion efficiency.

It is of significant interest to study the dissipation of a field-driven system. As energy flows into the system via the field, part of it is converted to work and the rest is dissipated into the reservoir due to friction. Thus, via dissipation, we can calculate the *energy conversion efficiency*, known as the ratio of work done and the total input energy. For superionic conductors, dissipation is the heat released during operation and hence affects their safety and thermal stability.

In Section 4.2.3, we have discussed the energy input, the dissipation, and the work. The energy input possesses the expression

$$(4.18) \qquad \mathcal{U}(\mathcal{T}) = \sum_i \int_{\mathcal{T}} \boldsymbol{F}_i^{ext} \mathrm{d}\boldsymbol{r}_i = \sum_i \int_{\mathcal{T}} F_i^{ext} \mathrm{d}x_i,$$

and the dissipation is defined as

$$(4.19) \qquad \mathcal{Q} = \sum_i \int_{\mathcal{T}} (\gamma_i v_{i,x} - \sqrt{2k_B T \gamma_i} \xi_{i,x}) \cdot \mathrm{d}x_i,$$

or in the ensemble average

$$(4.20) \qquad \langle \mathcal{Q} \rangle = \sum_i \int_{\mathcal{T}} (\gamma_i \langle v_{i,x}^2 \rangle - \gamma_i k_B T / m_i) \mathrm{d}t.$$

Combining (4.2), (4.18), and (4.19), the work done to the system by the field is expressed as

$$(4.21) \qquad \mathcal{W} \equiv \mathcal{U} - \mathcal{Q} = \sum_i \int_{\mathcal{T}} (m_i \dot{\boldsymbol{v}}_i + \nabla_i U) \cdot \mathrm{d}\boldsymbol{r}_i.$$

From (4.18) and (4.20), the average rates of energy input and dissipation are given as

$$(4.22) \qquad \langle \dot{\mathcal{U}} \rangle = \sum_i F_i^{ext} \langle v_{i,x} \rangle,$$

$$(4.23) \qquad \langle \dot{\mathcal{Q}} \rangle = \sum_i (\gamma_i \langle v_{i,x}^2 \rangle - \gamma_i k_B T / m_i),$$

respectively.
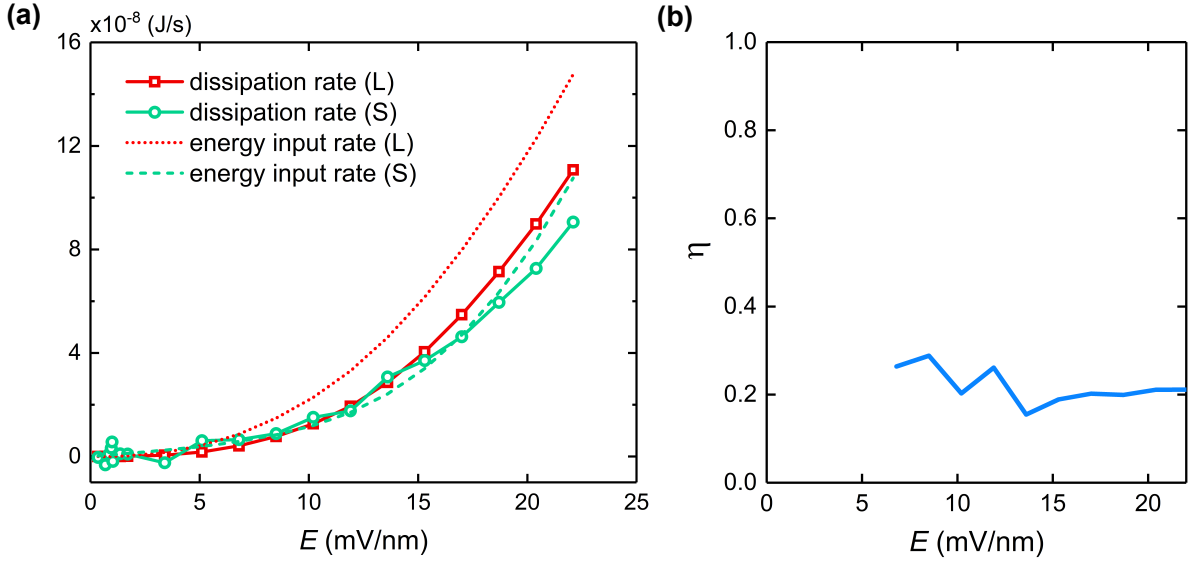
Figure 4.9. (a) Rates of dissipation and energy input of the 256 large NPs and 2048 small NPs in our simulation system, respectively, as a function of E. The work rate can be inferred from the discrepancy between two corresponding curves. (b) Energy conversion efficiency of the system η as a function of E.

Figure 4.9(a) presents $\langle \dot{\mathcal{U}} \rangle$ and $\langle \dot{\mathcal{Q}} \rangle$ in the NESS of large and small NPs in our system. While large NPs are stably converting the input energy into work at a certain rate, small NPs are much more random and less efficient, since the thermal noise has a pronounced effect on smaller particles. Such randomness creates a significant statistical error in our sampling of $v_{S,x}^2$. Therefore, in Figure 4.9(b), we plot the energy conversion efficiency, $\eta \equiv \langle \mathcal{W} \rangle / \langle \dot{\mathcal{U}} \rangle = 1 - \langle \dot{\mathcal{Q}} \rangle / \langle \dot{\mathcal{U}} \rangle$, only at the values when the electric field is strong enough to overcome the thermal fluctuations. With the errors reduced by enhancing the field, η stabilizes at around 0.2 in the strong field regime, showing that our system is highly dissipative.

4.4.4. Thermodynamic uncertainty relation (TUR) and transport efficiency

The stochastic nature of the dynamics of small NPs is also reflected by their less precise current, compared to that of the large NPs (Figure 4.10. The current precision is defined as $\text{var}(j)/\langle j \rangle^2$ and $\text{var}(j) = \langle j^2 \rangle - \langle j \rangle^2$. Notably, currents become more precise in stronger fields, as $\text{var}(j)$ is governed by temperature and $\langle j \rangle$ is governed by the field. Yet, this comes with a cost of larger dissipation as seen in Figure 4.9(a). The trade-off between dissipation and current precision can be described by the TUR recently discovered in far-from-equilibrium statistical mechanics [118, 119, 120, 121, 122, 123, 124, 125, 126]. For Markovian systems such as systems driven by overdamped Langevin dynamics, the TUR states that the current precision is lower-bounded by the inverse of entropy production $\Sigma = \mathcal{Q}/T$ as [118, 119, 120, 121, 122, 123]

$$(4.24) \qquad \frac{\text{var}(j)}{\langle j \rangle^2} \geq \frac{2k_B}{\langle \dot{\Sigma} \rangle}.$$
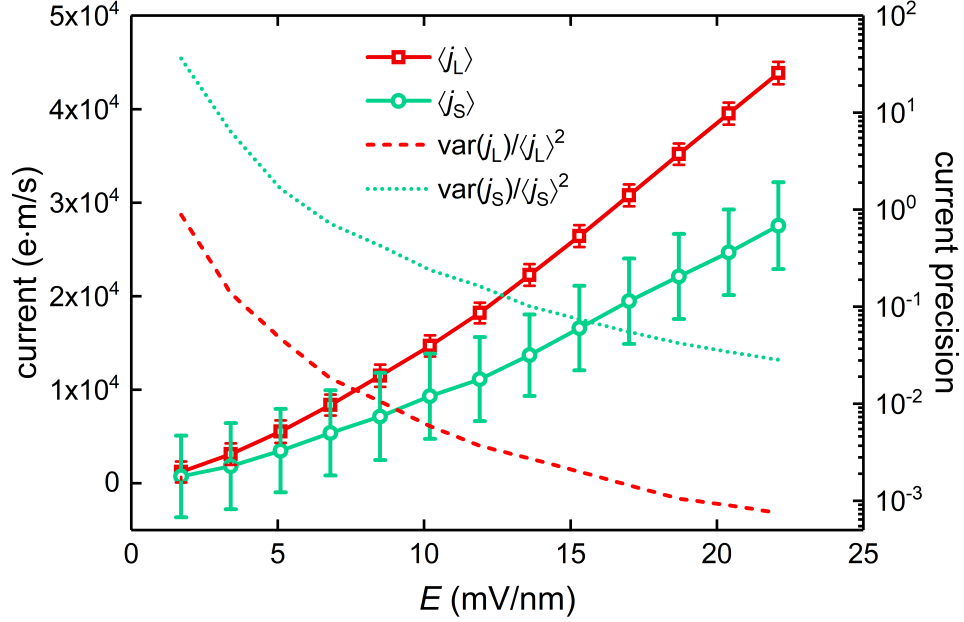
Figure 4.10. Currents of large and small NPs as well as their precision as a function of E.

In systems governed by underdamped Langevin dynamics, such as our system, particles are more diffusive. Hence, a smaller bound is derived as [124, 125, 126]

$$(4.25) \qquad \frac{\mathrm{var}(j)}{\langle j \rangle^2} \geq \frac{2}{4\langle \Upsilon \rangle + 9\langle \dot{\Sigma} \rangle/k_B}.$$

Υ is the so-called *dynamical activity*, defined as

$$(4.26) \qquad \langle \Upsilon \rangle = \sum_i \left(\frac{\langle F_{i,x}^2 \rangle}{k_B T \gamma_i} - 3\frac{\gamma_i \langle v_{i,x}^2 \rangle}{k_B T} + 4\frac{\gamma_i}{m_i} \right)$$

where $F_i = -\nabla_i U + F_i^{ext}$ is the total acting force of particle i. While Σ quantifies the time-irreversibility of currents, Υ quantifies their time-reversibility [124, 125, 126] and measures the tendency of non-directional symmetric movement of particles [125]. In other words, Υ

quantifies the magnitude of thermal motion. As expected, small NPs have a much greater dynamical activity than large NPs (Figure 4.11).
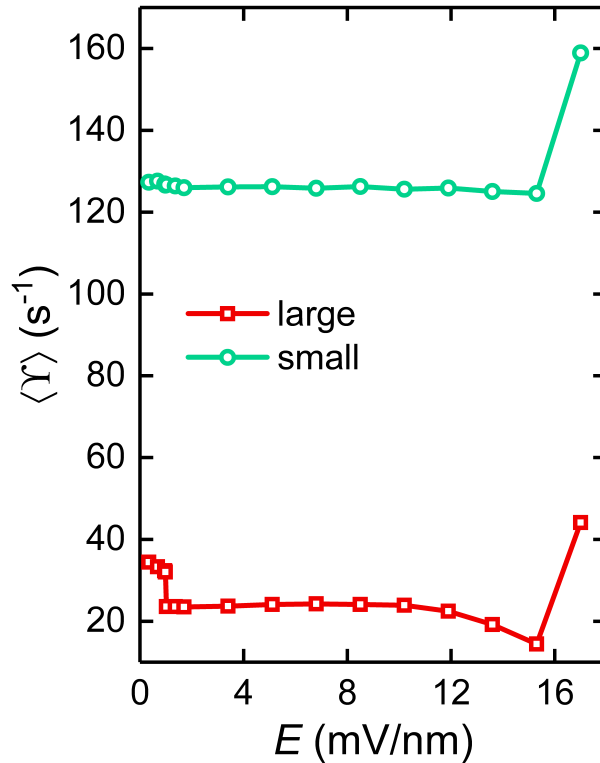
Figure 4.11. Per-particle dynamical activity, $\langle \Upsilon \rangle$. The abnormal increase in $\langle \Upsilon \rangle$ at large E is attributed to simulation errors, where particles start to strongly overlap and some tremendous values of F_i are sampled. To reduce these errors, a smaller simulation timestep should be used (see Figure 4.19 in the Appendix section of this chapter for details).

These reported TURs are valid only in small or ideal systems. In real biochemical systems, the current fluctuations are usually several orders of magnitude larger than the theoretical bounds [141]. How to improve the bounds in the theoretical calculations to more accurately describe real systems is still under exploration. Here, we derive a more precise estimate of the relationship between the entropy production rate and the current precision, using the fact that both can be written in terms of velocity statistics. As the

thermal noise is the only source of stochasticity in the dynamics and its significance has been shown in previous results, we approximate $\text{var}(v) = \sqrt{k_B T/m}$. Thus, via (4.23) the EP rate becomes

$$(4.27) \qquad \langle \dot{\Sigma} \rangle = \frac{N\gamma}{T}[\langle v^2 \rangle - \text{var}(v)] = \frac{N\gamma \langle v \rangle^2}{T},$$

and via (4.17) the current precision becomes

$$(4.28) \qquad \frac{\text{var}(j)}{\langle j \rangle^2} = \frac{\text{var}(v)}{N\langle v \rangle^2},$$

and consequently,

$$(4.29) \qquad \frac{\text{var}(j)}{\langle j \rangle^2} \langle \dot{\Sigma} \rangle = \frac{\text{var}(v)}{\langle v \rangle^2} \frac{\gamma \langle v \rangle^2}{T} = \frac{\gamma k_B}{m}.$$

Compared to (4.24), (4.29) replaces the constant 2 by the ratio of the damping strength and the inertia, γ/m. More details of the derivation and more discussions are in Section 4.6.3 in the Appendix section of this chapter.

Figure 4.12 shows the comparisons among the current precision obtained by simulations, the overdamped [118, 119, 120, 121, 122, 123] and underdamped [124, 125, 126] TUR bounds from the literature ((4.24) and (4.25), respectively), and the bound we obtained in (4.29) for both the large and the small particles. In our system, we set $\gamma_L/m_L = 5$ and $\gamma_S/m_S = 125$. Thus, the bounds given by (4.29) are larger than the overdamped TUR (and the underdamped TUR). Nevertheless, our derived (4.29) still nicely bound the current precision, suggesting that it is important to include system parameters to obtain accurate bound values.
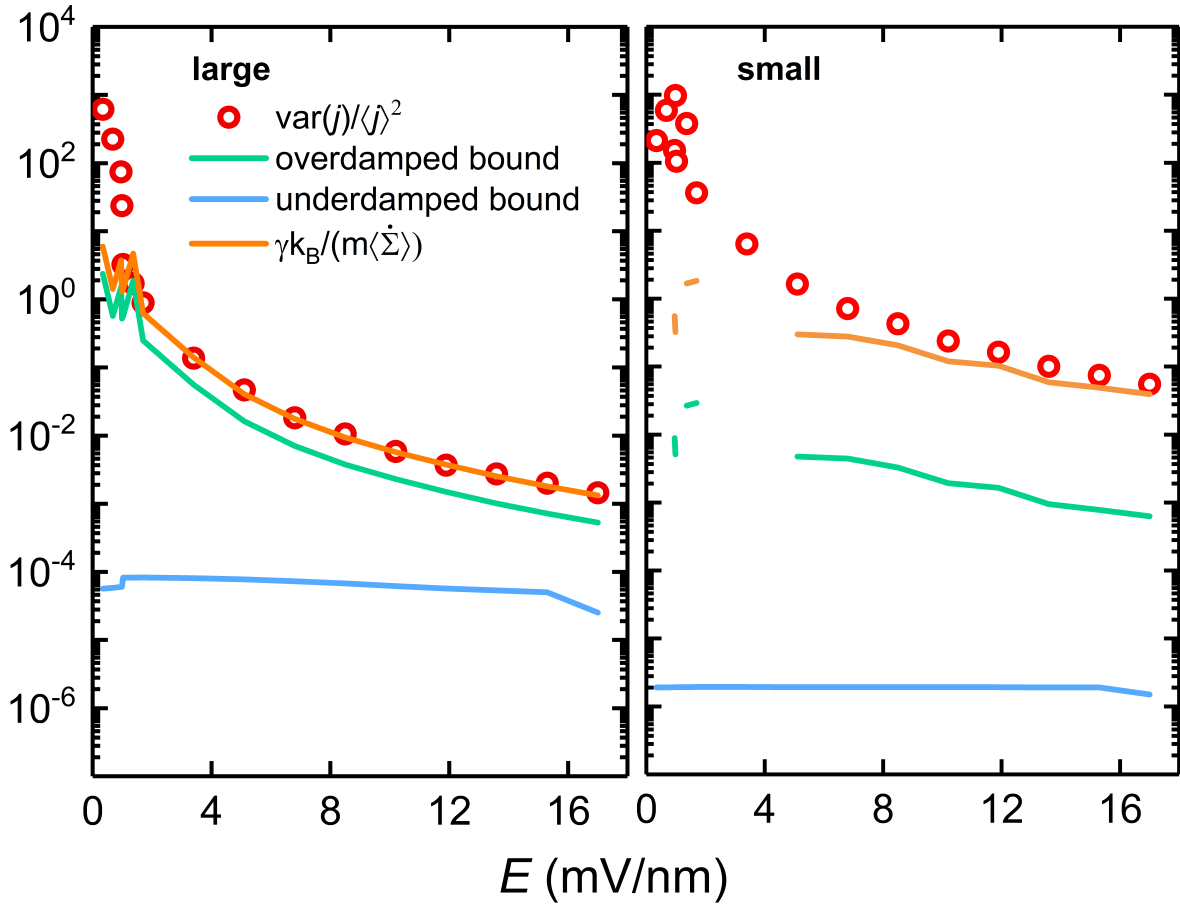
Figure 4.12. Comparison of the current precision, the overdamped bound ((4.24)), the underdamped bound ((4.25)), and the bound given by (4.29) for large and small NP currents, respectively. The discontinuity in curves of the overdamped bound and the bound given by (4.29) for small NP currents is because some data points are negative due to statistical errors and are out of the range of the plot.

Finally, in Figure 4.13 we examine the *transport efficiency*, which measures how close the current precision is to its optimal value, defined as [142] $\chi = bound/precision$. It is seen that large NPs have higher efficiencies in producing a precise current than small NPs, and all χ increase with E but saturate in the laning phase. One may conclude that the

more deterministic (or directed) the dynamics are, the more efficient the transport is until it reaches its limiting value when the system transitions to the laning state. Although the realization of the laning state requires strong electric fields which risks the melting of the large NP crystal, it is tempting to claim that the laning state is a better conductive state in terms of higher diffusion coefficients, lower resistivity, stable energy conversion, and more precise output currents than the superionic state.
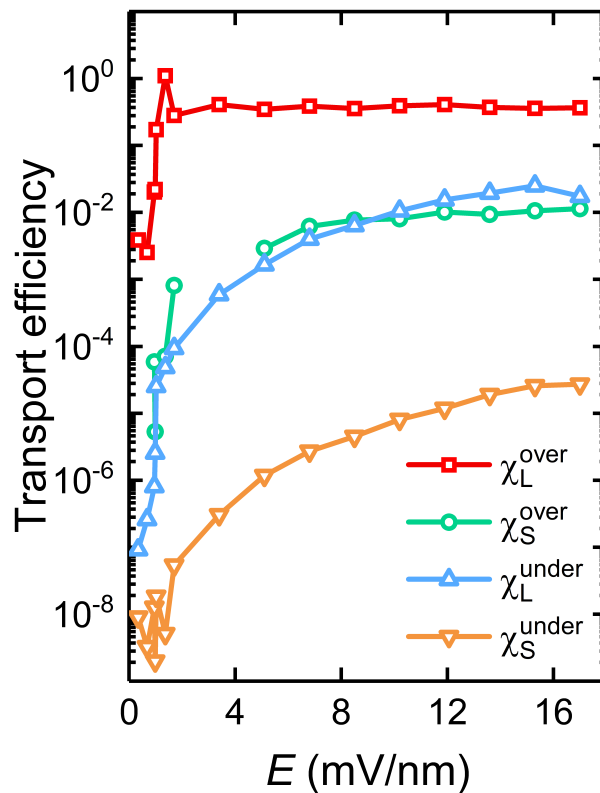
Figure 4.13. Transport efficiency of large and small NP currents as functions of E.

4.5. Conclusion

A size-asymmetric binary charged colloidal crystal in response to an applied electric field undergoes a sharp ionic to superionic transition with a dramatic improvement in

conductive performance, followed by a smoother transition to the laning state where the crystal deforms from cubic to tetragonal. In the laning state, the drift velocity returns to an Arrhenius law exponential relation with the field intensity, and the transport efficiency reaches the maximum. These findings suggest the possible existence of switchable field-induced-superionicity in charged colloidal crystals and widen our knowledge of charge transport mechanisms in solid-state systems.

4.6. Appendix for Chapter 4

4.6.1. Temperature dependence of the drift velocity

The temperature dependence of the drift velocity, via Eqn. (4) in the main text, is given as

$$
(4.30) \qquad \frac{\mathrm{d}\langle v \rangle}{\mathrm{d}T} = \frac{1}{T}\left[f\left(\frac{\Delta U - qEd/2}{T}\right) - f\left(\frac{\Delta U + qEd/2}{T}\right)\right],
$$

where $f(x) = xe^{-x}$ and is plotted as
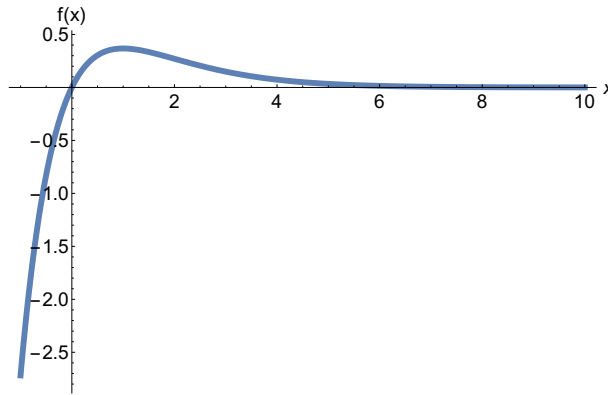
Figure 4.14. The plot of $f(x)$ versus x, which maximizes at $x = 1$.

It is seen that xe^{-x} monotonically increases before $x = 1$ and monotonically decreases afterwards. Hence, when $(\Delta U - qEd/2)/T > 1$, $\mathrm{d}\langle v \rangle/\mathrm{d}T > 0$. When $(\Delta U + qEd/2)/T < 1$, $\mathrm{d}\langle v \rangle/\mathrm{d}T < 0$. When $(\Delta U - qEd/2)/T < 1$ and $(\Delta U + qEd/2)/T > 1$, it is likely to have $\mathrm{d}\langle v \rangle/\mathrm{d}T < 0$ due to the asymmetric shape of $f(x)$. Therefore, in the main text, $(\Delta U - qEd/2)/T > 1$ is used as an approximate condition for $\mathrm{d}\langle v \rangle/\mathrm{d}T > 0$.

4.6.2. Dynamical activity and thermodynamic uncertainty relation

For simplicity, we consider a one-dimensional system, although generalization of these calculations to multiple dimensions is easy. In stochastic dynamics, the probability of observing a trajectory $\boldsymbol{\Gamma}_{\mathcal{T}} = \{\boldsymbol{x}(t), \boldsymbol{v}(t)\}$ from a starting point $(\boldsymbol{x}(0), \boldsymbol{v}(0))$ in the phase space satisfies [124, 125, 126]

$$(4.31) \qquad \mathbb{P}(\boldsymbol{\Gamma}_{\mathcal{T}}) \propto \exp(-\mathcal{A}[\boldsymbol{\Gamma}_{\mathcal{T}}]),$$

where $\mathcal{A}[\boldsymbol{\Gamma}_{\mathcal{T}}]$ is an Onsager-Machlup action functional and expressed as

$$(4.32) \qquad \mathcal{A}[\boldsymbol{\Gamma}_{\mathcal{T}}] = \sum_i \int_0^{\mathcal{T}} dt \left[\frac{1}{4k_B T \gamma_i} (m_i \dot{v}_i(t) + \gamma_i v_i(t) - F_i(t))^2 - \frac{\gamma_i}{2m_i} \right].$$

For the time-reversed trajectory $\bar{\boldsymbol{\Gamma}}_{\mathcal{T}} = \{\bar{\boldsymbol{x}}(t), \bar{\boldsymbol{v}}(t)\} = \{\boldsymbol{x}(\mathcal{T} - t), -\boldsymbol{v}(\mathcal{T} - t)\}$, the action functional becomes

$$
\begin{aligned}
\mathcal{A}[\bar{\boldsymbol{\Gamma}}_{\mathcal{T}}] &= \sum_i \int_0^{\mathcal{T}} dt \left[\frac{1}{4k_B T \gamma_i} (m_i \dot{\bar{v}}_i(t) + \gamma_i \bar{v}_i(t) - \bar{F}_i(t))^2 - \frac{\gamma_i}{2m_i} \right] \\
(4.33) \qquad &= \sum_i \int_0^{\mathcal{T}} dt \left[\frac{1}{4k_B T \gamma_i} (m_i \dot{v}_i(\mathcal{T} - t) - \gamma_i v_i(\mathcal{T} - t) - F_i(\mathcal{T} - t))^2 - \frac{\gamma_i}{2m_i} \right] \\
&= \sum_i \int_0^{\mathcal{T}} dt \left[\frac{1}{4k_B T \gamma_i} (m_i \dot{v}_i(t) - \gamma_i v_i(t) - F_i(t))^2 - \frac{\gamma_i}{2m_i} \right].
\end{aligned}
$$

The *dynamical activity*, Υ, and entropy production rate, $\dot{\Sigma}$, respectively, characterize the time-symmetric and time-antisymmetric components of the action functional (more strictly, the action minus its functional measure [143], $\mathcal{A}[\boldsymbol{\Gamma}_{\mathcal{T}}] - \sum_i \int_{\mathcal{T}} dt \frac{m_i^2 \dot{v}_i(t)^2}{4k_B T \gamma_i}$), which

is to say

$$(4.34) \qquad \mathcal{A}[\mathbf{\Gamma}_\mathcal{T}] - \sum_i \int_0^\mathcal{T} \mathrm{d}t \frac{m_i^2 \dot{v}_i(t)^2}{4k_B T \gamma_i} = -\mathcal{T}(\Upsilon[\mathbf{\Gamma}_\mathcal{T}]/4 + \dot{\Sigma}[\mathbf{\Gamma}_\mathcal{T}]/(2k_B)),$$

$$(4.35)$$
$$\mathcal{A}[\bar{\mathbf{\Gamma}}_\mathcal{T}] - \sum_i \int_0^\mathcal{T} \mathrm{d}t \frac{m_i^2 \dot{\bar{v}}_i(t)^2}{4k_B T \gamma_i} = -\mathcal{T}(\Upsilon[\bar{\mathbf{\Gamma}}_\mathcal{T}]/4 + \dot{\Sigma}[\bar{\mathbf{\Gamma}}_\mathcal{T}]/2) = -\mathcal{T}(\Upsilon[\mathbf{\Gamma}_\mathcal{T}]/4 - \dot{\Sigma}[\mathbf{\Gamma}_\mathcal{T}]/(2k_B)).$$

Hence, we have

$$(4.36) \qquad \langle \Upsilon \rangle = \sum_i \left[\frac{4\gamma_i}{m_i} + \frac{1}{k_B T \gamma_i} \left(2m_i \langle F_i \dot{v}_i \rangle - \langle F_i^2 \rangle - \gamma_i^2 \langle v_i^2 \rangle \right) \right].$$

Multiplying (4.2) by F_i on each side and taking the ensemble average gives

$$(4.37) \qquad m_i \langle F_i \dot{v}_i \rangle = \langle F_i^2 \rangle - \gamma_i \langle F_i v_i \rangle.$$

Multiplying (4.2) by v_i on each side and taking the ensemble average gives

$$(4.38) \qquad m_i \langle v_i \dot{v}_i \rangle = \langle F_i v_i \rangle - \gamma_i \langle v_i^2 \rangle.$$

Note that in the NESS, the average kinetic energy of the system should be invariant with time, $\mathrm{d} \sum_i m_i \langle v_i^2 \rangle / \mathrm{d}t = 0$, rendering $\sum_i m_i \langle v_i \dot{v}_i \rangle = 0$. Therefore (4.36) becomes

$$(4.39) \qquad \langle \Upsilon \rangle = \sum_i \left(\frac{\langle F_i^2 \rangle}{k_B T \gamma_i} - 3 \frac{\gamma_i \langle v_i^2 \rangle}{k_B T} + 4 \frac{\gamma_i}{m_i} \right).$$

The entropy production and dynamical activity together set the lower bound for the precision of current precision, termed *thermodynamic uncertainty relation*, in a form as

[124, 126]

$$(4.40) \qquad \frac{\mathrm{var}(j)}{\langle j \rangle^2} \geq \frac{2}{4\langle \Upsilon \rangle + 9\langle \dot{\Sigma} \rangle / k_B}.$$

Note that here and in the main text, we do not include $\mathcal{T}$ in the denominator on the right-hand side of the TUR equations as in the original work [124, 126]. This is because we use the instantaneous current $j = \sum_i q_i v_i$ whose mean and variance do not grow with time. However, in the original work [124, 126], the integrated current $J_{\mathcal{T}} = \int_{\mathcal{T}} j(t)\mathrm{d}t = \sum_i q_i \Delta x_i(\mathcal{T})$ is used. Thus, $\langle J_{\mathcal{T}} \rangle^2 = \mathcal{T}^2 \langle j \rangle^2 \propto \mathcal{T}^2$ and $\mathrm{var}(J_{\mathcal{T}}) = \mathcal{T}\mathrm{var}(j) \propto \mathcal{T}$. Thus, the denominator on the right-hand side of (4.40) needs to be multiplied by $\mathcal{T}$ to represent the integrated value. A thorough discussion of j and $J_{\mathcal{T}}$ can be found in Ref. [122].

The original underdamped TUR [124] contains an extra term

$$(4.41) \qquad \Omega = 2\left\langle \left(\sum_i v_i \partial_{v_i} P^{ss}(\boldsymbol{r}, \boldsymbol{v})/P^{ss}(\boldsymbol{r}, \boldsymbol{v}) \right)^2 \right\rangle - 2N^2,$$

where N is the number of particle and $P(\boldsymbol{r}, \boldsymbol{v})$ is the probability of finding the particle at the position $\boldsymbol{r}$ with a velocity $\boldsymbol{v}$. The superscript ss stands for *steady state*. As we only consider the dynamics along x-direction, we have $\boldsymbol{r} \to x$ and $\boldsymbol{v} \to v_x$. In the steady state of our system, the particles visit every x with an equal probability. The velocity distribution is Gaussian-type with a standard deviation close to the thermal velocity, $\sqrt{k_B T/m}$ (see

Figure 4.15). Therefore,

$$\Omega = 2\left\langle \left(Nv\partial_v e^{-\frac{(v-\bar{v})^2}{2\sigma_v^2}} \Big/ e^{-\frac{(v-\bar{v})^2}{2\sigma_v^2}}\right)^2 \right\rangle - 2N^2$$

(4.42)
$$= 2N^2\langle [v(v-\bar{v})/\sigma_v^2]^2\rangle - 2N^2$$

$$= 0.$$

That is why we do not have this term in the main text.
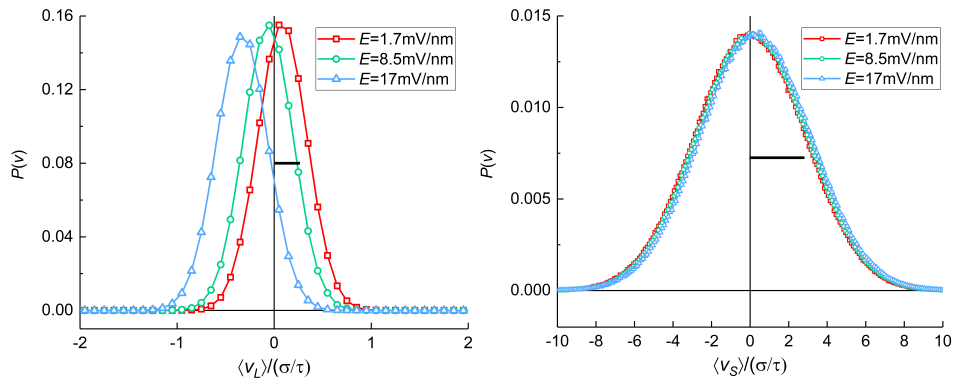
Figure 4.15. The steady state velocity distribution, $P^{ss}(v)$, of large (left) and small NPs (right) at different field strengths. Both are close to Gaussian-type. The black bar in each graph marks the thermal velocity, $\sqrt{k_B T/m}$.

4.6.3. Overdamped TUR in the underdamped dynamics

We derive a simple criterion to estimate if the overdamped TUR is applicable in the underdamped dynamics. From (4.2), the probability distribution function of particle velocity satisfies the following Fokker-Planck equation

$$(4.43) \qquad m\frac{\partial P(v,t)}{\partial t} = -\frac{\partial}{\partial v}\big[(-\nabla U + F_{ext} - \gamma v)P(v,t)\big] + \gamma k_B T\frac{\partial^2}{\partial v^2}P(v,t).$$

For simplicity, we have assumed the velocity can be decoupled from the position. Both $-\nabla U$ and F_{ext} are functions of the field strength, E, but are independent of the velocity. Hence, we can write $-\nabla U + F_{ext}$ as $f(E)$, whose details are discussed in the diffusion model in the main text. As in the steady state, $\partial P/\partial t = 0$, we solve (4.43) and obtain

$$(4.44) \qquad P^{ss}(v) = \frac{1}{\sqrt{2\pi k_B T/m}}\exp\left[-\frac{m(v - f(E)/\gamma)^2}{2k_B T}\right].$$

This gives

$$(4.45) \qquad \langle v\rangle = \frac{f(E)}{\gamma},$$

$$(4.46) \qquad \mathrm{var}(v) = \frac{k_B T}{m}.$$

The Gaussian form of (4.44) as well as (4.46) are consistent with Figure 4.15. The variance of the velocity equals the strength of the thermal motion, as a result of the thermal noise being the only stochastic source of the dynamics. Thus, the EP rate ((4.11)) becomes

$$(4.47) \qquad \langle\dot\Sigma\rangle = \frac{N\gamma}{T}[\langle v^2\rangle - \mathrm{var}(v)] = \frac{N\gamma\langle v\rangle^2}{T}.$$

Also, since $j = \sum_i q_i v_i$, we have

$$(4.48) \qquad \frac{\text{var}(j)}{\langle j \rangle^2} = \frac{\text{var}(v)}{N \langle v \rangle^2}.$$

Combining (4.47) and (4.48), we can evaluate the product of the current precision and the EP rate as

$$(4.49) \qquad \frac{\text{var}(j)}{\langle j \rangle^2} \langle \dot{\Sigma} \rangle = \frac{\text{var}(v)}{\langle v \rangle^2} \frac{\gamma \langle v \rangle^2}{T} = \frac{\gamma k_B}{m}.$$

The overdamped TUR [126] states that

$$(4.50) \qquad \frac{\text{var}(j)}{\langle j \rangle^2} \geq \frac{2 k_B}{\langle \dot{\Sigma} \rangle}.$$

This means

$$(4.51) \qquad \frac{m}{\gamma} < \frac{1}{2}.$$

We know that when the ratio of inertia and the damping strength is much smaller than 1, $m/\gamma \ll 1$, the underdamped Langevin dynamics reduce to the overdamped dynamics. Here, (4.51) shows that m/γ can also serve as a criterion for when we can use the overdamped TUR in the underdamped dynamics. However, the assumption made in the derivation that the position and the velocity can be decoupled holds only in homogeneous systems or when the velocity is fast enough to average out the spatial inhomogeneity. Thus, (4.51) is not rigorous but a rough estimation. Also as a result, in our system, (4.51) is more precise at strong fields than at weak fields.

4.6.4. Table of simulation parameters

Table 4.1. Simulation parameters in this study.

Parameter	Value
$R_{large\ particle}$	5 nm
$R_{small\ particle}$	1 nm
$q_{large\ particle}$	-80 e
$q_{small\ particle}$	$+10$ e
ϵ_r	80
η_0	0.89 mPa $\cdot$ s
$\rho_{particle}$	10 g/cm^3
ε (energy unit)	1.56 kJ/mol
σ (length unit)	1 nm
m (mass unit)	2×10^{-22} kg
τ (time unit)	2.85×10^{-10}s

4.6.5. Temperature hysteresis curves
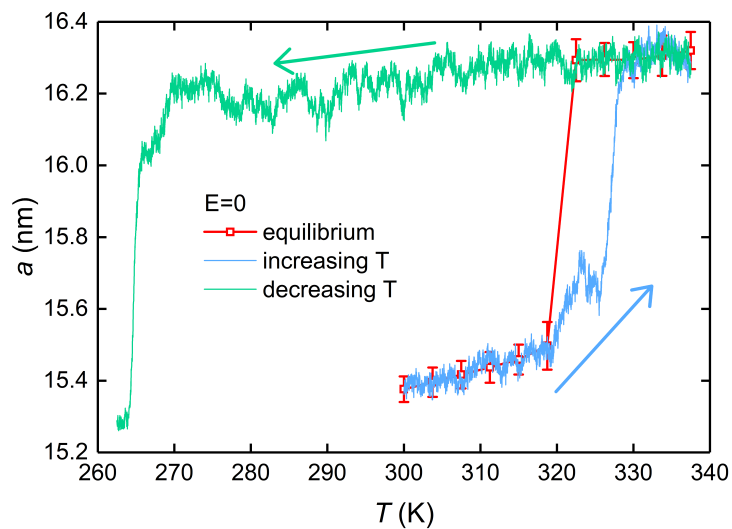
Figure 4.16. The temperature hysteresis curves of the lattice constant under zero external electric field. The red dots are the equilibrium lattice constant values at different temperatures in the NPT simulations, which are the same as the data in Figure 2A in the main text. After equilibrating the crystal at $T = 300\,\mathrm{K}$, we increase the heat bath temperature to $338\,\mathrm{K}$ at a constant rate $(\mathrm{d}T/\mathrm{d}t = 2.67 \times 10^7\,\mathrm{K/s})$ and the blue curve shows the lattice constant. The green curve shows the lattice constant of the opposite path. We do not consider the freezing of water here.

4.6.6. Equilibration of the system
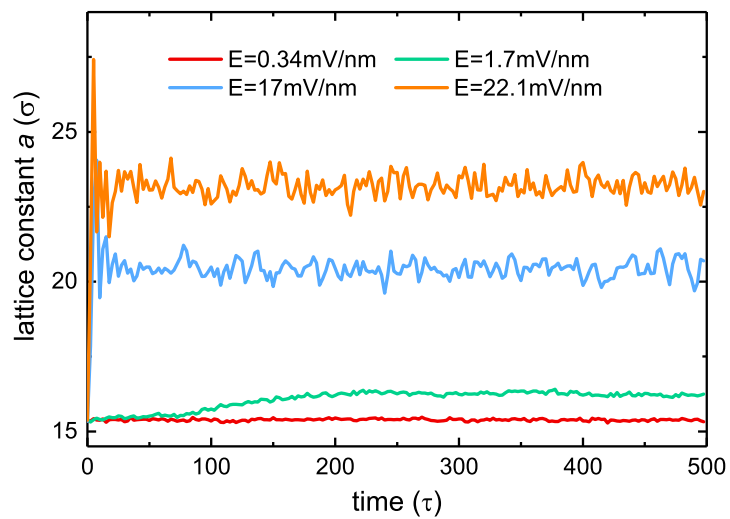
Figure 4.17. The lattice constant parallel to the electric field over time since the field is applied.

4.6.7. Radial distribution functions in three states
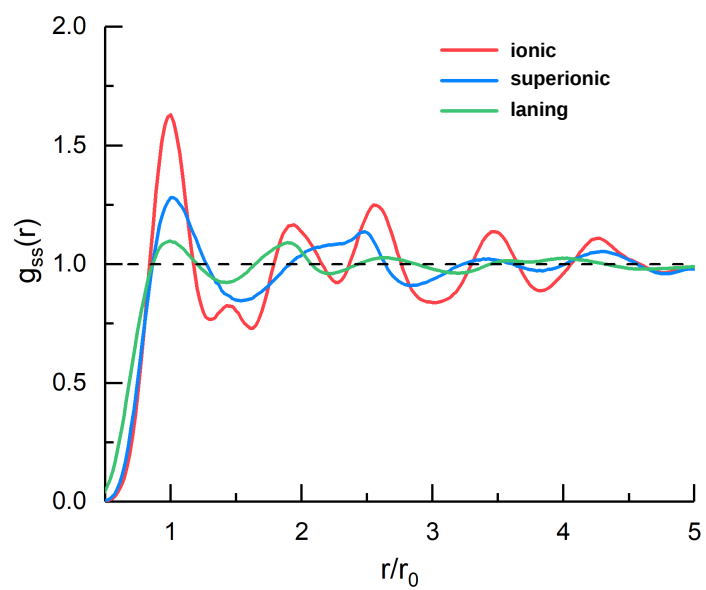
Figure 4.18. The radial distribution functions between small and small NPs in ionic, superionic, and laning states. Here, r_0 is the position of the first peak in each function.

4.6.8. Total acting force under different integration timesteps
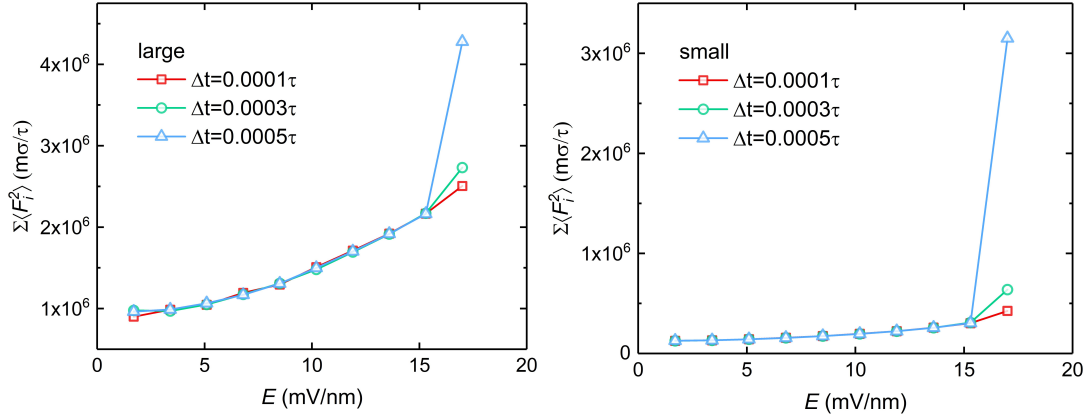
Figure 4.19. The ensemble average of the total acting force, $\sum_i \langle F_i^2 \rangle$, of large (left) and small (right) NPs under different integration timesteps. At strong fields, a large timestep ($\Delta t = 0.0005\tau$ would result in strong overlaps between particles. Hence, abrupt increases in $\sum_i \langle F_i^2 \rangle$ occur, which are carried into the calculations of the dynamical activities. This sampling problem can be mitigated by using a smaller timestep to reduce the overlaps between particles.

CHAPTER 5

Summary and outlooks

5.1. Summary of the dissertation

This dissertation employed a combination of theoretical analysis and simulations to investigate the newly discovered superionic phase in charged colloidal assemblies. The research encompassed the entire timeline, starting from the initial observation of the superionic phase to exploring phase transitions and dynamic behaviors under the influence of an electric field. Our usage of a simple coarse-grained (CG) model with dimensionless parameters ensures the generality of our findings.

Chapter 2 focused on a binary colloidal system, where large and small particles with opposite charges assemble into crystals through electrostatic interactions. By increasing the temperature, we observed a transition of the small particles from localized positions in the crystal's interstices to a delocalized and roaming state, while still effectively binding the large particles together. This entropy-driven sublattice melting exhibited a first-order transition at specific number ratios, which we characterized using Wyckoff positions.

In Chapter 3, we extended our research from isolated crystals to a mixture of crystals and solution, accounting for material exchange. We discovered that, in addition to temperature, an increase in the concentration of small particles in the solution could induce sublattice melting and an ionic-to-superionic transition. This transition was accompanied by lattice expansion and the incorporation of more small particles into the crystal.

Theoretical analysis revealed that the Madelung constant summation method accurately calculated the electrostatic potential energy in the ionic state, while the Wigner-Seitz cell approach described the superionic state. The phonon model captured the hardcore repulsion. Our free energy calculations indicated that the ionic-to-superionic transition was driven by enthalpy when the material exchange was allowed.

The results presented in Chapters 2 and 3 demonstrated the versatile nature of the superionic transition. On one hand, predicting transition behaviors is challenging due to the sensitivity to environmental conditions. On the other hand, the complexity of the transition opens up opportunities for engineering applications once a comprehensive understanding is achieved.

Chapter 4 explored the behaviors of charged colloidal crystals under an electric field. As the field strength increased, multiple phase transitions occurred, progressing from ionic to superionic states and eventually forming laning states, which facilitated faster material transport. In the superionic state, the mobility of charged colloidal particles was comparable to that of ions in water, indicating the potential for charged colloidal crystals to serve as superionic conductors and as models for studying superionic conduction properties. At the transport limit, the system exhibited precise charge transport described by Arrhenius's law, while the dissipation and system's charge currents demonstrated a tradeoff relationship with increasing field strength. We established that, in the transport limit, the product of dissipation and current precision converged to the system's damping degree. These findings provide theoretical insights for enhancing energy-conversion efficiency in future applications.

Overall, our research expands the realm of nanoparticle engineering and demonstrates the utility of colloidal systems for unraveling mechanisms in more fundamental systems.

5.2. Outlook for future work

In our research, we have primarily focused on the study of assemblies composed of simple colloidal particles, which we have modeled as isotropic spheres. However, it is worth noting that our system can readily be extended to investigate more complex systems. Furthermore, we firmly believe that our observations and conclusions hold relevance across various other systems. As a result, it is crucial to continue our research in diverse future directions to expand our understanding of these phenomena.

One intriguing avenue for future exploration is the investigation of the superionic phase in assemblies of colloidal particles featuring interacting patchy domains. By incorporating these domains, we can introduce the concept of *valency* and directional bonding into the system. Through controlled adjustments of the interaction strength, we can effectively manipulate the reversible condensation and release of the patchy particles. It is anticipated that in the ionic state, the assembly will assume a distinct structure due to the presence of static directional bondings. However, in the superionic state, the structure may become more symmetric as the bondings become dynamic. Consequently, these structural transformations have the potential to enable the realization of specific mechanical functions through the assembly's morphological changes.

Expanding the study of patchy particle systems to include macromolecule systems presents another promising direction. For instance, proteins exhibit interactions through their surface domains, which possess positive or negative charges and varying degrees

of hydrophilicity. Such interactions allow proteins to either self-aggregate or coassemble with other soft matter components. A particularly valuable goal is to identify the localized-to-delocalized transition within protein aggregates, which could revolutionize protein separation and purification techniques. However, simulating macromolecules or bio-molecules computationally is inherently expensive. To tackle this challenge, we have developed a numerical method based on the spherical harmonic expansion. This method, detailed in Appendix A of the dissertation, enables fast simulations of macromolecule systems, offering a practical solution to computational limitations.

Lastly, it is expected that field-induced superionicity will find application and exist in various other systems. One such example is iontronics, where ions navigate intricate networks formed by soft matter like polymers, functioning as carriers of signals [25]. As the intensity of the applied electric field increases, the mobility of ions may undergo a significant boost, indicating a superionic transition. Additionally, the polymer network, being more flexible than colloidal crystals, can exhibit more intricate structural changes. The insights gained from our research, along with the methodologies employed, such as osmotic ensemble simulations, diffusion models, and dissipation calculations, can lay a solid foundation for exploring the physics of such complex systems. By applying similar approaches, we can delve into the behavior of these intricate systems and uncover their distinct characteristics. This exploration holds great potential for developing novel materials with enhanced functionalities and a wide range of applications.

In conclusion, our research on assemblies of simple colloidal particles has served as a foundation for further exploration in a multitude of directions. By delving into the study of patchy particle systems, extending our investigations to macromolecule systems, and

probing the possibilities of field-induced superionicity, we can advance our understanding of complex systems and their practical applications. These future research directions will undoubtedly contribute to the broader field of materials science, paving the way for new technological advancements and fostering innovative solutions to current challenges.

References

[1] Kang Xu. Nonaqueous liquid electrolytes for lithium-based rechargeable batteries. *Chemical reviews*, 104(10):4303–4418, 2004.

[2] G Feuillade and Ph Perche. Ion-conductive macromolecular gels and membranes for solid lithium cells. *Journal of Applied Electrochemistry*, 5:63–69, 1975.

[3] Aiping Wang, Sanket Kadam, Hong Li, Siqi Shi, and Yue Qi. Review on modeling of the anode solid electrolyte interphase (sei) for lithium-ion batteries. *npj Computational Materials*, 4(1):15, 2018.

[4] Yaguang Zhang, Ning Du, and Deren Yang. Designing superior solid electrolyte interfaces on silicon anodes for high-performance lithium-ion batteries. *Nanoscale*, 11(41):19086–19104, 2019.

[5] Albert J Fry. *Synthetic organic electrochemistry.* John Wiley & Sons, Hoboken, NJ, USA, 1989.

[6] Kazunori Ozawa. Lithium-ion rechargeable batteries with licoo2 and carbon electrodes: the licoo2/c system. *Solid State Ionics*, 69(3-4):212–221, 1994.

[7] AD Robertson, AR West, and AG Ritchie. Review of crystalline lithium-ion conductors suitable for high temperature battery applications. *Solid State Ionics*, 104(1-2):1–11, 1997.

[8] Zhizhen Zhang, Yuanjun Shao, Bettina Lotsch, Yong-Sheng Hu, Hong Li, Jürgen Janek, Linda F Nazar, Ce-Wen Nan, Joachim Maier, Michel Armand, et al. New horizons for inorganic solid state ion conductors. *Energy & Environmental Science*, 11(8):1945–1976, 2018.

[9] Abhik Banerjee, Kern Ho Park, Jongwook W Heo, Young Jin Nam, Chang Ki Moon, Seung M Oh, Seung-Tae Hong, and Yoon Seok Jung. Na3sbs4: a solution processable sodium superionic conductor for all-solid-state sodium-ion batteries. *Angewandte Chemie*, 128(33):9786–9790, 2016.

[10] Myron Ben Salamon. *Physics of superionic conductors*, volume 15. Springer Science & Business Media, Berlin, Germany, 2013.

[11] A Zimmers, L Aigouy, M Mortier, A Sharoni, Siming Wang, KG West, JG Ramirez, and Ivan K Schuller. Role of thermal heating on the voltage induced insulator-metal transition in vo 2. *Physical review letters*, 110(5):056601, 2013.

[12] JGP Binner, G Dimitrakis, DM Price, M Reading, and B Vaidhyanathan. Hysteresis in the β–α phase transition in silver iodide. *Journal of thermal analysis and calorimetry*, 84:409–412, 2006.

[13] Noriaki Kamaya, Kenji Homma, Yuichiro Yamakawa, Masaaki Hirayama, Ryoji Kanno, Masao Yonemura, Takashi Kamiyama, Yuki Kato, Shigenori Hama, Koji Kawamoto, et al. A lithium superionic conductor. *Nature materials*, 10(9):682–686, 2011.

[14] Yan Wang, William Davidson Richards, Shyue Ping Ong, Lincoln J Miara, Jae Chul Kim, Yifei Mo, and Gerbrand Ceder. Design principles for solid-state lithium superionic conductors. *Nature materials*, 14(10):1026, 2015.

[15] William D Richards, Tomoyuki Tsujimura, Lincoln J Miara, Yan Wang, Jae Chul Kim, Shyue Ping Ong, Ichiro Uechi, Naoki Suzuki, and Gerbrand Ceder. Design and synthesis of the superionic conductor na10snp2s12. *Nature communications*, 7(1):1–8, 2016.

[16] John Christopher Bachman, Sokseiha Muy, Alexis Grimaud, Hao-Hsun Chang, Nir Pour, Simon F Lux, Odysseas Paschos, Filippo Maglia, Saskia Lupart, Peter Lamp, et al. Inorganic solid-state electrolytes for lithium batteries: mechanisms and properties governing ion conduction. *Chemical reviews*, 116(1):140–162, 2016.

[17] KyuJung Jun, Yingzhi Sun, Yihan Xiao, Yan Zeng, Ryounghee Kim, Haegyeom Kim, Lincoln J Miara, Dongmin Im, Yan Wang, and Gerbrand Ceder. Lithium superionic conductors with corner-sharing frameworks. *Nature Materials*, pages 1–8, 2022.

[18] Hiram Kwak, Shuo Wang, Juhyoun Park, Yunsheng Liu, Kyu Tae Kim, Yeji Choi, Yifei Mo, and Yoon Seok Jung. Emerging halide superionic conductors for all-solid-state batteries: Design, synthesis, and practical applications. *ACS Energy Letters*, 7(5):1776–1805, 2022.

[19] Linfeng Zhang, Han Wang, Roberto Car, and E Weinan. Phase diagram of a deep potential water model. *Physical review letters*, 126(23):236001, 2021.

[20] Jean-Alexis Hernandez and Razvan Caracas. Superionic-superionic phase transitions in body-centered cubic h 2 o ice. *Physical review letters*, 117(13):135503, 2016.

[21] Jiming Sun, Bryan K Clark, Salvatore Torquato, and Roberto Car. The phase diagram of high-pressure superionic ice. *Nature communications*, 6(1):1–8, 2015.

[22] Marius Millot, Federica Coppari, J Ryan Rygg, Antonio Correa Barrios, Sebastien Hamel, Damian C Swift, and Jon H Eggert. Nanosecond x-ray diffraction of shock-compressed superionic water ice. *Nature*, 569(7755):251–255, 2019.

[23] C Cavazzoni, GL Chiarotti, S Scandolo, E Tosatti, M Bernasconi, and M Parrinello. Superionic and metallic states of water and ammonia at giant planet conditions. *Science*, 283(5398):44–46, 1999.

[24] Yangyang Wang, Fei Fan, Alexander L Agapov, Xiang Yu, Kunlun Hong, Jimmy Mays, and Alexei P Sokolov. Design of superionic polymers—new insights from walden plot analysis. *Solid State Ionics*, 262:782–784, 2014.

[25] Seamus D Jones, Howie Nguyen, Peter M Richardson, Yan-Qiao Chen, Kira E Wyckoff, Craig J Hawker, Raphaële J Clément, Glenn H Fredrickson, and Rachel A Segalman. Design of polymeric zwitterionic solid electrolytes with superionic lithium

transport. *ACS Central Science*, 8(2):169–175, 2022.

[26] MA Subramanian, Rajeevi Subramanian, and A Clearfield. Lithium ion conductors in the system ab (iv) 2 (po4) 3 (b= ti, zr and hf). *Solid State Ionics*, 18:562–569, 1986.

[27] Ryoji Kanno, Takayuki Hata, Yoji Kawamoto, and Michihiko Irie. Synthesis of a new lithium ionic conductor, thio-lisicon–lithium germanium sulfide system. *Solid state ionics*, 130(1-2):97–104, 2000.

[28] Venkataraman Thangadurai and Werner Weppner. Li6ala2nb2o12 (a= ca, sr, ba): A new class of fast lithium ion conductors with garnet-like structure. *Journal of the American Ceramic Society*, 88(2):411–418, 2005.

[29] Alexandra Emly, Emmanouil Kioupakis, and Anton Van der Ven. Phase stability and transport mechanisms in antiperovskite li3ocl and li3obr superionic conductors. *Chemistry of Materials*, 25(23):4663–4670, 2013.

[30] James B Boyce and Bernardo A Huberman. Superionic conductors: Transitions, structures, dynamics. *Physics Reports*, 51(4):189–265, 1979.

[31] AS Dworkin and Max A Bredig. Diffuse transition and melting in fluorite and antifluorite type of compounds. heat content of potassium sulfide from 298 to 1260. degree. k. *The Journal of Physical Chemistry*, 72(4):1277–1281, 1968.

[32] Yange Lin and Monica Olvera de la Cruz. Sublattice melting in binary superionic colloidal crystals. *Physical Review E*, 101(3):032603, 2020.

[33] Peter J Lu and David A Weitz. Colloidal particles: crystals, glasses, and gels. *Annu. Rev. Condens. Matter Phys.*, 4(1):217–233, 2013.

[34] Ling Zhang, Jake B Bailey, Rohit H Subramanian, Alexander Groisman, and F Akif Tezcan. Hyperexpandable, self-healing macromolecular crystals with integrated polymer networks. *Nature*, 557(7703):86, 2018.

[35] Étienne Ducrot, Mingxin He, Gi-Ra Yi, and David J Pine. Colloidal alloys with preassembled clusters and spheres. *Nature materials*, 16(6):652, 2017.

[36] Dmitriy S Dolzhnikov, Hao Zhang, Jaeyoung Jang, Jae Sung Son, Matthew G Panthani, Tomohiro Shibata, Soma Chattopadhyay, and Dmitri V Talapin. Composition-matched molecular "solders" for semiconductors. *Science*, 347(6220):425–428, 2015.

[37] Anand Yethiraj and Alfons van Blaaderen. A colloidal model system with an interaction tunable from hard sphere to soft and dipolar. *Nature*, 421(6922):513, 2003.

[38] Khoa N Pham, Antonio M Puertas, Johan Bergenholtz, Stefan Ulrich Egelhaaf, A Moussaıd, Peter N Pusey, Andrew B Schofield, Michael E Cates, Matthias Fuchs, and Wilson CK Poon. Multiple glassy states in a simple model system. *Science*, 296(5565):104–106, 2002.

[39] Lang Feng, Bezia Laderman, Stefano Sacanna, and Paul Chaikin. Re-entrant solidification in polymer–colloid mixtures as a consequence of competing entropic and enthalpic attractions. *Nature materials*, 14(1):61, 2015.

[40] C Patrick Royall, Mirjam E Leunissen, and A Van Blaaderen. A new colloidal model system to study long-range interactions quantitatively in real space. *Journal of Physics: Condensed Matter*, 15(48):S3581, 2003.

[41] Mirjam E Leunissen, Christina G Christova, Antti-Pekka Hynninen, C Patrick Royall, Andrew I Campbell, Arnout Imhof, Marjolein Dijkstra, Rene Van Roij, and Alfons Van Blaaderen. Ionic colloidal crystals of oppositely charged particles. *Nature*, 437(7056):235, 2005.

[42] Mauri A Kostiainen, Panu Hiekkataipale, Ari Laiho, Vincent Lemieux, Jani Seitsonen, Janne Ruokolainen, and Pierpaolo Ceci. Electrostatic assembly of binary nanoparticle superlattices using protein cages. *Nature nanotechnology*, 8(1):52, 2013.

[43] Ville Liljeström, Joona Mikkilä, and Mauri A Kostiainen. Self-assembly and modular functionalization of three-dimensional crystals from oppositely charged proteins. *Nature Comm.*, 5:4445, 2014.

[44] Markus Bier, René van Roij, and Marjolein Dijkstra. Phase diagrams of binary mixtures of oppositely charged colloids. *J. Chem. Phys.*, 133(12):124501, 2010.

[45] MD Eldridge, PA Madden, and D Frenkel. Entropy-driven formation of a superlattice in a hard-sphere binary mixture. *Nature*, 365(6441):35, 1993.

[46] Marjolein Dijkstra, René van Roij, and Robert Evans. Direct simulation of the phase behavior of binary hard-sphere mixtures: test of the depletion potential description. *Phys. Rev. Lett.*, 82(1):117, 1999.

[47] Yaohua Li, Martin Girard, Meng Shen, Jaime Andres Millan, and Monica Olvera de la Cruz. Strong attractions and repulsions mediated by monovalent salts. *Proceedings of the National Academy of Sciences*, 114(45):11838–11843, 2017.

[48] Kaylie L Young, Michelle L Personick, Michael Engel, Pablo F Damasceno, Stacey N Barnaby, Reiner Bleher, Tao Li, Sharon C Glotzer, Byeongdu Lee, and Chad A Mirkin. A directional entropic force approach to assemble anisotropic nanoparticles into superlattices. *Angewandte Chemie International Edition*, 52(52):13980–13984, 2013.

[49] Thi Vo and Sharon C Glotzer. A theory of entropic bonding. *Proceedings of the National Academy of Sciences*, 119(4):e2116414119, 2022.

[50] Yein Lim, Sangmin Lee, and Sharon C Glotzer. Engineering the thermodynamic stability and metastability of mesophases of colloidal bipyramids through shape entropy. *ACS nano*, 17(5):4287–4295, 2023.

[51] Sangmin Lee and Sharon C Glotzer. Entropically engineered formation of fivefold and icosahedral twinned clusters of colloidal shapes. *Nature Communications*, 13(1):7362, 2022.

[52] Andriy Nych, Ulyana Ognysta, Miha Škarabot, Miha Ravnik, Slobodan Žumer, and Igor Muševič. Assembly and control of 3d nematic dipolar colloidal crystals. *Nature communications*, 4(1):1489, 2013.

[53] Franz X Redl, K-S Cho, Christopher B Murray, and Stephen O'Brien. Three-dimensional binary superlattices of magnetic nanocrystals and semiconductor quantum dots. *Nature*, 423(6943):968, 2003.

[54] Aldo Spatafora-Salazar, Dana M Lobmeyer, Lucas HP Cunha, Kedar Joshi, and Sibani Lisa Biswal. Hierarchical assemblies of superparamagnetic colloids in time-varying magnetic fields. *Soft Matter*, 17(5):1120–1155, 2021.

[55] Sabine HL Klapp. Collective dynamics of dipolar and multipolar colloids: From passive to active systems. *Current opinion in colloid & interface science*, 21:76–85, 2016.

[56] Chad A Mirkin, Robert L Letsinger, Robert C Mucic, and James J Storhoff. A dna-based method for rationally assembling nanoparticles into macroscopic materials. *Nature*, 382(6592):607–609, 1996.

[57] Sung Yong Park, Abigail KR Lytton-Jean, Byeongdu Lee, Steven Weigand, George C Schatz, and Chad A Mirkin. Dna-programmable nanoparticle crystallization. *Nature*, 451(7178):553–556, 2008.

[58] James J Storhoff and Chad A Mirkin. Programmed materials synthesis with dna. *Chemical Reviews*, 99(7):1849–1862, 1999.

[59] Ziyi Miao, Cindy Y Zheng, George C Schatz, Byeongdu Lee, and Chad A Mirkin. Low-density 2d superlattices assembled via directional dna bonding. *Angewandte Chemie*, 133(35):19183–19188, 2021.

[60] Congzhi Liu, Yaoxuan Chen, Jian Zhao, Yong Wang, Yulei Shao, Zhanjun Gu, Lele Li, and Yuliang Zhao. Self-assembly of copper–dnazyme nanohybrids for dual-catalytic tumor therapy. *Angewandte Chemie*, 133(26):14445–14449, 2021.

[61] Aaron E Saunders and Brian A Korgel. Observation of an ab phase in bidisperse nanocrystal superlattices. *ChemPhysChem*, 6(1):61–65, 2005.

[62] Martin Girard, Shunzhi Wang, Jingshan S Du, Anindita Das, Ziyin Huang, Vinayak P Dravid, Byeongdu Lee, Chad A Mirkin, and Monica Olvera de la Cruz. Particle analogs of electrons in colloidal crystals. *Science*, 364(6446):1174–1178, 2019.

[63] Hector Lopez-Rios, Ali Ehlen, and Monica Olvera de la Cruz. Delocalization transition in colloidal crystals. *The Journal of Physical Chemistry C*, 125(1):1096–1106, 2021.

[64] Ali Ehlen, Hector Lopez-Rios, and Monica Olvera de la Cruz. Metallization of colloidal crystals. *Physical Review Materials*, 5(11):115601, 2021.

[65] Shunzhi Wang, Sangmin Lee, Jingshan S Du, Benjamin E Partridge, Ho Fung Cheng, Wenjie Zhou, Vinayak P Dravid, Byeongdu Lee, Sharon C Glotzer, and Chad A Mirkin. The emergence of valency in colloidal crystals through electron equivalents. *Nature materials*, 21(5):580–587, 2022.

[66] Luis A Padilla, Andres A León-Islas, Jesse Funkhouser, Julio C Armas-Pérez, and Abelardo Ramírez-Hernández. Dynamics and phase behavior of two-dimensional size-asymmetric binary mixtures of core-softened colloids. *The Journal of Chemical*

Physics, 155(21):214901, 2021.

[67] D Gersappe, JM Deutsch, and M Olvera de la Cruz. Density fluctuations of self-avoiding walks in random systems. *Phys. Rev. Lett.*, 66(6):731, 1991.

[68] Niels Boon, Guillermo Ivan Guerrero-García, René Van Roij, and Monica Olvera de la Cruz. Effective charges and virial pressure of concentrated macroion solutions. *Proceedings of the National Academy of Sciences*, 112(30):9242–9246, 2015.

[69] Steve Plimpton. Fast parallel algorithms for short-range molecular dynamics. *J. Comp. Phys.*, 117(1):1–19, 1995.

[70] Daan Frenkel and Berend Smit. *Understanding molecular simulation: from algorithms to applications*, volume 1. Elsevier, Amsterdam, Netherlands, 2001.

[71] Theo Hahn. *International tables for crystallography: Brief teaching edition of volume A, Space-group symmetry*, volume 1. Kluwer Academic Pub, Berlin, Germany, 1996.

[72] L Filion, M Hermes, R Ni, ECM Vermolen, A Kuijk, CG Christova, JCP Stiefelhagen, T Vissers, A Van Blaaderen, and M Dijkstra. Self-assembly of a colloidal interstitial solid with tunable sublattice doping. *Phys. Rev. Lett.*, 107(16):168302, 2011.

[73] SA Brazovskii. Phase transition of an isotropic system to a nonuniform state. *Soviet Journal of Experimental and Theoretical Physics*, 41:85, 1975.

[74] Kurt Binder, Benjamin J Block, Peter Virnau, and Andreas Tröster. Beyond the van der waals loop: What can be learned from simulating lennard-jones fluids inside the region of phase coexistence. *American Journal of Physics*, 80(12):1099–1109, 2012.

[75] LE Sánchez-Díaz, A Vizcarra-Rendón, and R Juárez-Maldonado. Ionic and wigner glasses, superionic conductors, and spinodal electrostatic gels: dynamically arrested phases of the primitive model. *Physical review letters*, 103(3):035701, 2009.

[76] Jos W Zwanikken and Monica Olvera de la Cruz. Tunable soft structure in charged fluids confined by dielectric interfaces. *Proceedings of the National Academy of Sciences*, 110(14):5301–5308, 2013.

[77] Yange Lin and Monica Olvera de la Cruz. Superionic colloidal crystals: Ionic to metallic bonding transitions. *The Journal of Physical Chemistry B*, 126(35):6740–6749, 2022.

[78] Tong Bian, Andrea Gardin, Julius Gemen, Lothar Houben, Claudio Perego, Byeongdu Lee, Nadav Elad, Zonglin Chu, Giovanni M Pavan, and Rafal Klajn. Electrostatic co-assembly of nanoparticles with oppositely charged small molecules into static and dynamic superstructures. *Nature Chemistry*, 13(10):940–949, 2021.

[79] Niels Boon, Guillermo Ivan Guerrero-García, René Van Roij, and Monica Olvera de la Cruz. Effective charges and virial pressure of concentrated macroion solutions. *Proceedings of the National Academy of Sciences*, 112(30):9242–9246, 2015.

[80] Guillaume Bareigts and Christophe Labbez. Effective pair potential between charged nanoparticles at high volume fractions. *Physical Chemistry Chemical Physics*, 19(6):4787–4792, 2017.

[81] Yannick Hallez and Martine Meireles. Fast, robust evaluation of the equation of state of suspensions of charge-stabilized colloidal spheres. *Langmuir*, 33(38):10051–10060, 2017.

[82] Chongyang Shen, Scott Bradford, Zhan Wang, Yuanfang Huang, Yulong Zhang, and Baoguo Li. Dlvo interaction energies between hollow spherical particles and collector surfaces. *Langmuir*, 33(40):10455–10467, 2017.

[83] Francisco J Solis and Monica Olvera de la Cruz. Collapse of flexible polyelectrolytes in multivalent salt solutions. *The Journal of Chemical Physics*, 112(4):2030–2035, 2000.

[84] Howard G Schild. Poly (n-isopropylacrylamide): experiment, theory and application. *Progress in polymer science*, 17(2):163–249, 1992.

[85] M Muthukumar. 50th anniversary perspective: A perspective on polyelectrolyte solutions. *Macromolecules*, 50(24):9528–9560, 2017.

[86] De-Wei Yin, Monica Olvera de la Cruz, and Juan J de Pablo. Swelling and collapse of polyelectrolyte gels in equilibrium with monovalent and divalent electrolyte solutions. *The Journal of chemical physics*, 131(19):194907, 2009.

[87] Carlos Vega, José LF Abascal, Carl McBride, and Fernando Bresme. The fluid–solid equilibrium for a charged hard sphere model revisited. *The Journal of chemical physics*, 119(2):964–971, 2003.

[88] LE Sánchez-Díaz, A Vizcarra-Rendón, and R Juárez-Maldonado. Ionic and wigner glasses, superionic conductors, and spinodal electrostatic gels: Dynamically arrested phases of the primitive model. *Physical review letters*, 103(3):035701, 2009.

[89] Eugene Wigner and Frederick Seitz. On the constitution of metallic sodium. *Physical Review*, 43(10):804, 1933.

[90] Charles Kittel and Paul McEuen. *Introduction to solid state physics*. John Wiley & Sons, Hoboken, NJ, USA, 2018.

[91] FW De Wette. Comments on the electrostatic energy of a wigner solid. *Physical Review B*, 21(8):3751, 1980.

[92] K Fuchs. A quantum mechanical investigation of the cohesive forces of metallic copper. *Proceedings of the Royal Society of London. Series A-Mathematical and Physical Sciences*, 151(874):585–602, 1935.

[93] Leonard Kleinman. Comment on the average potential of a wigner solid. *Physical Review B*, 24(12):7412, 1981.

[94] W Michael Brown, Peng Wang, Steven J Plimpton, and Arnold N Tharrington. Implementing molecular dynamics on hybrid high performance computers–short range forces. *Computer Physics Communications*, 182(4):898–911, 2011.

[95] W Michael Brown, Axel Kohlmeyer, Steven J Plimpton, and Arnold N Tharrington. Implementing molecular dynamics on hybrid high performance computers–particle–particle particle-mesh. *Computer Physics Communications*, 183(3):449–459, 2012.

[96] Y. Masako W. M. Brown. Implementing molecular dynamics on hybrid high performance computers –three-body potentials. *Comp. Phys. Comm.*, 184:2785–2793,

2013.

[97] S. J. Plimpton T. D. Nguyen. Accelerating dissipative particle dynamics simulations for soft matter systems. *Comput. Mater. Sci.*, 100:173–180, 2015.

[98] T. D. Nguyen. Gpu-accelerated tersoff potentials for massively parallel molecular dynamics simulations. *Comp. Phys. Comm.*, 212:113–122, 2017.

[99] William Humphrey, Andrew Dalke, and Klaus Schulten. Vmd: visual molecular dynamics. *Journal of molecular graphics*, 14(1):33–38, 1996.

[100] Chunyan Fan, DD Do, David Nicholson, and E Ustinov. Chemical potential, helmholtz free energy and entropy of argon with kinetic monte carlo simulation. *Molecular Physics*, 112(1):60–73, 2014.

[101] EA Ustinov. Thermodynamics and simulation of hard-sphere fluid and solid: Kinetic monte carlo method versus standard metropolis scheme. *The Journal of chemical physics*, 146(3):034110, 2017.

[102] Georgios C Boulougouris, Ioannis G Economou, and Doros N Theodorou. On the calculation of the chemical potential using the particle deletion scheme. *Molecular physics*, 96(6):905–913, 1999.

[103] Jasper N Immink, Maxime J Bergman, JJ Erik Maris, Joakim Stenhammar, and Peter Schurtenberger. Crystal-to-crystal transitions in binary mixtures of soft colloids. *ACS nano*, 14(11):14861–14868, 2020.

[104] Eric Raspaud, Thomas Forth, Carlos São-José, Paulo Tavares, and Marta De Frutos. A kinetic analysis of dna ejection from tailed phages revealing the prerequisite activation energy. *Biophysical Journal*, 93(11):3999–4005, 2007.

[105] Francisco J Solis and Monica Olvera de la Cruz. Flexible linear polyelectrolytes in multivalent salt solutions: Solubility conditions. *EPJ direct*, 2(1):1–18, 2000.

[106] Ho Fung Cheng, Shunzhi Wang, and Chad A Mirkin. Electron-equivalent valency through molecularly well-defined multivalent dna. *Journal of the American Chemical Society*, 143(4):1752–1757, 2021.

[107] Yange Lin and Monica Olvera de la Cruz. Colloidal superionic conductors. *Proceedings of the National Academy of Sciences*, 120(15):e2300257120, 2023.

[108] Milan Bier. *Electrophoresis: theory, methods, and applications.* Elsevier, 2013.

[109] B David Hames. *Gel electrophoresis of proteins: a practical approach*, volume 197. OUP Oxford, 1998.

[110] Teun Vissers, Adam Wysocki, Martin Rex, Hartmut Löwen, C Patrick Royall, Arnout Imhof, and Alfons van Blaaderen. Lane formation in driven mixtures of oppositely charged colloids. *Soft Matter*, 7(6):2352–2356, 2011.

[111] Bin Li, Yong-Lei Wang, Guang Shi, Yangyang Gao, Xinghua Shi, Clifford E Woodward, and Jan Forsman. Phase transitions of oppositely charged colloidal particles driven by alternating current electric field. *ACS nano*, 15(2):2363–2373, 2021.

[112] J Dzubiella, GP Hoffmann, and H Löwen. Lane formation in colloidal mixtures driven by an external field. *Physical Review E*, 65(2):021402, 2002.

[113] M Rex and H Löwen. Lane formation in oppositely charged colloids driven by an electric field: Chaining and two-dimensional crystallization. *Physical review E*, 75(5):051402, 2007.

[114] Fumihiko Nakamura, Mariko Sakaki, Yuya Yamanaka, Sho Tamaru, Takashi Suzuki, and Yoshiteru Maeno. Electric-field-induced metal maintained by current of the mott insulator ca2ruo4. *Scientific reports*, 3(1):1–6, 2013.

[115] K Ueno, S Nakamura, H Shimotani, A Ohtomo, N Kimura, T Nojima, H Aoki, Y Iwasa, and M Kawasaki. Electric-field-induced superconductivity in an insulator. *Nature materials*, 7(11):855–858, 2008.

[116] Giacomo Mazza, Adriano Amaricci, Massimo Capone, and Michele Fabrizio. Field-driven mott gap collapse and resistive switch in correlated insulators. *Physical review letters*, 117(17):176401, 2016.

[117] K Kishida, J Shibutani, T Hatano, Y Yokoyama, N Katayama, Y Okamoto, Y Nakamura, H Kishida, HS Suzuki, K Takehana, et al. Electrical-field-induced insulator-to-metal transition in samarium monosulfides. *Applied Physics Letters*, 121(12):121901, 2022.

[118] Andre C Barato and Udo Seifert. Thermodynamic uncertainty relation for biomolecular processes. *Physical review letters*, 114(15):158101, 2015.

[119] Todd R Gingrich, Jordan M Horowitz, Nikolay Perunov, and Jeremy L England. Dissipation bounds all steady-state current fluctuations. *Physical review letters*, 116(12):120601, 2016.

[120] Soham Pal, Sushant Saryal, Dvira Segal, TS Mahesh, and Bijay Kumar Agarwalla. Experimental study of the thermodynamic uncertainty relation. *Physical Review Research*, 2(2):022044, 2020.

[121] Udo Seifert. Stochastic thermodynamics: From principles to the cost of precision. *Physica A: Statistical Mechanics and its Applications*, 504:176–191, 2018.

[122] Jordan M Horowitz and Todd R Gingrich. Thermodynamic uncertainty relations constrain non-equilibrium fluctuations. *Nature Physics*, 16(1):15–20, 2020.

[123] Todd R Gingrich, Grant M Rotskoff, and Jordan M Horowitz. Inferring dissipation from current fluctuations. *Journal of Physics A: Mathematical and Theoretical*, 50(18):184004, 2017.

[124] Tan Van Vu and Yoshihiko Hasegawa. Uncertainty relations for underdamped langevin dynamics. *Physical Review E*, 100(3):032130, 2019.

[125] Christian Maes. Frenesy: Time-symmetric dynamical activity in nonequilibria. *Physics Reports*, 850:1–33, 2020.

[126] Rueih-Sheng Fu and Todd R Gingrich. Thermodynamic uncertainty relation for langevin dynamics by scaling time. *Physical Review E*, 106(2):024128, 2022.

[127] Ken Sekimoto. Kinetic characterization of heat bath and the energetics of thermal ratchet models. *Journal of the physical society of Japan*, 66(5):1234–1237, 1997.

[128] Rep Kubo. The fluctuation-dissipation theorem. *Reports on progress in physics*, 29(1):255, 1966.

[129] V. Stegailov V. Nikolskiy. Gpu acceleration of four-site water models in lammps. *Proceeding of the International Conference on Parallel Computing (ParCo 2019), Prague, Czech Republic*, 2019.

[130] Katherine Klymko, Phillip L Geissler, and Stephen Whitelam. Microscopic origin and macroscopic implications of lane formation in mixtures of oppositely driven particles. *Physical Review E*, 94(2):022608, 2016.

[131] Haiyang Niu, Yi Isaac Yang, and Michele Parrinello. Temperature dependence of homogeneous nucleation in ice. *Physical review letters*, 122(24):245501, 2019.

[132] Liang Xu, Zhigang Wang, Jian Chen, Songyi Chen, Wenge Yang, Yang Ren, Xiaobing Zuo, Jianrong Zeng, Qiang Wu, and Howard Sheng. Folded network and structural transition in molten tin. *Nature communications*, 13(1):1–10, 2022.

[133] Pablo M Piaggi, Omar Valsson, and Michele Parrinello. Enhancing entropy and enthalpy fluctuations to drive crystallization in atomistic simulations. *Physical Review Letters*, 119(1):015701, 2017.

[134] Pablo M Piaggi and Michele Parrinello. Predicting polymorphism in molecular crystals using orientational entropy. *Proceedings of the National Academy of Sciences*, 115(41):10251–10256, 2018.

[135] KL Galloway, EG Teich, XG Ma, Ch Kammer, IR Graham, NC Keim, C Reina, DJ Jerolmack, AG Yodh, and PE Arratia. Relationships between structure, memory and flow in sheared disordered materials. *Nature Physics*, 18(5):565–570, 2022.

[136] Andras Baranyai and Denis J Evans. Direct entropy calculation from computer simulation of liquids. *Physical Review A*, 40(7):3817, 1989.

[137] Cui Zhang, Leonardo Spanu, and Giulia Galli. Entropy of liquid water from ab initio molecular dynamics. *The Journal of Physical Chemistry B*, 115(48):14190–14195, 2011.

[138] S Koneshan, Jayendran C Rasaiah, RM Lynden-Bell, and SH Lee. Solvent structure, dynamics, and ion mobility in aqueous solutions at 25 c. *The Journal of Physical Chemistry B*, 102(21):4193–4204, 1998.

[139] LB Schein, A Peled, and D Glatz. The electric field dependence of the mobility in molecularly doped polymers. *Journal of Applied Physics*, 66(2):686–692, 1989.

[140] Chiara Lionello, Claudio Perego, Andrea Gardin, Rafal Klajn, and Giovanni M Pavan. Supramolecular semiconductivity through emerging ionic gates in ion–nanoparticle superlattices. *ACS nano*, 2022.

[141] Robert Marsland III, Wenping Cui, and Jordan M Horowitz. The thermodynamic uncertainty relation in biochemical oscillations. *Journal of the Royal Society Interface*, 16(154):20190098, 2019.

[142] Andreas Dechant and Shin-ichi Sasa. Current fluctuations and transport efficiency for general langevin systems. *Journal of Statistical Mechanics: Theory and Experiment*, 2018(6):063209, 2018.

[143] Gianmaria Falasco and Marco Baiesi. Nonequilibrium temperature response for stochastic overdamped systems. *New Journal of Physics*, 18(4):043039, 2016.

[144] Siewert J Marrink, H Jelger Risselada, Serge Yefimov, D Peter Tieleman, and Alex H De Vries. The martini force field: coarse grained model for biomolecular simulations. *The journal of physical chemistry B*, 111(27):7812–7824, 2007.

[145] Paulo CT Souza, Riccardo Alessandri, Jonathan Barnoud, Sebastian Thallmair, Ignacio Faustino, Fabian Grünewald, Ilias Patmanidis, Haleh Abdizadeh, Bart MH Bruininks, Tsjerk A Wassenaar, et al. Martini 3: a general purpose force field for coarse-grained molecular dynamics. *Nature methods*, 18(4):382–388, 2021.

[146] James F Dama, Anton V Sinitskiy, Martin McCullagh, Jonathan Weare, Benoît Roux, Aaron R Dinner, and Gregory A Voth. The theory of ultra-coarse-graining. 1. general principles. *Journal of chemical theory and computation*, 9(5):2466–2480, 2013.

[147] Aram Davtyan, James F Dama, Anton V Sinitskiy, and Gregory A Voth. The theory of ultra-coarse-graining. 2. numerical implementation. *Journal of chemical theory and computation*, 10(12):5265–5275, 2014.

[148] James F Dama, Jaehyeok Jin, and Gregory A Voth. The theory of ultra-coarse-graining. 3. coarse-grained sites with rapid local equilibrium of internal states. *Journal of Chemical Theory and Computation*, 13(3):1010–1022, 2017.

[149] Natalie Baddour. Operational and convolution properties of three-dimensional fourier transforms in spherical polar coordinates. *JOSA A*, 27(10):2144–2155, 2010.

[150] Martin Girard, Trung Dac Nguyen, and Monica Olvera De La Cruz. Orbitals for classical arbitrary anisotropic colloidal potentials. *Physical Review E*, 96(5):053309, 2017.

[151] Árpád Baricz. *Generalized Bessel functions of the first kind.* Springer, 2010.

[152] William Rowan Hamilton. *Elements of quaternions.* Longmans, Green, & Company, 1866.

[153] Michael Boyle. Angular velocity of gravitational radiation from precessing binaries and the corotating frame. *Physical Review D*, 87(10):104006, 2013.

APPENDIX A

Spherical Harmonic Expansion Method for Fast Computation

When modeling a N-body system where each body is made of M elementary particles, to evaluate the interaction between two bodies, we need to go through and sum up all the interactions of particle-particle pair. In such cases, the computational time is in the order of $\mathcal{O}(M^2)$. Although this time can be reduced by the usage of cutoff distance, neighbor list, and other acceleration methods, it is still computationally expensive when M is large. For example, a protein usually contains tens of thousands of atoms and to efficiently model a large-scale protein system is still challenging.

A feasible way to increase the computational efficiency is to reduce M, which reduces the degrees of freedom. This is actually the core idea of coarse-grained simulations. For instance, MARTINI force field [144, 145] wraps four heavy atoms into one bead. The higher degree of coarse-graining methods may use one bead to represent hundreds of atoms such that the number of representative beads of a protein is reduced to several hundreds. Methods with an even coarser resolution, which are called *ultra-coarse-grained* (UCG) methods [146, 147, 148], can sometimes represent the whole molecule/object by one or a few beads. The UCG methods require the identification of important metastable states of the molecule. For example, the 2-butene has two important metastable states, *cis-* and *trans-*, and a hairpin peptide has "open" and "close" states. The interaction energy between these states are pre-calculated, which can be assisted by machine learning methods. Each UCG bead is assigned a state and can switch states during simulations.

Via these implementations, the granularity of the model has been greatly reduced. In addition, the particle-wise configuration space is simplified and represented by a few important states. However, important atomistic details could be omitted in the coarse-graining process. Efficient ultra coarse models are often knowledge-based, relying on a priori information to parameterize models thus hindering general predictive capability.

Therefore, CG models with a high granularity that preserves atomistic details are demanded. A powerful numerical method to fast-compute the summation over all the atom pairs is the multipole expansion. In the multipole expansion, the discrete summation is approximated in the continuous form and then expanded into a multipole series. As higher-order terms gradually decay and contribute less, we can properly truncate the infinite series and keep the leading terms. By doing this, we have turned the number of terms in the summation from $\mathcal{O}(M^2)$ to only a few.

In the following of this chapter, we will introduce the multipole expansion method using the spherical harmonics, which is mostly based on the previous works of Baddour [149] and Girard [150], and extend it to complex biological molecule systems. In Section A.1, we show how the interaction between two complex objects can be written as an integral in the continuous representation and can be transformed into multiplication in the Fourier space. In Section A.2, we review the Fourier transform, the spherical harmonic functions, and their connection. In Section A.3, we discuss the numerical implementation of the spherical harmonic expansion method.

A.1. Field representation of pairwise potentials

Consider a system of macromolecules interacting through some particular potentials that we are interested in, for example, a screened Yukawa potential. For molecule i, we denote the position of its center of mass by $\boldsymbol{r}_i$ and its orientation by $\hat{\boldsymbol{R}}_i$. Let $\chi(r)$ be the interaction potential, which is isotropic and hence only relies on the distance between two molecules. In this method, $\chi(r)$ must possess a Fourier transform; otherwise, it has no restriction.

Taking the case of charged particles interacting through a Yukawa potential for an example, we have $\chi(r) = \exp(-\kappa r)/r$. Let $\rho_i(\boldsymbol{r}, \hat{\boldsymbol{R}}_i)$ be the charge density distribution of molecule i in its own reference system (i.e. put $\boldsymbol{r}_i$ on the origin). For a point in the reference system of molecule i, $\boldsymbol{r}$, and a point in the reference system of molecule j, $\boldsymbol{r}'$, their absolute distance is given as

$$(A.1) \qquad (\boldsymbol{r} + \boldsymbol{r}_i) - (\boldsymbol{r}' + \boldsymbol{r}_j) = \boldsymbol{r} - \boldsymbol{r}' - (\boldsymbol{r}_j - \boldsymbol{r}_i) = \boldsymbol{r} - \boldsymbol{r}' - \boldsymbol{r}_{ij},$$

and thus, the interaction potential between molecule i and j can be written as

$$(A.2) \qquad u_{ij}(\boldsymbol{r}_i, \hat{\boldsymbol{R}}_i, \boldsymbol{r}_j, \hat{\boldsymbol{R}}_j) = \iint_{V,V'} \rho_i(\boldsymbol{r}, \hat{\boldsymbol{R}}_i)\chi(|\boldsymbol{r}_{ij} - \boldsymbol{r} - (-\boldsymbol{r}')|)\rho_j(\boldsymbol{r}', \hat{\boldsymbol{R}}_j)\mathrm{d}\boldsymbol{r}\mathrm{d}\boldsymbol{r}'.$$

Notice that if we denote $\underline{\rho}(\boldsymbol{r}) \equiv \rho(-\boldsymbol{r})$, Eqn. (A.2) is in fact the convolution of ρ_i, χ, and $\rho_j{}^*$:

$$(\text{A.3}) \qquad u_{ij}(\boldsymbol{r}_i, \hat{\boldsymbol{R}}_i, \boldsymbol{r}_j, \hat{\boldsymbol{R}}_j) = (\rho_i * * * \chi * * * \underline{\rho_j})(\boldsymbol{r}_{ij}).$$

Here, $* * *$ stands for the convolution operator, which is written as $*$ for short hereafter. In Fourier space, the convolution becomes the multiplication of the Fourier transforms of three functions:

$$(\text{A.4}) \qquad \mathbb{F}\{u_{ij}(\boldsymbol{r}_i, \hat{\boldsymbol{R}}_i, \boldsymbol{r}_j, \hat{\boldsymbol{R}}_j)\} = \mathbb{F}\{\rho_i\}\mathbb{F}\{\chi\}\mathbb{F}\{\underline{\rho_j}\},$$

where $\mathbb{F}\{...\}$ stands for the Fourier transform. Therefore, it is more numerically efficient to compute the interaction potential by first transforming the functions into Fourier space, then calculating the multiplication, and finally transforming back to the real space.

A.2. Properties of three-dimensional Fourier transforms in spherical polar coordinates

A.2.1. Three-dimensional Fourier transform

The three-dimensional (3D) Fourier transform of $f(\boldsymbol{r}) = f(x, y, z)$ is defined as

$$(\text{A.5}) \qquad F(\boldsymbol{\omega}) = \int_V f(\boldsymbol{r}) e^{-i\boldsymbol{\omega}\cdot\boldsymbol{r}} \mathrm{d}\boldsymbol{r}.$$

---

*The convolution of three functions is:
$$(f * g * h)(x) = \iint_{V \times V} f(y)g(z)h(x - y - z)\mathrm{d}y\mathrm{d}z$$

By doing this, the function is converted from the spatial space, $\boldsymbol{r} = (r, \psi_r, \theta_r)$, to the frequency space, $\boldsymbol{\omega} = (\omega, \psi_\omega, \theta_\omega)$. Similarly, the inverse Fourier transform is given as

$$(A.6) \qquad f(\boldsymbol{r}) = \frac{1}{(2\pi)^3} \int_V F(\boldsymbol{\omega}) e^{i\boldsymbol{\omega}\cdot\boldsymbol{r}} \mathrm{d}\boldsymbol{\omega}.$$

The Fourier kernel, $e^{-i\boldsymbol{\omega}\cdot\boldsymbol{r}}$, can be expanded into spherical harmonics as follows:

$$(A.7) \qquad e^{-i\boldsymbol{\omega}\cdot\boldsymbol{r}} = 4\pi \sum_{l=0}^{\infty} \sum_{k=-l}^{k=l} (-i)^l j_l(\omega r) \overline{Y_l^k(\psi_r, \theta_r)} Y_l^k(\psi_\omega, \theta_\omega).$$

Here, Y_l^k are spherical harmonics and j_l is the l-order spherical Bessel function which will be introduced in the later sections. As $\boldsymbol{r}$ and $\boldsymbol{\omega}$ are equivalent in Eqn. (A.7), they are interchangable. Thus, the inverse Fourier kernel can be expanded as:

$$(A.8) \qquad e^{i\boldsymbol{\omega}\cdot\boldsymbol{r}} = 4\pi \sum_{l=0}^{\infty} \sum_{k=-l}^{k=l} (i)^l j_l(\omega r) \overline{Y_l^k(\psi_\omega, \theta_\omega)} Y_l^k(\psi_r, \theta_r).$$

A.2.2. Spherical harmonics

Spherical harmonics are the solution to the angular portion of Laplace's equation:

$$(A.9) \qquad \frac{1}{Y} \frac{1}{\sin\theta} \frac{\partial}{\partial\theta}\left(\sin\theta \frac{\partial Y}{\partial\theta}\right) + \frac{1}{Y} \frac{1}{\sin^2\theta} \frac{\partial^2 Y}{\partial\psi^2} = -l(l+1),$$

and possess the expression

$$(A.10) \qquad Y_l^m(\psi, \theta) = \sqrt{\frac{(2l+1)(l-m)!}{4\pi(l+m)!}} P_l^m(\cos\psi) e^{im\theta}.$$

Here, Y_l^m is called a spherical harmonic function of degree l and order m, P_l^m is an associated Legendre function, $0 \le \psi \le \pi$ represents the colatitude, and $0 \le \theta \le 2\pi$

represents the longitude. The degree $l = 0, 1, 2, ...$ must be a non-negative integer and the order m can be any integer within $[-l, l]$. The orthogonality relationship between spherical harmonics is given by

$$(A.11) \qquad \int_0^{2\pi} \int_0^{\pi} Y_l^m \overline{Y_{l'}^{m'}} \sin \psi \mathrm{d}\psi \mathrm{d}\theta = \delta_{ll'} \delta_{mm'},$$

where δ_{ij} is the Kronecker function and the overbar indicates the complex conjugate.

A.2.3. Bessel functions and spherical Hankel transform

Bessel functions are canonical solutions of Bessel's differential equation

$$(A.12) \qquad x^2 \frac{\mathrm{d}^2 y}{\mathrm{d}x^2} + x \frac{\mathrm{d}y}{\mathrm{d}x} + (x^2 - \alpha^2)y = 0.$$

Bessel functions of the first kind [151], $J_\alpha(x)$, has the expression

$$(A.13) \qquad J_\alpha(x) = \sum_{m=0}^{\infty} \frac{(-1)^m}{m! \Gamma(m + \alpha + 1)} \left(\frac{x}{2}\right)^{2m+\alpha},$$

where Γ is the Gamma function. The spherical Bessel functions are defined from the half-integer order Bessel functions

$$(A.14) \qquad j_n(x) = \sqrt{\frac{\pi}{2x}} J_{n+1/2}(x).$$

The spherical Bessel functions with different orders satisfy an orthogonality relationship.

The spherical Hankel transform of order n can be defined from the nth-order spherical Bessel function as

$$\text{(A.15)} \qquad \hat{F}_n(\omega) = S_n\{f(r)\} = \int_0^\infty f(r) j_n(\omega r) r^2 \mathrm{d}r.$$

The inverse Hankel transform is given by

$$\text{(A.16)} \qquad f(r) = \frac{2}{\pi} \int_0^\infty \hat{F}_n(\omega) j_n(\omega r) \omega^2 \mathrm{d}\omega.$$

Next, we will show how the Hankel transforms and the Fourier transforms are related.

A.2.4. Connection between Fourier transform and spherical harmonics

Because of the orthogonality of spherical harmonics, any well-behaved function can be expanded in terms of spherical harmonics in the following form

$$\text{(A.17)} \qquad f(\boldsymbol{r}) = f(r, \psi_r, \theta_r) = \sum_L f_l^k(r) Y_l^k(\psi_r, \theta_r),$$

where we have used

$$\text{(A.18)} \qquad \sum_L = \sum_{l=0}^\infty \sum_{k=-l}^{k=l}$$

for simplicity. The expansion coefficient is given by

$$\text{(A.19)} \qquad f_l^k(r) = \int_0^{2\pi} \int_0^\pi f(r, \psi_r, \theta_r) \overline{Y_l^k(\psi_r, \theta_r)} r^2 \sin \psi_r \mathrm{d}\psi_r \mathrm{d}\theta_r.$$

Similarly, the Fourier transform of $f(\boldsymbol{r})$ can be expanded into a spherical harmonic series

(A.20) $$F(\boldsymbol{\omega}) = \sum_L F_l^k(\omega) Y_l^k(\psi_\omega, \theta_\omega).$$

Plugging the spherical harmonic expansion of the Fourier kernel, Eqn. (A.7), and the spherical harmonic expansion of $f(\boldsymbol{r})$, Eqn. (A.10), into the Fourier transform equation, Eqn. (A.5), we have

$$
\begin{aligned}
F(\boldsymbol{\omega}) = &\int_0^\infty \mathrm{d}r \int_0^{2\pi} \int_0^\pi \sum_L f_l^k(r) Y_l^k(\psi_r, \theta_r) \\
&\times 4\pi \sum_{L'} (-i)^{l'} j_{l'}(\omega r) \overline{Y_{l'}^{k'}(\psi_r, \theta_r)} Y_{l'}^{k'}(\psi_\omega, \theta_\omega) r^2 \sin\psi_r \mathrm{d}\psi_r \mathrm{d}\theta_r \\
= &\sum_{L'} \sum_L 4\pi(-i)^{l'} \int_0^\infty f_l^k(r) j_{l'}(\omega r) r^2 \mathrm{d}r \\
&\times \int_0^{2\pi} \int_0^\pi Y_l^k(\psi_r, \theta_r) \overline{Y_{l'}^{k'}(\psi_r, \theta_r)} \sin\psi_r \mathrm{d}\psi_r \mathrm{d}\theta_r \times Y_{l'}^{k'}(\psi_\omega, \theta_\omega) \\
= &\sum_{L'} \sum_L 4\pi(-i)^{l'} \int_0^\infty f_l^k(r) j_{l'}(\omega r) r^2 \mathrm{d}r \delta_{ll'} \delta_{kk'} Y_{l'}^{k'}(\psi_\omega, \theta_\omega) \\
= &\sum_L 4\pi(-i)^l \left\{ \int_0^\infty f_l^k(r) j_l(\omega r) r^2 \mathrm{d}r \right\} Y_l^k(\psi_\omega, \theta_\omega).
\end{aligned}
$$

(A.21)

Comparing Eqn. (A.21) to Eqn. (A.20), it is seen that

(A.22) $$F_l^k(\omega) = 4\pi(-i)^l \left\{ \int_0^\infty f_l^k(r) j_l(\omega r) r^2 \mathrm{d}r \right\} = 4\pi(-i)^l S_l\{f_l^k(r)\}.$$

Therefore, the spherical harmonic expansion coefficients of the Fourier transform of a function, $\{F_l^k\}$, are the Hankel transform of the spherical harmonic expansion coefficients

of the original function, $\{f_l^k\}$. In other words, and more importantly, in the representation of spherical harmonic expansion, the Fourier transform can be realized by simply replacing the (l, k)th coefficient of the spherical harmonic series by its l-th order Hankel transform.

For the inverse Fourier transform, following the same derivation, we have

$$
\begin{aligned}
f(\boldsymbol{r}) = & \frac{1}{(2\pi)^3} \int_0^\infty d\omega \int_0^{2\pi} \int_0^\pi \sum_L F_l^k(r) Y_l^k(\psi_\omega, \theta_\omega) \\
& \times 4\pi \sum_{L'} (i)^{l'} j_{l'}(\omega r) \overline{Y_{l'}^{k'}(\psi_\omega, \theta_\omega)} Y_{l'}^{k'}(\psi_r, \theta_r) \omega^2 \sin\psi_\omega d\psi_\omega d\theta_\omega \\
= & \sum_{L'} \sum_L \frac{(i)^{l'}}{2\pi^2} \int_0^\infty F_l^k(r) j_{l'}(\omega r) \omega^2 dr \delta_{ll'} \delta_{kk'} Y_{l'}^{k'}(\psi_r, \theta_r) \\
= & \sum_L \frac{(i)^l}{4\pi} \left\{ \frac{2}{\pi} \int_0^\infty F_l^k(r) j_l(\omega r) \omega^2 d\omega \right\} Y_l^k(\psi_r, \theta_r),
\end{aligned}
$$

(A.23)

which gives

(A.24)
$$
f_l^k(r) = \frac{(i)^{l'}}{4\pi} S_l\{F_l^k(r)\}.
$$

A more straightforward way to obtain the above equation is to do the inverse Hankel transform of Eqn. (A.22).

A.2.5. Multiplication and Slater coefficients

Next, we discuss the multiplication between functions. Consider two functions, $f(\boldsymbol{r})$ and $g(\boldsymbol{r})$, where $f(\boldsymbol{r}) = \sum_L f_l^k(r) Y_l^k$ and similarly for g. Their product, $h(\boldsymbol{r}) = f(\boldsymbol{r})g(\boldsymbol{r})$, can be also expanded into a spherical harmonic series, $h(\boldsymbol{r}) = \sum_L h_l^k(r) Y_l^k$. We aim to find out how h_l^k relates to f_l^k and g_l^k. This can be accomplished by transforming $h(\boldsymbol{r})$ into the

Fourier space:

$$H(\boldsymbol{\omega}) = \int_V f(\boldsymbol{r})g(\boldsymbol{r})e^{-i\boldsymbol{\omega}\cdot\boldsymbol{r}}\mathrm{d}\boldsymbol{r}$$

$$(A.25) \qquad = \int_0^\infty \int_0^{2\pi} \int_0^\pi \sum_{L'} f_{l'}^{k'}(r)Y_{l'}^{k'}(\psi_r,\theta_r) \sum_{L''} g_{l''}^{k''}(r)Y_{l''}^{k''}(\psi_r,\theta_r)$$

$$\times 4\pi \sum_L (-i)^l j_l(\omega r)\overline{Y_l^k(\psi_r,\theta_r)}Y_l^k(\psi_\omega,\theta_\omega)r^2 \sin\psi_r \mathrm{d}r\mathrm{d}\psi_r\mathrm{d}\theta_r,$$

where the angular part (ψ_r,θ_r) is the integral:

$$(A.26) \qquad \int_0^{2\pi} \int_0^\pi Y_{l'}^{k'}(\psi_r,\theta_r)Y_{l''}^{k''}(\psi_r,\theta_r)\overline{Y_l^k(\psi_r,\theta_r)} \sin\psi_r\mathrm{d}\psi_r\mathrm{d}\theta_r.$$

The expression of spherical harmonics, Eqn. (A.10), allows a further separation of the angular variables, which results in an integral:

$$(A.27) \qquad \int_0^{2\pi} e^{i(k'+k''-k)\theta_r}\mathrm{d}\theta_r = \delta(k'+k''-k).$$

Therefore, we can replace k'' by $k-k'$. Actually, the integrals in Eqn. (A.26) are known as *Slater coefficients* which are defined as

$$(A.28) \qquad c^{l''}(l,k,l',k') \equiv \int_0^{2\pi} \int_0^\pi Y_{l'}^{k'}(\psi_r,\theta_r)Y_{l''}^{k-k'}(\psi_r,\theta_r)\overline{Y_l^k(\psi_r,\theta_r)} \sin\psi_r\mathrm{d}\psi_r\mathrm{d}\theta_r$$

and are nonzero only for $|l-l'| \leq l'' \leq l+l'$. Using Slater coefficients, Eqn. (A.25) becomes

(A.29)

$$H(\boldsymbol{\omega}) = \sum_L 4\pi(-i)^l \left\{ \int_0^\infty \sum_{L'} f_{l'}^{k'}(r) \sum_{l''=|l-l'|}^{l+l'} g_{l''}^{k-k'}(r)c^{l''}(l,k,l',k')j_l(\omega r)r^2\mathrm{d}r \right\} Y_l^k(\psi_\omega,\theta_\omega).$$

As shown by Eqn. (A.21) that

(A.30)
$$H(\boldsymbol{\omega}) = \sum_L 4\pi(-i)^l \left\{ \int_0^\infty h_l^k(r) j_l(\omega r) r^2 \mathrm{d}r \right\} Y_l^k(\psi_\omega, \theta_\omega),$$

we obtain

(A.31)
$$h_l^k(r) = \sum_{L'} f_{l'}^{k'}(r) \sum_{l''=|l-l'|}^{l+l'} c^{l''}(l, k, l', k') g_{l''}^{k-k'}(r).$$

As Slater coefficients are precomputed and tabulated, it is convenient for us to use the existing table of Slater coefficients in our computation.

A.2.6. Spatial shift

The spatial shift of a function $f(\boldsymbol{r})$ respect to a reference point $\boldsymbol{r}_0$, which is written as $f(\boldsymbol{r} - \boldsymbol{r}_0)$, possesses a Fourier transform

(A.32)
$$\begin{aligned}
\mathbb{F}\{f(\boldsymbol{r} - \boldsymbol{r}_0)\} &= \int_V f(\boldsymbol{r} - \boldsymbol{r}_0) e^{-i\boldsymbol{\omega}\cdot\boldsymbol{r}} \mathrm{d}\boldsymbol{r}. \\
&= e^{-i\boldsymbol{\omega}\cdot\boldsymbol{r}_0} \int_V f(\boldsymbol{r} - \boldsymbol{r}_0) e^{-i\boldsymbol{\omega}\cdot(\boldsymbol{r}-\boldsymbol{r}_0)} \mathrm{d}(\boldsymbol{r} - \boldsymbol{r}_0) \\
&= e^{-i\boldsymbol{\omega}\cdot\boldsymbol{r}_0} \mathbb{F}\{f(\boldsymbol{r})\}.
\end{aligned}$$

Thus, the spatially shifted function can be defined as

(A.33)
$$f(\boldsymbol{r} - \boldsymbol{r}_0) = \mathbb{F}^{-1}\{e^{-i\boldsymbol{\omega}\cdot\boldsymbol{r}_0} F(\boldsymbol{\omega})\}.$$

Using the spherical harmonic series of $F(\boldsymbol{\omega})$ (Eqn. (A.21)), $e^{-i\boldsymbol{\omega}\cdot\boldsymbol{r}_0}$ (Eqn. (A.7) with r replaced by r_0), and $e^{i\boldsymbol{\omega}\cdot\boldsymbol{r}}$ (Eqn. (A.8)), Eqn. (A.33) becomes

(A.34)

$$
\begin{aligned}
f(\boldsymbol{r}-\boldsymbol{r}_0) =& \frac{1}{(2\pi)^3} \int_0^\infty \int_0^{2\pi} \int_0^\pi \sum_{L''} 4\pi(-i)^{l''} \left\{ \int_0^\infty f_{l''}^{k''}(u) j_{l''}(\omega u) u^2 \mathrm{d}u \right\} Y_{l''}^{k''}(\psi_\omega, \theta_\omega) \\
&\times 4\pi \sum_{L'}(-i)^{l'} j_{l'}(\omega r_0) \overline{Y_{l'}^{k'}(\psi_{r_0}, \theta_{r_0})} Y_{l'}^{k'}(\psi_\omega, \theta_\omega) \\
&\times 4\pi \sum_{L}(i)^{l} j_{l}(\omega r) \overline{Y_l^k(\psi_\omega, \theta_\omega)} Y_l^k(\psi_r, \theta_r) \omega^2 \sin\psi_\omega \mathrm{d}\omega \mathrm{d}\psi_\omega \mathrm{d}\theta_\omega.
\end{aligned}
$$

The integral above can be separated into the angular part $(\psi_\omega, \theta_\omega)$ and the radial part ω. The angular part yields the aforementioned Slater coefficients. The radial part featuring the integral of a triple product of spherical Bessel functions can be called *the shift operator*, which is defined as

(A.35)
$$
S_{l''}^{l,l'}(u, r, r_0) = \int_0^\infty j_{l''}(\omega u) j_{l'}(\omega r_0) j_l(\omega r) \omega^2 \mathrm{d}\omega.
$$

Hence, the spatially shifted function becomes

(A.36)
$$
\begin{aligned}
f(\boldsymbol{r}-\boldsymbol{r}_0) =& \sum_{L} 8(i)^{l} Y_l^k(\psi_r, \theta_r) \sum_{L'}(-i)^{l'} \overline{Y_{l'}^{k'}(\psi_{r_0}, \theta_{r_0})} \\
&\times \sum_{l''=|l-l'|}^{l+l'} (-i)^{l''} c^{l''}(l, k, l', k') \int_0^\infty f_{l''}^{k-k'}(u) S_{l''}^{l,l'}(u, r, r_0) u^2 \mathrm{d}u.
\end{aligned}
$$

The properties of the shift operator are quite complicated and will not be discussed here. With the shift operator, the calculation of convolution seems to be very cumbersome. Next, however, we will show when transforming the convolution into the Fourier space,

the shift operator disappears and the result only includes the spherical harmonic expansion coefficients of the Fourier transform of each function.

A.2.7. Convolution

The 3D convolution of two functions is defined as

$$(A.37) \qquad h(\boldsymbol{r}) = f(\boldsymbol{r}) * g(\boldsymbol{r}) = \int_V g(\boldsymbol{r}_0) f(\boldsymbol{r} - \boldsymbol{r}_0) \mathrm{d}\boldsymbol{r}_0.$$

Here, we use the spherical harmonic expansion to prove the below relationship:

$$(A.38) \qquad H(\boldsymbol{\omega}) = F(\boldsymbol{\omega}) G(\boldsymbol{\omega}).$$

By plugging the spherical harmonic series of $g(\boldsymbol{r}_0)$ and $f(\boldsymbol{r} - \boldsymbol{r}_0)$ into Eqn. (A.37), it becomes

$$
\begin{aligned}
h(\boldsymbol{r}) = & \int_0^\infty \int_0^{2\pi} \int_0^\pi \sum_{L'''} g_{l'''}^{k'''}(r_0) Y_{l'''}^{k'''}(\psi_{r_0}, \theta_{r_0}) \sum_L 8(i)^l Y_l^k(\psi_r, \theta_r) \\
& \times \sum_{L'} (-i)^{l'} \overline{Y_{l'}^{k'}(\psi_{r_0}, \theta_{r_0})} \sum_{l''=|l-l'|}^{l+l'} (-i)^{l''} c^{l''}(l, k, l', k') \\
& \times \int_0^\infty f_{l''}^{k-k'}(u) \int_0^\infty j_{l''}(\omega u) j_{l'}(\omega r_0) j_l(\omega r) \omega^2 \mathrm{d}\omega u^2 \mathrm{d}u r_0^2 \sin\psi_{r_0} \mathrm{d}\psi_{r_0} \mathrm{d}\theta_{r_0} \mathrm{d}r_0.
\end{aligned}
$$
(A.39)

The integral of the angular variables $(\psi_{r_0}, \theta_{r_0})$ is

$$(A.40) \qquad \int_0^{2\pi} \int_0^\pi Y_{l'''}^{k'''}(\psi_{r_0}, \theta_{r_0}) \overline{Y_{l'}^{k'}(\psi_{r_0}, \theta_{r_0})} \sin\psi_{r_0} \mathrm{d}\psi_{r_0} \mathrm{d}\theta_{r_0} = \delta_{l' l'''} \delta_{k' k'''}.$$

Thus, Eqn. (A.39) can be simplified as

(A.41)
$$
h(\boldsymbol{r}) = \int_0^\infty \sum_L 8(i)^l Y_l^k(\psi_r, \theta_r) \sum_{L'} (-i)^{l'} g_{l'}^{k'}(r_0) \sum_{l''=|l-l'|}^{l+l'} (-i)^{l''} c^{l''}(l, k, l', k')
$$
$$
\times \int_0^\infty f_{l''}^{k-k'}(u) \int_0^\infty j_{l''}(\omega u) j_{l'}(\omega r_0) j_l(\omega r) \omega^2 d\omega u^2 du r_0^2 dr_0.
$$

Comparing Eqn. (A.41) to the Fourier transform of $h(\boldsymbol{r})$:

(A.42)
$$
h(\boldsymbol{r}) = \sum_L \frac{(i)^l}{4\pi} \left\{ \frac{2}{\pi} \int_0^\infty H_l^k(r) j_l(\omega r) \omega^2 d\omega \right\} Y_l^k(\psi_r, \theta_r),
$$

we have

(A.43)
$$
H_l^k(r) = \int_0^\infty (4\pi)^2 \sum_{L'} (-i)^{l'} g_{l'}^k(r_0) \sum_{l''=|l-l'|}^{l+l'} (-i)^{l''} c^{l''}(l, k, l', k')
$$
$$
\times \int_0^\infty f_{l''}^{k-k'}(u) j_{l''}(\omega u) j_{l'}(\omega r_0) u^2 du r_0^2 dr_0
$$
$$
= \sum_{L'} \sum_{l''=|l-l'|}^{l+l'} c^{l''}(l, k, l', k') \left\{ \int_0^\infty 4\pi (-i)^{l'} g_{l'}^k(r_0) j_{l'}(\omega r_0) r_0^2 dr_0 \right\}
$$
$$
\times \left\{ 4\pi (-i)^{l''} \int_0^\infty f_{l''}^{k-k'}(u) j_{l''}(\omega u) u^2 du \right\}
$$
$$
= \sum_{L'} \sum_{l''=|l-l'|}^{l+l'} c^{l''}(l, k, l', k') G_{l'}^k(\omega) F_{l''}^{k-k'}(\omega).
$$

Note that the final equation in Eqn. (A.43) implies that $H(\boldsymbol{\omega})$ is the product of $F(\boldsymbol{\omega})$ and $G(\boldsymbol{\omega})$. Therefore, we have proven Eqn. (A.38).

A.2.8. Quaternions and spatial rotation

Now, we start to discuss the rotation of the object, as the object in any orientation can be obtained via a rotation from the reference orientation. In our method, we use *quaternions* to describe rotation. Quaternions are generally represented in the form

$$(A.44) \qquad \boldsymbol{q} = q_w + q_x \boldsymbol{i} + q_y \boldsymbol{j} + q_z \boldsymbol{k},$$

where q_w, q_x, q_y, and q_z are real numbers; and 1, $\boldsymbol{i}$, $\boldsymbol{j}$, and $\boldsymbol{k}$ are the basis vectors or basis elements. In traditional Cartesian coordinates, the basis vectors are simply $\hat{\boldsymbol{x}}$, $\hat{\boldsymbol{y}}$, and $\hat{\boldsymbol{z}}$. Hereafter, the quaternions discussed are all in the Cartesian coordinates and are normalized, which means their norms are $\sqrt{q_w^2 + q_x^2 + q_y^2 + q_z^2} = 1$.

Quaternions can be viewed as an extension of the two-dimensional complex plane to the 3D space. Therefore, we refer to q_w as the real part and $q_x \boldsymbol{i} + q_y \boldsymbol{j} + q_z \boldsymbol{k}$ as the imaginary part. Similar to the imaginary axis in the complex plane, for quaternions we have

$$(A.45) \qquad \boldsymbol{i}^2 = \boldsymbol{j}^2 = \boldsymbol{k}^2 = -1.$$

Also, we have

$$(A.46) \qquad \boldsymbol{ij} = \boldsymbol{k}; \ \boldsymbol{jk} = \boldsymbol{i}; \ \boldsymbol{ki} = \boldsymbol{j},$$

as rotating the y-axis about the x-axis by 90° yields the z-axis in the right-handed coordinate system; similarly for other equations.

Given any two orientations, we denote their z-axes as $\boldsymbol{z}_1$ and $\boldsymbol{z}_2$, respectively. Let $\boldsymbol{u} = \boldsymbol{z}_1 \times \boldsymbol{z}_2$ and $\phi = \arccos[\boldsymbol{z}_1 \cdot \boldsymbol{z}_2 / (|\boldsymbol{z}_1||\boldsymbol{z}_2|)]$, where $\times$ and $\cdot$ are the cross product and the

dot product between vectors, respectively. Then, z_1-orientation can be transformed to z_2-orientation by rotating z_1-orientation about u by ϕ. In the representation of quaternions, this rotation is written as

$$(A.47) \qquad\qquad q^{-1} z_1 q = z_2,$$

where q^{-1} is the inverse of q. For unit quaternions, q^{-1} is the conjugate of q:

$$(A.48) \qquad\qquad q^{-1} = q_w - (q_x i + q_y j + q_z k).$$

It is proven [152] that

$$(A.49) \qquad\qquad q = e^{i\frac{\phi}{2}(u_x i + u_y j + u_z k)} = \cos\frac{\phi}{2} + \sin\frac{\phi}{2}(u_x i + u_y j + u_z k).$$

Therefore, to briefly summarize how to use quaternions to represent 3D rotations, we first determine the rotation axis u and the rotation angle ϕ, then find the corresponding quaternion via Eqn. (A.49), and obtain the coordinate of rotated object via Eqn. (A.47).

A.2.9. Rotation formulas for spherical harmonics and Wigner D-Matrix

A 3D rotation operator is defined as

$$(A.50) \qquad\qquad \hat{\mathcal{R}}(\alpha, \beta, \gamma) = e^{i\alpha\hat{z}} e^{i\beta\hat{y}} e^{i\gamma\hat{z}},$$

where α, β, γ are Euler angles. The rotation operator can be understood as first rotating about the z-axis by an angle γ, then rotating about the y-axis by β, and finally rotating about the z-axis by α.

Each spherical harmonic function is rotated when the rotation operator is exerted on a function expanded into spherical harmonics. These rotated spherical harmonics can be expanded again into spherical harmonics given by the following rotation formula:

$$(A.51) \qquad \hat{\mathcal{R}}(\alpha, \beta, \gamma)Y_l^m(\psi, \theta) = \sum_{m'=-l}^{l} D_{mm'}^l(\alpha, \beta, \gamma)Y_l^{m'}(\psi, \theta).$$

Here, $D_{mm'}^l(\alpha, \beta, \gamma)$ is called *Wigner D-matrix* and defined as

$$(A.52) \qquad D_{mm'}^l(\alpha, \beta, \gamma) = e^{im\alpha} d_{mm'}^l(\beta) e^{im'\gamma},$$

where the rotations about the z-axis in the spherical polar coordinates are simply $e^{im\alpha}$ and $e^{im\gamma}$. The *Wigner's small d-matrix*, $d_{mm'}^l(\beta)$, is defined as

$$(A.53) \qquad \begin{aligned} d_{mm'}^l(\beta) = &\sqrt{(l+m)!(l-m)!(l+m')!(l-m')!} \\ &\times \sum_{s=s_{min}}^{s_{max}} \frac{(-1)^{m-m'+s}\left(\cos\frac{\beta}{2}\right)^{2l+m'-m-2s}\left(\sin\frac{\beta}{2}\right)^{m-m'+2s}}{(l+m'-s)!(l-m-s)!(m-m'+s)!}, \end{aligned}$$

where the range of s covers the values which make the factorials non-negative, i.e., $s_{min} = \max(0, m'-m)$ and $s_{max} = \min(l+m', l-m)$.

In the quaternion representation of rotations, $D_{mm'}^l(\alpha, \beta, \gamma)$ is given as [153]:

$$(A.54)$$
$$D_{mm'} = \sqrt{\frac{(l+m)!(l-m)!}{(l+m')!(l-m')!}}|R_a|^{2l-2m}R_a^{m+m'}R_b^{m-m'}\sum_s(-1)^s\binom{s}{l+m'}\binom{l-s-m}{l-m'}\left(\frac{|R_a|}{|R_b|}\right)^{2s},$$

where $R_a = q_w + iq_z$ and $R_b = q_y + iq_x$; the range of s is the same as the one mentioned above. Using quaternions, it is more convenient for us to deal with the rotations without evaluating trigonometric functions.

A.3. Numerical implementation

With all the aforementioned mathematical tools, we can revisit Eqn. (A.2). We start by evaluating each term on the r.h.s. of Eqn. (A.4), which all are required to possess a Fourier transform. We also require that the object is rigid so that the spherical harmonics are time-invariant.

A.3.1. Density function

A convenient choice of the continuous density function is the Gaussian function. The density function of an atom located at $\boldsymbol{r}_0$ can be written as a Gaussian function shifted in space:

$$(A.55) \qquad f(\boldsymbol{r} - \boldsymbol{r}_0) = \left(\frac{1}{\sqrt{2\pi}\sigma} \right)^3 \exp \left[-\frac{(\boldsymbol{r} - \boldsymbol{r}_0)^2}{2\sigma^2} \right].$$

Here, σ is the width of the Gaussian function and is a tunable parameter. In practice, σ should depend on the radius of the atom.

Note that the 3D Fourier transform of a Gaussian function is given by

$$(A.56) \qquad \mathbb{F}\{f(\boldsymbol{r})\} = F(\boldsymbol{\omega}) = \int d\boldsymbol{r} \left(\frac{1}{\sqrt{2\pi}\sigma} \right)^3 e^{-\frac{\boldsymbol{r}^2}{2\sigma^2}} e^{-i\boldsymbol{\omega} \cdot \boldsymbol{r}} = e^{-\frac{\omega^2 \sigma^2}{2}}.$$

Since $Y_0^0 = 1/\sqrt{4\pi}$ is the only constant term and the only spherically symmetric term, the spherical harmonic expansion of $F(\boldsymbol{\omega})$ contains only the first term:

$$(A.57) \qquad F(\boldsymbol{\omega}) = \sqrt{4\pi} e^{-\frac{\omega^2 \sigma^2}{2}} Y_0^0(\psi_\omega, \theta_\omega).$$

Thus, the Fourier transform of the shifted Gaussian function can be expanded into spherical harmonics as

$$(A.58) \quad \mathbb{F}\{f(\boldsymbol{r} - \boldsymbol{r}_0)\} = e^{-i\boldsymbol{\omega}\cdot\boldsymbol{r}_0}F(\boldsymbol{\omega}) = \sum_{L}\left\{4\pi(-i)^l j_l(\omega r)\overline{Y_l^k(\psi_{r_0}, \theta_{r_0})}e^{-\frac{\omega^2\sigma^2}{2}}\right\}Y_l^k(\psi_\omega, \theta_\omega),$$

where inside the bracket $\{...\}$ are the expansion coefficients.

For an object with an orientation $\hat{R}_1$, its density function in the reciprocal space is given by the sum of density functions of all its atoms

(A.59)

$$\tilde{\rho}(\boldsymbol{\omega}, \hat{R}_1) = \sum_{L}\left\{\sum_{j}4\pi(-i)^l j_l(\omega r)\overline{Y_l^k(\psi_{r_{1,j}}, \theta_{r_{1,j}})}e^{-\frac{\omega^2\sigma_{1,j}^2}{2}}\right\}\sum_{m'=-l}^{l}D_{kk'}^l(\hat{R}_1)Y_l^k(\psi_\omega, \theta_\omega)$$

$$= \sum_{L}\sum_{k'=-l}^{l}D_{kk'}^l(\hat{R}_1)F_l^k(\omega)Y_l^k(\psi_\omega, \theta_\omega).$$

Here, $\tilde{\rho}$ represents the Fourier transform of ρ; the subscript j goes through all the atoms in the object; and $\sigma_{1,j}$ and $\boldsymbol{r}_{1,j}$ are the Gaussian function width parameter and the atom position in the referential frame of the object, respectively. The expansion coefficients, $F_l^k(\omega)$, can be precalculated from the atomic information and saved for later simulations.

For the geometrically inversed density function, $\underline{\rho}(\boldsymbol{r}) = \rho(-\boldsymbol{r})$, its Fourier transform is

$$(A.60) \qquad \underline{\tilde{\rho}}(\boldsymbol{\omega}) = \int_{-\infty}^{\infty}\rho(-\boldsymbol{r})e^{-i\boldsymbol{\omega}\cdot\boldsymbol{r}}\mathrm{d}\boldsymbol{r} = -\int_{\infty}^{-\infty}\rho(\boldsymbol{r}')e^{-i(-\boldsymbol{\omega})\cdot\boldsymbol{r}'}\mathrm{d}\boldsymbol{r}' = \tilde{\rho}(-\boldsymbol{\omega}),$$

where we have changed the variable by $r' = -r$. Since $-\boldsymbol{\omega} = (\omega, \pi - \psi_\omega, \pi + \theta_\omega)$, the spherical harmonics become

$$Y_l^k(\pi - \psi_\omega, \pi + \theta_\omega) \sim P_l^k(\cos(\pi - \psi_\omega))e^{ik(\pi+\theta_\omega)}$$

(A.61)
$$= P_l^k(-\cos\psi_\omega)(-1)^k e^{ik\theta_\omega}$$

$$= (-1)^{l+k} P_l^k(\cos\psi_\omega)(-1)^k e^{ik\theta_\omega},$$

where the third equation comes from the parity $P_l^k(x) = (-1)^{l+k} P_l^k(x)$. Therefore, we have

(A.62)
$$\tilde{\underline{\rho}}(\boldsymbol{\omega}, \hat{R}_1) = \sum_L \sum_{k'=-l}^{l} (-1)^l D_{kk'}^l(\hat{R}_1) F_l^k(\omega) Y_l^k(\psi_\omega, \theta_\omega).$$

When considering other density functions, such as the charge density function, we simply multiply the density of each atom by its charge or partial charge as the weighting factor.

A.3.2. Interaction potentials

A.3.2.1. Hardcore repulsion. The hardcore repulsion, or the volume excluding effect, between two objects is considered by setting $\chi(\boldsymbol{r}) = \delta(\boldsymbol{r})$, whose Fourier transform is 1. Thus, the only non-zero spherical harmonic expansion coefficient is $G_0^0(\omega) = \sqrt{4\pi}$.

A.3.2.2. Yukawa potential. The $1/r$ Coulomb potential does not have a Fourier transform and thus cannot be used in our method. However, when salt exists in the solution, the electrostatic interaction can be described by a screened Yukawa potential,

$\chi(r) = \exp(-\kappa r)/r$, which possesses a Fourier transform as

$$
\begin{aligned}
\mathbb{F}\{\chi(\boldsymbol{\omega})\} &= \int \mathrm{d}\boldsymbol{r} \frac{e^{-\kappa r}}{r} e^{-i\boldsymbol{\omega}\cdot\boldsymbol{r}} \\
&= \int_0^\infty \int_0^{2\pi} \int_0^\pi r e^{-\kappa r} e^{-i\omega r \cos\theta} \sin\theta \mathrm{d}\theta \mathrm{d}\psi \\
&= 2\pi \int_0^\infty r e^{-\kappa r} \left(\frac{e^{-i\omega r}}{-i\omega r} - \frac{e^{i\omega r}}{-i\omega r} \right) \mathrm{d}r \\
&= \frac{4\pi}{\kappa^2 + \omega^2}.
\end{aligned}
$$

(A.63)

Similarly, the only non-zero spherical harmonic expansion coefficient is

$$
G_0^0(\omega) = \sqrt{4\pi} \frac{4\pi}{\kappa^2 + \omega^2} = \frac{8\pi^{3/2}}{\kappa^2 + \omega^2}
$$

(A.64)

A.3.2.3. Other interactions. Other interactions existing in macromolecule systems, such as interactions between hydrophilic and hydrophobic domains, can be approximately simulated as coarse-grained potentials. Without losing generality, we can use a simple Gaussian function to describe these interactions:

$$
\chi(r) = \pm a \exp(-br^2),
$$

(A.65)

where $+$ is for the repulsion, $-$ is for the attraction, and a and b respectively represent the interaction strength and the interaction range. Same as the density function, $\chi(r)$ has a Fourier transform:

$$
\mathbb{F}\{\chi(\boldsymbol{\omega})\} = \pm a \left(\frac{\pi}{b} \right)^{3/2} e^{-\frac{\omega^2}{4b}}
$$

(A.66)

and possesses the only non-zero term in its spherical harmonic series

$$(A.67) \qquad \mathbb{F}\{\chi(\boldsymbol{\omega})\} = \pm\sqrt{4\pi}a\left(\frac{\pi}{b}\right)^{3/2}e^{-\frac{\omega^2}{4b}}Y_0^0.$$

A.3.3. Full expression of the potential function

We can construct the full expression of the potential function using the spherical harmonic expansion coefficients discussed above. We first calculate the product $H(\boldsymbol{\omega}) = \mathbb{F}\{\chi\}\mathbb{F}\{\underline{\rho_j}\}$. As discussed above, most of the interaction potentials have spherical symmetry and hence only possess the leading constant term in their spherical harmonic expansion. Thus, the expansion coefficients of the product are given as

$$
\begin{aligned}
H_l^k(\omega, \hat{R}_j) &= \sum_{L'} \sum_{l''=|l-l'|}^{l+l'} c^{l''}(l,k,l',k') G_{l'}^{k'}(\omega) \sum_{\mu_j=-l''}^{l''} D_{k-k',\mu_j}^{l''}(\hat{R}_j)(\underline{F_j})_{l''}^{k-k'}(\omega) \\
(A.68) &= G_0^0(\omega) \sum_{l''=|l|}^{l} c^{l''}(l,k,0,0) \sum_{\mu_j=-l''}^{l''} D_{k-k',\mu_j}^{l''}(\hat{R}_j)(\underline{F_j})_{l''}^{k-k'}(\omega) \\
&= (-1)^l \tilde{\chi}(\omega) \sum_{\mu_j=-l}^{l} D_{k\mu_j}^l(\hat{R}_j)(F_j)_l^k(\omega),
\end{aligned}
$$

where we have used $c^l(l,k,0,0) = 1/\sqrt{4\pi}$. Then, we convolute the result with ρ_i and obtain

$$
\begin{aligned}
\tilde{u}_l^k(\omega, \hat{R}_i, \hat{R}_j) &= \tilde{\chi}(\omega) \sum_{L'} \sum_{l''=|l-l'|}^{l+l'} (-1)^{l''} c^{l''}(l,k,l',k') \\
(A.69) &\qquad \times \sum_{\mu_i=-l'}^{l'} D_{k'\mu_i}^{l'}(\hat{R}_i)(F_i)_{l'}^{k'}(\omega) \sum_{\mu_j=-l''}^{l''} D_{k''\mu_j}^{l''}(\hat{R}_j)(F_j)_{l''}^{k-k'}(\omega).
\end{aligned}
$$

Transforming $\tilde{u}$ back to the real space yields $u(\boldsymbol{r}_{ij}, \hat{R}_i, \hat{R}_j)$:

$$
u(\boldsymbol{r}_{ij}, \hat{R}_i, \hat{R}_j) = \sum_L \sum_{L'} \sum_{l''=|l-l'|}^{l+l'} \frac{(i)^l}{2\pi^2} \left\{ \int_0^\infty \tilde{u}_l^k(\omega, \hat{R}_i, \hat{R}_j) j_l(\omega r) \omega^2 \mathrm{d}\omega \right\} Y_l^k(\psi_r, \theta_r)
$$

$$
= \sum_L \sum_{L'} \sum_{l''=|l-l'|}^{l+l'} \sum_{\mu_i=-l'}^{l'} \sum_{\mu_j=-l''}^{l''} \frac{(i)^l(-1)^{l''}}{2\pi^2}
$$

(A.70)

$$
\times \left\{ \int_0^\infty \tilde{\chi}(\omega)(F_i)_{l'}^{k'}(\omega)(F_j)_{l''}^{k-k'}(\omega) j_l(\omega r) \omega^2 \mathrm{d}\omega \right\}
$$

$$
\times c^{l''}(l, k, l', k') D^{l'}_{k'\mu_i}(\hat{R}_i) D^{l''}_{k''\mu_j}(\hat{R}_j) Y_l^k(\psi_{ij}, \theta_{ij})
$$

with the real space vector $\boldsymbol{r}_{ij} = (r_{ij}, \psi_{ij}, \theta_{ij})$. For the sake of simplicity and clearance, we rewrite the indexes as $k - k' = k''$ such that $k = k' + k''$. Also, we have $|l' - l''| \le l \le l' + l''$, since l, l', and l'' must form a triangle. All the indexes related to the ith object, those with a superscript $'$, are rewritten with a subscript i. All the indexes related to the jth object, those with a superscript $''$, are rewritten with a subscript j. Eqn. (A.70) then becomes

$$
u(\boldsymbol{r}_{ij}, \hat{R}_i, \hat{R}_j) = \sum_{L_i} \sum_{L_j} \sum_{l=|l_i-l_j|}^{l_i+l_j} \sum_{\mu_i=-l_j}^{l_i} \sum_{\mu_j=-l_j}^{l_j} \frac{(i)^l(-1)^{l_j}}{2\pi^2}
$$

(A.71)

$$
\times \left\{ \int_0^\infty \tilde{\chi}(\omega)(F_i)_{l_i}^{k_i}(\omega)(F_j)_{l_j}^{k_j}(\omega) j_l(\omega r) \omega^2 \mathrm{d}\omega \right\}
$$

$$
\times c^{l_j}(l, k_i + k_j, l_i, k_i) D^{l_i}_{k_i\mu_i}(\hat{R}_i) D^{l_j}_{k_j\mu_j}(\hat{R}_j) Y_l^{k_i+k_j}(\psi_r, \theta_r) \Big|_{r=r_{ij}}.
$$

For a macromolecule system consisting of diverse interactions, for example, hardcore repulsion, Yukawa-type electrostatic interaction, and non-directional polar-polar attraction, the total expansion coefficient is given by

$$
\begin{aligned}
F_{l_i,l_j}^{k_i,k_j}(\omega) =& F_{l_i,k_i}^{atom}(\omega) F_{l_j,k_j}^{atom}(\omega) + \frac{4\pi}{\kappa^2 + \omega^2} F_{l_i,k_i}^{charge}(\omega) F_{l_j,k_j}^{charge}(\omega) \\
& - a\left(\frac{\pi}{b}\right)^{3/2} e^{-\frac{\omega^2}{4b}} F_{l_i,k_i}^{polar}(\omega) F_{l_j,k_j}^{polar}(\omega) + ...,
\end{aligned}
$$
(A.72)

where $F_{l,k}^{atom}(\omega)$, $F_{l,k}^{charge}(\omega)$, and $F_{l,k}^{polar}(\omega)$ are the (l,k)th expansion coefficients of the atomic density function, the charge density function, and the polar strength function. The full expression of the potentia function is given as

(A.73)
$$
u(\boldsymbol{r}_{ij}, \hat{R}_i, \hat{R}_j) = \sum_{\substack{l_i,k_i,\mu_i \\ l_i,k_i,\mu_i,l}} \frac{(i)^l(-1)^{l_j}}{2\pi^2} \mathcal{F}_{l,l_i,l_j}^{k_i,k_j}(r_{ij}) \mathcal{C}_{l,l_i,l_j}^{k_i,k_j} D_{k_i\mu_i}^{l_i}(\hat{R}_i) D_{k_j\mu_j}^{l_j}(\hat{R}_j) Y_l^{k_i+k_j}(\psi_r, \theta_r) \bigg|_{r=r_{ij}},
$$

where

(A.74)
$$
\sum_{\substack{l_i,k_i,\mu_i \\ l_i,k_i,\mu_i,l}} = \sum_{l_i=0}^{\infty} \sum_{k_i=-l_i}^{l_i} \sum_{l_j=0}^{\infty} \sum_{k_j=-l_j}^{l_j} \sum_{l=|l_i-l_j|}^{l_i+l_j} \sum_{\mu_i=-l_j}^{l_i} \sum_{\mu_j=-l_j}^{l_j},
$$

and

(A.75)
$$
\mathcal{C}_{l,l_i,l_j}^{k_i,k_j} = c^{l_j}(l, k_i + k_j, l_i, k_i),
$$

and

(A.76)
$$
\mathcal{F}_{l,l_i,l_j}^{k_i,k_j}(r_{ij}) = \int_0^{\infty} F_{l_i,l_j}^{k_i,k_j}(\omega) j_l(\omega r) \omega^2 \mathrm{d}\omega.
$$

In the numerical implementation, we first precalculate the reciprocal density function of each object via Eqn. (A.58) to obtain the expansion coefficients. For objects of the same type, we only need to calculate the density function once. Then, we numerically calculate $F_{l_i,l_j}^{k_i,k_j}(\omega)$ and its Hankel transforms $\mathcal{F}_{l,l_i,l_j}^{k_i,k_j}(r_{ij})$, which is complied into tables up to some cutoff order beforehand. Since $\mathcal{C}_{l,l_i,l_j}^{k_i,k_j}$ can be pre-tabulated as well, the only quantities needed to be computed in every step are $\{D_{k\mu}^l(\hat{R})\}$ given by Eqn. (A.54). The potential is computed via Eqn. (A.73) up to the cutoff order. For example, cutting off at $l_i, l_j = 3$ results in a summation over several thousand terms. This number is tiny to simulate macromolecules containing tens of thousands of atoms.

A.3.4. Force

Eqn. (A.73) is sufficient for calculating potential energies and sampling in Monte Carlo simulations. For MD simulations, we also need forces and torques to evolve the position and orientation of objects. Forces are given by the spatial derivative of $u(\boldsymbol{r}_{ij}, \hat{R}_i, \hat{R}_j)$ as

$$(A.77) \qquad \boldsymbol{F}_{ij} = -\frac{\partial u_{ij}}{\partial \boldsymbol{r}_{ij}} = \left(-\frac{\partial u_{ij}}{\partial x_{ij}}, -\frac{\partial u_{ij}}{\partial y_{ij}}, -\frac{\partial u_{ij}}{\partial z_{ij}} \right)$$

where $\boldsymbol{r}_{ij} = (x_{ij}, y_{ij}, z_{ij})$. The spatial derivative will exert on $\mathcal{F}(r_{ij})$ and $Y_l^{k_i+k_j}(\psi_{ij}, \theta_{ij})$ separately.

Since

$$(A.78) \qquad \frac{\partial j_l(\omega r)}{\partial r} = \frac{l j_l(\omega r)}{r} - \omega j_{l+1}(\omega r),$$

the derivatives of $\mathcal{F}$ are:

(A.79)

$$-\frac{\partial \mathcal{F}_{l,l_i,l_j}^{k_i,k_j}(r_{ij})}{\partial \alpha_{ij}} = -\frac{\partial \mathcal{F}_{l,l_i,l_j}^{k_i,k_j}(r_{ij})}{\partial r_{ij}}\frac{\partial r_{ij}}{\partial \alpha_{ij}} = \frac{\alpha_{ij}}{r_{ij}}\int_0^\infty F_{l_i,l_j}^{k_i,k_j}(\omega)\left[\frac{Lj_l(\omega r)}{r} - \omega j_{l+1}(\omega r)\right]\omega^2 \mathrm{d}\omega \Bigg|_{r=r_{ij}}$$

where $\alpha = x, y, z$. We can tabulate $\int_0^\infty F(\omega)j_{l+1}(\omega r)\omega^3 \mathrm{d}\omega$ as well to accelerate the computation.

The derivative of $Y_l^{k_i+k_j}(\psi_{ij}, \theta_{ij})$ is

(A.80)
$$\frac{\partial Y_l^k(\psi,\theta)}{\partial \alpha} = \frac{\partial Y_l^k(\psi,\theta)}{\partial \cos\psi}\frac{\partial \cos\psi}{\partial \alpha} + \frac{\partial Y_l^k(\psi,\theta)}{\partial \theta}\frac{\partial \theta}{\partial \alpha}.$$

We know that $\cos\psi = z/r$ and hence

(A.81)
$$\frac{\partial \cos\psi}{\partial x} = -\frac{xz}{r^3}, \quad \frac{\partial \cos\psi}{\partial y} = -\frac{yz}{r^3}, \quad \frac{\partial \cos\psi}{\partial z} = \frac{x^2+y^2}{r^3}.$$

Also, since $\theta = \arccos(x/\sqrt{x^2+y^2})$, we have

(A.82)
$$\frac{\partial \theta}{\partial x} = \frac{|y|}{x^2+y^2}, \quad \frac{\partial \theta}{\partial y} = \frac{x^2}{|y|(x^2+y^2)}, \quad \frac{\partial \theta}{\partial z} = 0.$$

From Eqn. (A.10), the derivatives of spherical harmonics are given as

(A.83)

$$\frac{\partial Y_l^k(\psi,\theta)}{\partial \cos\psi} = \sqrt{\frac{(2l+1)(l-k)!}{4\pi(l+k)!}}e^{ik\theta}\frac{P_l^k(\cos\psi)}{\partial \cos\psi}$$

$$= \sqrt{\frac{(2l+1)(l-k)!}{4\pi(l+k)!}}e^{ik\theta}\left[-\frac{(l+1)\cos\psi}{\sin^2\psi}P_l^k(\cos\psi) - (l-m+1)P_{l+1}^k(\cos\psi)\right]$$

which is a linear combination of $Y_l^k(\psi, \theta)$ and $Y_{l+1}^k(\psi, \theta)$, and

$$\text{(A.84)} \qquad \frac{\partial Y_l^k(\psi, \theta)}{\partial \theta} = ik\sqrt{\frac{(2l+1)(l-k)!}{4\pi(l+k)!}}P_l^k(\cos\psi)e^{ik\theta} = ikY_l^k(\psi, \theta).$$

The force can be computed by the addition of all individual contributions.

A.3.5. Torque

Torques are computed via the derivatives with respect to infinitesimal rotations about some set of axes, which here are the x, y, and z-axes. For the rotation about a vector $\boldsymbol{u} = (u_x, u_y, u_z)$, by writing $\boldsymbol{u}$ as a quaternion $0 + u_x\boldsymbol{i} + u_y\boldsymbol{j} + u_z\boldsymbol{k}$, the variation in a quaternion caused by the rotation is given by

$$\text{(A.85)} \qquad \frac{\mathrm{d}\boldsymbol{q}}{\mathrm{d}\boldsymbol{u}} = \frac{1}{2}\boldsymbol{u} \cdot \boldsymbol{q}.$$

Thus, the derivatives of each component are

$$\text{(A.86)} \qquad \frac{\mathrm{d}q_w}{\mathrm{d}\boldsymbol{u}} = -\frac{1}{2}(u_x q_x + u_y q_y + u_z q_z),$$

$$\text{(A.87)} \qquad \frac{\mathrm{d}q_x}{\mathrm{d}\boldsymbol{u}} = \frac{1}{2}(u_x q_w + u_y q_z - u_z q_y),$$

$$\text{(A.88)} \qquad \frac{\mathrm{d}q_y}{\mathrm{d}\boldsymbol{u}} = \frac{1}{2}(u_y q_w + u_z q_x - u_x q_z),$$

$$\text{(A.89)} \qquad \frac{\mathrm{d}q_z}{\mathrm{d}\boldsymbol{u}} = \frac{1}{2}(u_z q_w + u_x q_y - u_y q_x).$$

Therefore, the derivative of u_{ij} with respect to a rotation about the axis $\boldsymbol{u}_\alpha$, $(\alpha = x, y, z)$ is given by the derivative of $D(\hat{R})$ as

(A.90)
$$\frac{\partial D}{\partial \boldsymbol{u}_\alpha} = \sum_\beta \frac{\partial D}{\partial q_\beta} \frac{\partial q_\beta}{\partial \boldsymbol{u}_\alpha},$$

where $\beta = w, z, y, z$ is the individual component of $\boldsymbol{q}$.